POLITECNICO DI MILANO
MOX, DIPARTIMENTO DI MATEMATICA
MATHEMATICAL MODELS AND METHODS IN ENGINEERING

MULTISCALE HOMOGENIZATION AND ITS APPLICATION TO TUMOR BIOLOGY: FLUID AND DRUG TRANSPORT PHENOMENA AND PORO MECHANICS OF GROWING MATERIALS

Doctoral Dissertation of:

Raimondo Penta

Supervisor:

Prof. Davide Ambrosi

The Chair of the Doctoral Program:

Prof. Roberto Lucchetti

2014 – XXVI cycle

"Questa tesi di dottorato é dedicata ai miei genitori Angelo e Filomena, che ringrazio infinitamente per aver sempre sostenuto le mie scelte con affetto e concretezza."

Raimondo

Acknowledgements

I would like to warmly acknowledge the ERC advanced grant *Mathcard* and especially its principal investigator Professor Alfio Quarteroni for the financial support of the present research project. I further thank very much the *MOX* research group, its director Professor Luca Formaggia and all the people I had the opportunity to interact with, I really felt at home during the last three years.

I also would like to acknowledge the professors and researchers I had the opportunity to interact with about the content of this work, in particular Alessandro Musesti, Fabio Nobile, Helen Byrne, Paolo Zunino, Reuben O'Dea, Sarah Waters.

I would like to devote a special thank to professors Alfredo Marzocchi and Edie Miglio, who supervised my master thesis and motivated myself to try the admission of the Politecnico Ph.D. programme in a very difficult moment of my life three years ago.

A friendly thank goes to Anna Zanzottera and Viola Pettinati [1] for listening to myself with patience and Franco Dassi[2], who managed to successfully teach me some theoretical numerical analysis.

To Professor Alfio Grillo, thank you so much for believing in me and welcoming so friendly in Turin.

To Alessandro Lucantonio, thank you for introducing myself to the magic C..SOL world. [3]

To Davide Bossini, you would deserve much more than a simple thank you, but I am gonna try a one-page acknowledgements only for the sake of style[4] :D Anyway, thank you so much for

[1] I finally succeeded in what you know

[2] You are one of the best and honest person I ever met and I feel you'll have the success you deserve!

[3] Since the thesis is in english the only thing I can add is "Myba" ;)

[4] Still, I failed :P

continuosly supporting myself[5]

To Laura Cattaneo, thank you for listening to, and collaborating with myself, it was definitely a pleasure.[6]

To Pietro Mascheroni, thank you for our collaboration during your master thesis project, it was a great occasion of mutual scientific and personal growth.[7]

To Simone Pezzuto, thank you very very much for your moral support and Giobbe's patience in training myself to numerical experiments.

A very special and warm thank is devoted to Dr. Rebecca J. Shipley (a.k.a Becky). This thesis wouldn't exist without your help and support, I think our collaboration was a unique experience and I will be always thanking you a lot! Also, you welcomed me in London UCL and I will never forget that experience.

Finally, I would need a thousands thesis pages to thank my Ph.D. advisor Professor **Davide Ambrosi**. Davide, thank you for your fundamental support and endless patience [8], it was a great honor to work with you and learn from you.

[5] I am finally becoming a matematician, like you always said :P

[6] I also will save in my memory the fun moments in Nottingham, including the *walk* to go back to the hotel :D

[7] You are supposed to watch *Hello Vietnam* on youtube while reading this :)

[8] which surely does not belong to L^2 :P

Abstract

Aim of the present thesis is the development of novel mathematical models to describe the fluid and drug transport processes in malignant biological tissues, as well as their mechanical properties and growth. The work falls within the framework of classical methods of mathematical physics, in particular multiscale *homogenization* (Sanchez-Palencia, 1980, 1983; Holmes, 1995; Mei and Vernescu, 2010), applied to the behavior of biological systems pointed out by recent experiments (see e.g. Carmeliet and Jain (2000); Jain et al. (2007); Moeendarbary et al. (2013)).

The tumor microvasculature represents an *ad hoc* supply network, which is sprout out via the so called angiogenesis process, in order for the malignant mass to obtain nutrients for growth, (Carmeliet and Jain, 2000). The angiogenic blood vessels are characterized by functional and structural abnormalities and heterogeneities and they are in general highly permeable, leaking and tortuous, such that the blood circulation through these vessels can be impaired and hard to predict, (Hashizume, 2000). In this scenario, several complex and coupled physical phenomena take place, including blood and drug circulation in the angiogenic capillary network, fluid and drug transport, as well as chemical reactions in the interstitial space and blood leakage through the vessels membrane, which enables the coupling between the two compartments. A complete description of the physics in the tumor system represents a challenging issue from a mathematical modelling and computing viewpoint. We thus exploit the sharp length scale separation between the characteristic tumor length (the *macroscale*) and the intercapillary distance (*the microscale*), such that, via asymptotic homogenization, we are able to decouple spatial variations and obtain a robust macroscale theoretical framework. The resulting model takes into account both the relevant physical

phenomena occuring in the system and reduces mathematical complexity; a major aim for this work is, in perspective, to achieve a practical tool which can help the setup of effective anti-cancer therapies. The role of the microvascular geometrical complexity is encoded in the model coefficients, which are computed via numerical simulations of classical differential problem on a single representative *cell*.

Tumor growth and its mechanical properties are important issues to tackle. The multiscale analysis of poroelastic growing materials (where, in this case, the micro and macro spatial scales are identified with the pore radius and medium length, respectively) we carried out represents a theoretical starting point to improve our physical insight about the interplay between material growth and elastic strains and it can be applied to the tumor mass, which has been shown to be behave as a poroelastic material (Moeendarbary et al., 2013).

The thesis is organized in the following chapters:

- In Chapter 1, (Penta et al., 2013) a system of differential equations for coupled fluid and drug transport in vascularized (malignant) tissues is derived by a multiscale expansion. We start from mass and momentum balance equations, stated in the physical domain, geometrically characterized by the intercapillary distance (the *microscale*). The Kedem-Katchalsky equations are used to account for blood and drug exchange across the capillary walls. The multiscale technique (*homogenization*) is used to formulate continuum equations describing the coupling of fluid and drug transport on the tumor length scale (the *macroscale*), under the assumption of local periodicity; macroscale variations of the microstructure account for spatial heterogeneities of the angiogenic capillary network. A double porous medium model for the fluid dynamics in the tumor is obtained, where the drug dynamics is represented by a double advection-diffusion-reaction model. The homogenized equations are straightforward to approximate, as the role of the vascular geometry is recovered at an average level by solving standard cell differential problems. Fluid and drug fluxes now read as effective mass sources in the macroscale model, which upscale the interplay between blood and drug dynamics on the tissue scale. We aim to provide a theoretical setting to support the design of effective anti-cancer therapies

- In Chapter 2, (Penta and Ambrosi, 2014) the role of the microvascular network geometry on transport phenomena in solid tumors and its interplay with the leakage and pressure drop across the vessels is qualitatively and quantitatively discussed. Our starting point is a multiscale homogenization, suggested by the sharp length scale separation that exists between the

characteristic vessels and tumor tissue spatial scales, referred to as the *microscale* and the *macroscale*, respectively. The coupling between interstitial and capillary compartment is described by a double Darcy model on the macroscale, whereas the geometric information on the microvascular structure is encoded in the effective hydraulic conductivities, which are numerically computed solving classical differential problems on the microscale representative *cell*. Then, microscale information is injected into the macroscopic model, which is analytically solved in a prototypical geometry and compared with previous experimentally validated, phenomenological models. In this way, we are able to capture the role of the standard blood flow determinants in the tumor, such as the tumor radius, tissue hydraulic conductivity and vessels permeability, as well as the influence of the vascular *tortuosity* on fluid convection. The results quantitatively confirm that transport of blood (and, as a consequence, of any advected anti-cancer drug) can be dramatically impaired by increasing the geometrical complexity of the microvasculature. Hence, our quantitative analysis supports the argument that geometric regularization of the capillary network improve blood transport and drug delivery in the tumor mass.

- In Chapter 3, (Penta et al., 2014), a new mathematical model is developed for the macroscopic behaviour of a porous, linear elastic solid, saturated with a slowly-flowing incompressible, viscous fluid, with surface accretion of the solid phase. The derivation uses a formal two-scale asymptotic expansion to exploit the well-separated length scales of the material: the pores are small compared to the macroscale, with a spatially-periodic microstructure. Surface accretion occurs at the interface between the solid and fluid phases, resulting in growth of the solid phase through mass exchange from the fluid at a prescribed rate (and *vice versa*). The averaging derives a new poroelastic model, which reduces to the classical result of Burridge and Keller in the limit of no growth. The new model is of relevance to a large range of applications including packed snow, tissue growth, biofilms and subsurface rocks or soils.

Contents

CHAPTER 1

Multiscale homogenization for fluid and drug transport in vascularized malignant tissues

1.1 Introduction

During the early stage of tumor growth (the "avascular phase"), nutrients enter the malignant mass and feed its development by simple diffusion. When the size of the tumor exceeds the diffusion length scale, the angiogenetic process starts: new vessels sprout from the neoplastic mass and create an *ad hoc* supply network (Carmeliet and Jain, 2000). The new microvasculature is characterized by abnormal features, as regards both geometry and functionalities. Differently than healthy vessels, the tumor ones are disorganized, tortuous and dilated, while the vessels walls are highly permeable and exhibit openings and defects (Hashizume, 2000). The tumor cells environment is often characterized by a high interstitial fluid pressure (Jain and Baxter, 1988; Boucher et al., 1990; Jain et al., 2007), which is related to both the microvasculature geometrical abnormalities and a reduction of the interstitial space (Heldin et al., 2004). As a result, the pressure gap across the capillary wall is small, so that the effectiveness of anti-cancer therapies can be compromised because of disordered blood flow in the vessels and a reduced distribution of drug molecules reaching the tumor cells

through advection. To improve anti-cancer strategies and make their effects easier to predict, understanding the relationship between the physical phenomena underlying the drug delivery process and the tumor system properties is essential.

Several mathematical models have been proposed in the last ten years to investigate the microscopic inhomogeneity of tumors, that are composed by proliferating, apoptotic, healthy cells end extracellular matrix. The mixture theory has been exploited to address both the avascular and the vascular stages of tumor growth, stating and solving numerically the equations of mass, momentum and energy balance for several species Preziosi and Byrne (2003); Ambrosi and Preziosi (2002); Schuff et al. (2013a,b). The theoretical basis of this approach is that the macroscale equations are not obtained on the basis of upscaling arguments from microstructural balance, but they are *a priori* stated, or at most obtained on the basis of pure averaging. The governing equations and the constitutive equations then mimick the behavior that single components have *in bulk* and the interaction forces between components are deduced on the basis of heuristic arguments. Mixture theory models can be quite general, including any number of interacting species, nonlinear behavior and no apparent retriction on the geometrical features of the microstructure.

In this chapter we address the tumor microcirculation by an approach that, as the mixture theory, aims to account for the gross behavior of the system in terms of averaged equations. However, the multiple scale (*homogenization*) method is able to upscale the parameters of the macro equations on the basis of microstructural arguments. The multiple-scales method (Sanchez-Palencia, 1983; Holmes, 1995) has been successfully applied to various physical systems, a most important field of applications of this technique being porous media flow (see for istance Arbogast and Lehr, 2006). The use of this technique in investigating living systems is more recent; a remarkable example of multiscale analysis applied to the fluid and drug transport in the microvasculature can be found in Shipley and Chapman (2010). There, the derivation is obtained by scaling the various physical numbers (which arise from a proper non-dimensionalization of the microscale model) according to their order of magnitude estimate, based on several examples which can be found in the biophysical literature. Furthermore, the blood is assumed to behave as a Newtonian fluid in a locally periodic and macroscopically uniform domain: macroscopic variations of the relevant fields are allowed, but macroscale variations of the microstructure, which might be relevant in malignant vascular networks, are not. Here, we follow a slightly different approach and derive a macroscale model which generalizes that in Shipley and Chapman (2010); the latter can be recovered under a number of simplifying assumptions.

More specifically, we develop a mathematical model which describes the fluid and drug transport phenomena on the tissue length scale, accounting for both the crucial role of the tumor vasculature geometry and the mutual influence of mass and fluid transcapillary exchange. In our work, we are able to deal with general interface conditions at the boundary between vessels and tumor interstitium. In particular, we adopt a non-equilibrium (possibly non-linear) thermodynamic approach (Kedem and Katchalsky, 1958) to track the influence of the concentration of drug molecules on the fluid flow (i.e the osmotic pressure) and to account for the convection of drug across the capillary walls. We enforce the sharp length scale separation between the intercapillary distance and the tumor size, then we state the differential model on the physical domain. Here, non-dimensionalization and scaling are performed accounting for the physical behavior of the representative quantities with respect to the asymptotic expansion parameter (the ratio between the intercapillary distance and the characteristic tissue scale), rather than their order of magnitude, which might depend strongly on the specific biophysical system at hand. This approach allows us to describe the greatest possible number of physical phenomena at leading order, though an order of magnitude estimate of the relevant non-dimensional numbers can be *a posteriori* performed to evaluate the relative importance of the various parameters. Further, our results account for possible macroscopic variations of the microstructure and for changes in the effective viscosity due to possible spatial heterogeneities.

The final macroscale model for the physical quantities of interest, such as velocity, concentration and pressure field, describe the blood dynamics through a double Darcy's system of differential equations, whereas the drug dynamics is represented by a double advection-diffusion-reaction system. The interstitial and capillary models are coupled through effective mass sources which account for the fluid and drug transport interplay. The present mathematical model is computationally feasible, because the key role of the microvascular geometry is encoded in the effective parameters of the macroscale model, which can be computed solving standard differential problems on a single cell. Hence, in perspective, numerical results obtained from such a model might help to predict the effectiveness of anti-cancer therapies.

The chapter is organized as follows:

- Section 1.2 is devoted to formulate the continuum mechanics balance equations and the corresponding boundary conditions on the physical domain characterized by the intercapillary distance length scale, so that the distinction between the interstitial and capillary compartment is pointed out.

- In section 1.3 the governing equations are rewritten in non-dimensional form.

- In section 1.4 we apply a two-scales asymptotic expansion to obtain the effective governing equations describing the physical behaviour of the system on the tissue scale. The fluid dynamics is modeled via a double Darcy's differential system, whereas the drug dynamics is represented by a double advection-diffusion-reaction model. The model reported in Shipley and Chapman (2010) is recovered as a particular case.

- In section 1.5 concluding remarks and future perspective are illustrated.

1.2 Balance equations

In this chapter we formulate a mathematical model for fluid and drug transport in a biological tissue permeated by a capillary network on the basis of a two-scale asymptotic expansion. The domain $\Omega \subset \mathbb{R}^3$ is composed of two subdomains, Ω_n and Ω_t, the capillary network and the tissue interstitium, respectively. Following the available biological literature, we assume the typical mean intercapillary distance d to be small compared to the tissue characteristic length L, so that we define a suitable spatial scale ratio as

$$\epsilon = \frac{d}{L} \ll 1. \tag{1.1}$$

According to the analysis reported in Less et al. (1991), the mean intercapillary distance is about $50\,\mu m\,(d \approx 10^{-5}\,\text{m})$, whereas, for a tumor, the characteristic length can vary between $1\,\text{cm}$ and $12\,\text{cm}$ (Stevens et al., 2001); hence $L \approx 10^{-2} - 10^{-1}$ m and

$$\epsilon \approx 10^{-4} - 10^{-3}. \tag{1.2}$$

At this stage, every unknown field of interest, such as the pressure p, the concentration of drug c and the blood velocity $\boldsymbol{u}$, is in principle a function of space $\boldsymbol{x}$ and time t. These quantities obey to balance laws that take specific form depending on the portion of the domain of interest and, in general, they are not continuous across subdomains interface. In particular, their restrictions to the interstitial and capillary compartment are denoted by subscripts t and n, respectively. We first consider the fluid and drug transport in each portion of Ω, then we will detail the proper interface conditions in order to close the resulting coupled differential problem.

1.2.1 Interstitial Fluid flow

The tumor interstitium Ω_t is here considered to be a non deformable, isotropic porous medium, where the intracellular space represents the pores and Darcy's law applies:

$$\boldsymbol{u}_t = -\kappa \nabla p_t \quad \text{in } \Omega_t \tag{1.3}$$

$$\nabla \cdot \boldsymbol{u}_t = 0 \quad \text{in } \Omega_t, \tag{1.4}$$

where κ denotes the tissue hydraulic conductivity, which, in tumors, may vary dramatically depending on the tissue type and its chemical composition (Swabb et al., 1974).

We assumed the medium isotropy for the sake of simplicity only. This assumption could be easily relaxed when replacing κ with a second order positive definite symmetric tensor to account for anisotropy, with some more complicated notations, but no increased insight from a physical viewpoint.

1.2.2 Capillary fluid flow

Blood is a non-Newtonian fluid, composed by the plasma (which can be regarded as a Newtonian solution made of water and proteins) and red blood cells, at a concentration (haematocrit) of $40 - 45\%$. A detailed analysis of blood rheology, regarding in particular its shear thinning behavior (i.e the apparent viscosity decreases with increasing shear rate), can be found for example in Formaggia et al. (2009). In particular, in vessels much larger than red blood cells (i.e $\approx 4\mu m$ (Jayaweera et al., 1994)), at constant temperature and haematocrit, blood can be assumed to behave (approximately) as a Newonian fluid, with viscosity greater than plasma.

In small capillaries, a more complex blood rheology should be taken into account, since non-Newtonian effects, such as the Fahareus and the Fahareus-Lindqvist effects (Fahareus and Lindqvist, 1931) occur. The typical diameter of the capillaries is comparable with the size of red blood cells, both in healthy (from 5 to $8\mu m$, Simonescu et al. (1974)) and malignant tissues (values ranging from 10 to $30\mu m$ are reported, for example, in Jain (1988)).

Without entering delicate theoretical questions about possible constitutive relations for blood flow at such scales, we restrict to consider it as a viscous fluid where the effective viscosity explicitly depends on the radius of the vessel r. In other words, we tacitly enforce a complex rheology of the blood, adopting an effective viscosity that depends on the radius, where such a spatial dependence is the *result* of an immaterial non-Newtonian constitutive law applied to a specific geometry.

For example, according to Pries et al. (1992) and Pozrikidis (2009), when haematocrit and tem-

perature are fixed to 45% and $37°C$, respectively, the flow in a straight vessel can be recovered by adopting an effective viscosity μ_e given by:

$$\mu_e = \mu \left(220 \exp(-2.6r) + 3.2 - 2.44 \exp(-0.06(2r)^{0.645})\right), \tag{1.5}$$

where $\mu \approx 1.16 - 1.33 \cdot 10^{-3}$ Pa s (Cooke and Stuart, 1988) denotes plasma viscosity. Whenever the capillary network is regular enough that an average representative radius can be identified, the viscosity can be considered constant, such that its value can be computed by means of (1.5). For example, for $r = 10\mu m$, we obtain $\mu_e = 1.59\mu$, whereas the the blood viscosity in large vessels (Rand et al., 1964) is $\approx 4 \cdot 10^{-3}$ Pa s, is reached only when r is approaching $200\mu m$, such that $\mu_e \approx 3.2\mu \approx 4 \cdot 10^{-3}$ Pa s.

Since the angiogenic capillary network embedded in a tumor mass typically exhibits strong spatial eterogeneities, we account for possible spatial variations in the (effective) capillary diameter. This can be performed, for example, replacing r in (1.5), with a suitable function $r = r(\boldsymbol{x})$, yielding

$$\mu_e = \mu_e(\boldsymbol{x}); \tag{1.6}$$

r is in principle a function of $\boldsymbol{x}$ depending on the geometric characteristics of the capillary network at hand (this can also be induced by medical images inspection). It is worth noting that a more accurate modelling of the blood rheology in small capillaries should also account for variations in haematocrit (which is here fixed for the sake of simplicity). In particular, in small capillaries, the so called phase-separation may occur, i.e. the red blood cell concentration can exhibit significant spatial inhomogeneities at diverging bifurcations. Since the effective viscosity exponentially increase with increasing haematocrit, a highly heterogeneous blood flow resistance may be observed in bad-organized and tortuous vascular networks Pries and Secomb (2003).

Finally, inertial and body forces can be ignored and the blood capillary flow is governed by the following Stokes' problem:

$$\mu_e \nabla^2 \boldsymbol{u}_n = \nabla p_n \quad \text{in } \Omega_n \tag{1.7}$$

$$\nabla \cdot \boldsymbol{u}_n = 0 \quad \text{in } \Omega_n. \tag{1.8}$$

1.2.3 Drug transport, reaction and diffusion

The combined action of transport and diffusion determines the concentration of drug in the blood vessels, whereas, in a tumor, cellular uptake ("the reaction") plays a major role. We thus assume a standard advection-diffusion equation for the concentration in the capillaries c_n, whereas

an advection-diffusion-reaction equation holds for the concentration c_t in the tissue interstitium:

$$\frac{\partial c_n}{\partial t} + \nabla \cdot (c_n \boldsymbol{u}_n - D_n \nabla c_n) = 0 \quad \text{in}\, \Omega_n \tag{1.9}$$

$$\frac{\partial c_t}{\partial t} + \nabla \cdot (c_t \boldsymbol{u}_t - D_t \nabla c_t) = -h(c_t) \quad \text{in}\, \Omega_t, \tag{1.10}$$

Here D_c and D_t are the species diffusivity in their own subdomains and $h(c_t)$ is a positive, possibly non-linear function of the interstitial concentration, which accounts for the reaction mechanisms occurring in the system. When linear uptake only is relevant, we can prescribe:

$$h(c_t) = \gamma c_t, \tag{1.11}$$

where γ is the reaction uptake rate.

1.2.4 Interface fluxes

The fluxes across the capillary wall can be obtained on the basis of non-equilibrium thermodynamic arguments, originally developed by Kedem and Katchalsky (1958) and then generalized to other bio-physical systems (Dreher et al., 2006; Waniewsky, 2006). When assuming that the Kedem-Katchalsky formulation applies for both blood and drug fluxes, we obtain

$$\phi_b = L_p \left[(p_n - p_t) - \sigma RT (c_n - c_t) \right] \tag{1.12}$$

$$\phi_d = \phi_b (1 - \sigma) c_m + P (c_n - c_t). \tag{1.13}$$

where ϕ_b and ϕ_d denote the blood and drug fluxes per unit of total exchange surface area, respectively, whereas L_p is the hydraulic conductivity of the vessel wall, which accounts for the fluid leakage from the capillaries. In tumors, it can be up to two orders of magnitude higher than in healthy tissue, because of the openings and defects that characterize the tumor blood vascular networks (Jain et al., 2007). Here, R is the universal gas constant, T is the absolute temperature, P is the diffusive permeability of the vessel wall. The osmotic reflection coefficient $0 < \sigma < 1$ quantifies the departure of a membrane behavior from semipermeability. For an ideal semipermeable membrane (no solute flux due to convection) $\sigma = 1$, so that the osmotic flow is maximized, whereas for an unselective membrane there is no osmosis and hence $\sigma = 0$. The value of σ depends on the relative geometry and size of the specific molecule and of the membrane pores (Bhalla and Deen, 2007).

According to (1.12), the blood flux across the interface is due both to the hydrostatic pressure drop and the osmotic pressure difference, the latter being proportional to the concentration jump for dilute solutions. The drug flux in (1.13) is the sum of a convective term, proportional to the

fluid flux, and a diffusive one, proportional to the difference in concentration. The term c_m has the dimension of a concentration and a thorough analysis (Waniewsky, 2006) suggests that it is a non-linear function of the fluid flux ϕ_b of the type:

$$c_m = (1-f)c_n + fc_t; \quad f := \frac{1}{\tilde{\lambda}\phi_b} - \frac{1}{\exp(\tilde{\lambda}\phi_b) - 1} \quad \tilde{\lambda} := \frac{1-\sigma}{P}. \tag{1.14}$$

The quantity $\tilde{\lambda}\phi_b$ (at fixed blood flux ϕ_b) is often called the *transvascular* Péclet number (Pe$_v$), as it expresses the relative importance of convection to diffusion across the capillary walls. It is worth recalling the linearized analogues of relationship (1.13) when limiting case of Pe$_v$ are taken into account, namely:

$$\phi_d = \phi_b(1-\sigma)c_n + P(c_n - c_t) \quad \text{for Pe}_v \gg 1 \tag{1.15}$$

and

$$\phi_d = \phi_b(1-\sigma)\bar{c} + P(c_n - c_t) \ ; \ \bar{c} = \frac{c_n + c_t}{2} \quad \text{for Pe}_v \ll 1. \tag{1.16}$$

The relationship (1.13) is widely accepted in the bio-physical literature (see for example Jain and Baxter (1988); Tang et al. (2012)), whereas the approximation (1.16) has been previously adopted, for example, in Dreher et al. (2006). A rough approximation for the drug flux, which rigorously apply only when the blood flux ϕ_b is negligible (Jain, 1987a), yields a membrane law of the type:

$$\phi_d = P(c_n - c_t), \tag{1.17}$$

which has been enforced by Modok et al. (2006, 2007).

Remark 1.1. According to the most widely accepted bio-physical literature (see for example Jain and Baxter, 1988), equation (1.12) should read:

$$\phi_b = L_p\left[(p_n - p_t) - \sigma(\pi_n - \pi_t)\right], \tag{1.18}$$

where $(\pi_n - \pi_t)$ denotes the osmotic pressure difference due to different concentrations of plasma proteins across the vessel walls. However, the present work is mostly related to malignant tissue, so that, according to the analysis reported in Jain et al. (2007), the typical capillary pore dimensions ($\approx \mu m$) are much larger than the hydrodynamic radius of plasma proteins (for example, the typical radius of albumin is $\approx 3.5\ nm$). As a result, the osmotic pressure contribution due to plasma proteins is negligible in tumors. It is worth remarking that this could not be the case, in general, for drug macromolecules, whose radius can reach dramatically higher values with respect to plasma proteins (for example, particles characterized by a radius of $\approx 100 - 150\ nm$, have been recently developed (Scomparin et al., 2011)). We then argue that, in tumors, even though the blood flux

is mostly driven by the pressure drop, the most general flux prescription is of the type (1.12), whereas, in healthy tissues, an accurate blood flux prescription should account for the osmotic pressure contribution, as in (1.18).

1.2.5 Interface conditions

Continuity of the drug and blood fluxes at the interface boundary $\Gamma = \partial\Omega_n \cap \partial\Omega_t$ leads to the following interface conditions:

$$\boldsymbol{u}_n \cdot \boldsymbol{n} = \boldsymbol{u}_t \cdot \boldsymbol{n} = \phi_b \tag{1.19}$$

$$(c_n \boldsymbol{u}_n - D_n \nabla c_n) \cdot \boldsymbol{n} = (c_t \boldsymbol{u}_t - D_t \nabla c_t) \cdot \boldsymbol{n} = \phi_d, \tag{1.20}$$

where $\boldsymbol{n}$ is the outward unit vector normal to the capillary surface, whereas the (possibly non-linear) fluxes are denoted by $\phi_b(p_n, p_t, c_n, c_t)$ and $\phi_d(p_n, p_t, c_n, c_t)$ and dictate the fluid and drug transfer rate per unit area across the capillary walls.

Remark 1.2. According to the biophysical literature (see, e.g. Jain and Baxter (1988); Jain et al. (2007)), the actually measured physical quantities are the average macroscopic blood and drug fluxes. For example the blood flux, which is often referred to as J_v, reads:

$$J_v = \mathrm{S}\phi_b, \tag{1.21}$$

where S is the total exchange surface of the capillary vessels and ϕ_b is given by (1.12) or (1.18) depending on the actual physical system at hand. Even though it is more convenient to prescribe the fluxes per unit area in the current formulation, we still have to account for the correct asymptotic behavior of the various physical quantities involved in the extravasation process. In fact, it is reasonable to assume that the actual measured flux (i.e of the type (1.21)) for a fixed portion of the tissue is finite, even when the number of capillaries (and correspondingly their total surface) increases within the volume, so that the average distance between them decreases, that is:

$$\mathrm{S} \propto N \propto \frac{L}{d} = \frac{1}{\epsilon} \rightarrow \phi_b \propto \frac{1}{N} \propto \frac{d}{L} = \epsilon, \tag{1.22}$$

where N is the (estimated) average capillary number in the network. We formalize the heuristic argument (1.22) highlighting the correct asymptotic behavior of both the blood and drug fluxes per unit area, ϕ_b and ϕ_d, via the following definitions:

$$\phi_b = \epsilon\Phi_b, \quad \phi_d = \epsilon\Phi_d, \tag{1.23}$$

and for the sake of simplicity, from now on, we still refer to the quantities Φ_b and Φ_d as the blood and drug flux, respectively. The interface conditions (1.19-1.20) then rewrite:

$$\boldsymbol{u}_n \cdot \boldsymbol{n} = \boldsymbol{u}_t \cdot \boldsymbol{n} = \epsilon \Phi_b \tag{1.24}$$

$$(c_n \boldsymbol{u}_n - D_n \nabla c_n) \cdot \boldsymbol{n} = (c_t \boldsymbol{u}_t - D_t \nabla c_t) \cdot \boldsymbol{n} = \epsilon \Phi_d. \tag{1.25}$$

The ϵ coefficient appearing on the right hand sides of (1.24-1.25) then reflects the application of average experimental measures to a local balance law. In fact, this is the proper scaling to ensure that local fluxes contributions, which are expected to translate into volumetric contribution on the global scale, are finite in the limit for $\epsilon \to 0$.

To close the problem, we need one more boundary condition for the tangent components of the fluid velocity in the capillaries. Since the solid compartment is a porous medium, following Jones (1973), we assume that the following generalized slip conditions (Beavers and Joseph, 1967) hold

$$\boldsymbol{u_n} \cdot \boldsymbol{\tau} = -\frac{\sqrt{k}}{\alpha_s} \left[(\boldsymbol{n} \cdot \nabla) \boldsymbol{u_n} \right] \cdot \boldsymbol{\tau} \text{ on } \quad \Gamma, \tag{1.26}$$

where α_s is a non-dimensional parameter, which depends on the properties of the porous surface, $\boldsymbol{\tau}$ is any unit vector tangent to the capillary surface and k is the tissue permeability, which is related to the hydraulic conductivity k by

$$\kappa = \frac{k}{\mu_e}. \tag{1.27}$$

1.3 Non-dimensional form of the equations

Equations (1.3), (1.4), (1.7), (1.8), (1.9), (1.10), equipped with boundary conditions (1.24), (1.25), (1.26) and proper effective viscosity and fluxes prescriptions (for example of the type (1.5,1.6) and (1.12,1.13), respectively), represent a coupled system of partial differential equations in the variables $\boldsymbol{u}_n$, $\boldsymbol{u}_t$, p_n, p_t, c_n, c_t on the whole domain Ω, which includes both the tumor interstitium Ω_t and the capillary network Ω_n. We now rewrite the system in non-dimensional variables:

$$\boldsymbol{x} = L\boldsymbol{x'} \quad \boldsymbol{u} = \frac{Cd^2}{\mu}\boldsymbol{u'} \quad p = CLp' \quad c = C_r c' \quad t = \frac{L\mu}{Cd^2}t', \tag{1.28}$$

where C_r, C are the reference concentration and pressure gradient, respectively. The corresponding system of partial differential equations in non-dimensional form then reads (the primes have been dropped for the sake of simplicity)

$$\bar{\mu}\epsilon^2\nabla^2\boldsymbol{u}_n = \nabla p_n \quad \text{in}\,\Omega_n \tag{1.29}$$

$$\nabla\cdot\boldsymbol{u}_n = 0 \quad \text{in}\,\Omega_n \tag{1.30}$$

$$\boldsymbol{u}_t = -\bar{\kappa}\nabla p_t \quad \text{in}\,\Omega_t \tag{1.31}$$

$$\nabla\cdot\boldsymbol{u}_t = 0 \quad \text{in}\,\Omega_t \tag{1.32}$$

$$\frac{\partial c_n}{\partial t} + \nabla\cdot(c_n\boldsymbol{u}_n - A_n\nabla c_n) = 0 \quad \text{in}\,\Omega_n \tag{1.33}$$

$$\frac{\partial c_t}{\partial t} + \nabla\cdot(c_t\boldsymbol{u}_t - A_t\nabla c_t) = -\bar{h}(c_t) \quad \text{in}\,\Omega_t \tag{1.34}$$

supplemented by the interface conditions

$$\boldsymbol{u}_n\cdot\boldsymbol{n} = \epsilon\bar{\Phi}_b \quad \text{on}\,\Gamma \tag{1.35}$$

$$\boldsymbol{u}_n\cdot\boldsymbol{\tau} = -\epsilon\phi\left[(\boldsymbol{n}\cdot\nabla)\boldsymbol{u_n}\right]\cdot\boldsymbol{\tau} \quad \text{on}\,\Gamma \tag{1.36}$$

$$\boldsymbol{u}_t\cdot\boldsymbol{n} = \epsilon\bar{\Phi}_b \quad \text{on}\,\Gamma \tag{1.37}$$

$$(c_n\boldsymbol{u}_n - A_n\nabla c_n)\cdot\boldsymbol{n} = \epsilon\bar{\Phi}_d \quad \text{on}\,\Gamma \tag{1.38}$$

$$(c_t\boldsymbol{u}_t - A_t\nabla c_t)\cdot\boldsymbol{n} = \epsilon\bar{\Phi}_d \quad \text{on}\,\Gamma, \tag{1.39}$$

where $\bar{\Phi}_b$, $\bar{\Phi}_d$, $\bar{h}$ are the corresponding non-dimensional blood and drug fluxes and reaction function, respectively. The non-dimensional numbers (functions) introduced above are defined as follows:

$$\bar{\mu}(\boldsymbol{x}) = \frac{\mu_e(\boldsymbol{x})}{\mu}\,;\ \bar{\kappa} = \frac{\kappa\mu}{d^2}\,;\ A_n = \frac{D_n\mu}{LCd^2}\,;\ A_t = \frac{D_t\mu}{Cd^2}\,;\ \phi = \frac{\sqrt{\bar{\kappa}\bar{\mu}(\boldsymbol{x})}}{\alpha_s}. \tag{1.40}$$

Here, $\bar{\mu}$ represents the relative fluid viscosity, whereas $\bar{\kappa}$, ϕ are the non-dimensional hydraulic conductivity and slip coefficient, respectively. The non-dimensional numbers A_n and A_t express the relative importance of diffusion vs convection, so that they can be written as

$$A_n = \frac{1}{\text{Pe}_n}; \quad A_t = \frac{1}{\text{Pe}_t}, \tag{1.41}$$

where the capillary and interstitial Péclet numbers Pe_n and Pe_t are defined as

$$\text{Pe}_n := \frac{LCd^2}{D_n\mu}; \quad \text{Pe}_t := \frac{LCd^2}{\mu D_t}. \tag{1.42}$$

Further remarks about the choice (1.28) of non-dimensional variables and the meaning of the corresponding equations are in order.

The Stokes' type characteristic velocity

$$U = \frac{Cd^2}{\mu} \tag{1.43}$$

adopted in (1.28) preserves the asymptotic behavior of the interstitial fluid velocity, as well as in the capillaries (see continuity condition (1.24)) as $\epsilon \to 0$. Problem (1.29) is the typical asymptotic problem which characterizes the flow in porous media in the multiple scales analysis context, as, for example, in Burridge and Keller (1981); Holmes (1995); Arbogast and Lehr (2006). The transport parameters, including the tissue hydraulic conductivity and any other transvascular parameter encoded in the fluxes $\bar{\Phi}_b$, $\bar{\Phi}_d$ (for example, the membrane conductivity L_p and the diffusive permeability P), are given by experimental measurements, that implicitly comprise a dependence on both the geometry and on the tissue and capillary walls material and chemical composition. Here, we claim that the observed Darcy's interstitial flow, together with the Kedem-Katchalsky leakage of blood and macromolecules from the vessels, should be consistent with the Stokes's type characteristic velocity profile assumed in (1.28). As a consequence, the non-dimensional tissue hydraulic conductivity given by (1.40) and the non-dimensional fluxes are to be considered fixed in the limit $\epsilon \to 0$. Finally, we assume a formal balance between diffusion, reaction and convection within the domain, so that the Péclet numbers (1.42) and the non-dimensional reaction $\bar{h}$ are fixed in the limit $\epsilon \to 0$. This is done for the sake of generality, as this approach allows us to retain the greatest possible number of physical phenomena in the asymptotic analysis. However, the relative importance of the various phenomena can be *a posteriori* evaluated via an order of magnitude estimate of the resulting non-dimensional numbers, to account for specific physical regimes (such as, for example, the advection dominated regime), depending on the actual physical system at hand.

1.4 Multiscale formulation

In this section we employ the two-scales technique (Sanchez-Palencia, 1983; Holmes, 1995) to derive a continuum macroscale model for the system of equations (1.29-1.39). Since $\epsilon \ll 1$, we enforce the sharp length scale separation between the intercapillary distance d, the *microscale*, and the tissue characteristic dimension L, the *macroscale*, (see figure 1.1) defining:

$$\boldsymbol{y} := \frac{\boldsymbol{x}}{\epsilon}. \tag{1.44}$$

Following the usual approach in multiscale analysis, from now on $\boldsymbol{x}$ and $\boldsymbol{y}$ denote independent variables, representing the macro and micro spatial scale, respectively. We then assume that any unknown field ψ defined throughout this work (i.e. $\boldsymbol{u}_n$, $\boldsymbol{u}_t$, p_n, p_t, c_n, c_t) is a function of these independent spatial variables:

$$\psi = \psi(\boldsymbol{x}, \boldsymbol{y}, t)$$

so that the differential operators transform accordingly,

$$\nabla \to \nabla_{\boldsymbol{x}} + \frac{1}{\epsilon}\nabla_{\boldsymbol{y}}; \quad \nabla^2 \to \frac{1}{\epsilon^2}\nabla_{\boldsymbol{y}} + \frac{2}{\epsilon}\nabla_{\boldsymbol{y}} \cdot \nabla_{\boldsymbol{x}} + \nabla^2_{\boldsymbol{x}}. \tag{1.45}$$

For every field ψ we formally perform the following multiple scales expansion in power series of ϵ:

$$\psi = \psi_\epsilon(\boldsymbol{x}, \boldsymbol{y}, t) = \sum_{l=0}^{\infty} \psi^{(l)}(\boldsymbol{x}, \boldsymbol{y}, t)\epsilon^l. \tag{1.46}$$

The components $\psi^{(l)}$ are defined for every $\boldsymbol{x}$ belonging to the macroscale domain, whereas $\boldsymbol{y}$ spans only the specific portion of the microscale where ψ is defined. We assume periodicity in the microscale variable, so that every $\psi^{(l)}$ is $\boldsymbol{y}$-periodic.

Remark 1.3. Only *local* periodicity is assumed, while macroscale variation in any field ψ is allowed. Furthermore, the interstitial and capillary compartments can also macroscopically vary, that is $\Omega_n = \Omega_n(\boldsymbol{x}, \boldsymbol{y})$, $\Omega_t = \Omega_t(\boldsymbol{x}, \boldsymbol{y})$, so that possible macroscale changes of geometry are accounted for. This represents a difference with respect to previous works (Arbogast and Lehr, 2006; Shipley and Chapman, 2010), where the medium is assumed *macroscopically uniform*, i.e. the interface between subdomains is assumed to be $\boldsymbol{x}$-constant, so that the geometric structure of the medium is globally periodic, even though macroscopic variations of the fields are obviously still allowed. Note that the latter assumption is much stronger than local periodicity only, especially for tumor vascular networks, which exhibit sharp spatial heterogeneities. However, when accounting for tumor microvasculature, the local periodicity assumption still represents a restricitive assumption which does not universally hold, although, as we shall see in the following, the analysis of a suitable (possibly macroscopically varying) periodic unit can be viewed as a robust starting point to gain crucial microstructure information within the context of a tissue scale homogenized model.

We perform power series expansions of the form (1.46) for the relevant fields in (1.29-1.39); by collecting coefficients of ϵ^l for $l = 0, 1, ...$, and exploiting suitable microscale averages, we derive a closed macroscale model for the leading order fields $p_n^{(0)}$, $p_t^{(0)}$, $c_n^{(0)}$, $c_t^{(0)}$, $\boldsymbol{u}_n^{(0)}$, $\boldsymbol{u}_t^{(0)}$.
Whenever a component of the asymptotic expansion retains a dependence on the microscale $\boldsymbol{y}$, we can take its integral average, defined as follows:

$$\langle \psi \rangle_s = \frac{1}{|\Omega|} \int_{\Omega_s} \psi(\boldsymbol{x}, \boldsymbol{y}, t)\, \mathrm{d}\boldsymbol{y}, \quad s = t, n \tag{1.47}$$

where $|\Omega|$ stands for the volume of the domain and integration is performed over the local scale $\boldsymbol{y}$. Because of the $\boldsymbol{y}$-periodicity, the integral average (1.47) does not change if performed over a single representative cell only (that is, when $|\Omega|$ is replaced by the single cell volume and Ω_s by its

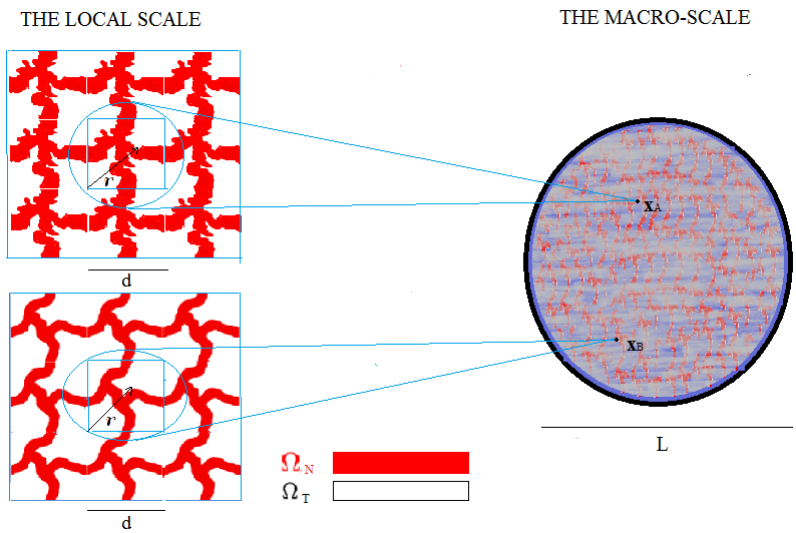

Figure 1.1: *A 2D cartoon representing the micro and macro scales. On the right hand side, the homogenized domain, where the microstructure is smoothed out, is shown. On the left hand side, the microscale is shown and the difference between the interstitial and capillary compartment is pointed out. Two possible examples of periodic units (drawn as blue circles) are depicted, related to two different macroscale points denoted by $\boldsymbol{x}_A$ and $\boldsymbol{x}_B$, to emphasize that the medium is not, in general, macroscopically uniform. In fact, the interface position vector $\boldsymbol{r}$ related to the same (homologous by $\boldsymbol{y}$-periodicity) local point is varying with respect to $\boldsymbol{x}$, that is $\boldsymbol{r}(\boldsymbol{x}_A, \boldsymbol{y}) \neq \boldsymbol{r}(\boldsymbol{x}_B, \boldsymbol{y})$. Whenever the medium exhibits such variations, one cell problem for every $\boldsymbol{x}$ of the homogenized domain needs to be solved.*

representative cell portion), so that, from now on, (1.47) will be regarded as a cell average. Finally, we also permit macroscale variations of the capillary radius r, such that from now on we assume:

$$\bar{\mu} = \bar{\mu}(\boldsymbol{x}), \tag{1.48}$$

that is, $\bar{\mu}$ is $\boldsymbol{y}$-constant.

1.4.1 Capillary problem

Assuming that all the fields depend on the independent variables $(\boldsymbol{x}, \boldsymbol{y})$, derivatives transform according to (1.45), so that the capillary problem in Ω_n (1.29-1.30), (1.33), (1.35-1.36), (1.38), rewrites:

$$\bar{\mu}\epsilon\nabla^2_{\boldsymbol{y}}\boldsymbol{u}_n + 2\bar{\mu}\epsilon^2\nabla_{\boldsymbol{y}}\cdot\nabla_{\boldsymbol{x}}\boldsymbol{u}_n + \bar{\mu}\epsilon^3\nabla^2_{\boldsymbol{x}}\boldsymbol{u}_n = \nabla_{\boldsymbol{y}}p_n + \epsilon\nabla_{\boldsymbol{x}}p_n \tag{1.49}$$

$$\nabla_{\boldsymbol{y}}\cdot\boldsymbol{u}_n + \epsilon\nabla_{\boldsymbol{x}}\cdot\boldsymbol{u}_n = 0 \tag{1.50}$$

$$\begin{aligned}\epsilon^2\frac{\partial c_n}{\partial t} + \nabla_{\boldsymbol{x}}\cdot\left(\epsilon^2 c_n\boldsymbol{u}_n - \epsilon A_n\nabla_{\boldsymbol{y}}c_n - \epsilon^2 A_n\nabla_{\boldsymbol{x}}c_n\right)\\ +\nabla_{\boldsymbol{y}}\cdot\left(\epsilon c_n\boldsymbol{u}_n - A_n\nabla_{\boldsymbol{y}}c_n - \epsilon A_n\nabla_{\boldsymbol{x}}c_n\right) =0\end{aligned} \tag{1.51}$$

equipped with interface conditions on Γ of the form:

$$(\epsilon c_n \boldsymbol{u}_n - A_n \nabla_{\boldsymbol{y}} c_n - \epsilon A_n \nabla_{\boldsymbol{x}} c_n) \cdot \boldsymbol{n} = \epsilon^2 \Phi_d \text{ on } \Gamma \tag{1.52}$$

$$\boldsymbol{u}_n \cdot \boldsymbol{n} = \epsilon \bar{\Phi}_b \tag{1.53}$$

$$-\phi \left[(\boldsymbol{n} \cdot \nabla_{\boldsymbol{y}}) \boldsymbol{u}_{\boldsymbol{n}}\right] \cdot \boldsymbol{\tau} - \epsilon \phi \left[(\boldsymbol{n} \cdot \nabla_{\boldsymbol{x}}) \boldsymbol{u}_n\right] \cdot \boldsymbol{\tau} = \boldsymbol{u}_n \cdot \boldsymbol{\tau} \text{ on } \Gamma. \tag{1.54}$$

Our aim is to determine a closed problem for the zero-th order fields $p_n^{(0)}$, $\left\langle \boldsymbol{u}_n^{(0)} \right\rangle_n$, $c_n^{(0)}$. We start considering the fluid flow in the capillaries; collecting terms of order ϵ^0 in (1.49) we get

$$\nabla_{\boldsymbol{y}} p_n^{(0)} = 0 \rightarrow p_n^{(0)} = p_n^{(0)}(\boldsymbol{x}, t) \tag{1.55}$$

Therefore, the leading order pressure field in the capillaries is $\boldsymbol{y}$-constant. Equating coefficients of ϵ^1 in (1.49) and ϵ^0 in (1.50), (1.53), (1.54), we obtain the following Stokes-type boundary value problem for $(\boldsymbol{u}_n^{(0)}, p_n^{(1)})$:

$$\nabla_{\boldsymbol{y}} p_n^{(1)} - \bar{\mu} \nabla_{\boldsymbol{y}}^2 \boldsymbol{u}_n^{(0)} = -\nabla_{\boldsymbol{x}} p_n^{(0)} \text{ in } \Omega_n \tag{1.56}$$

$$\nabla_{\boldsymbol{y}} \cdot \boldsymbol{u}_n^{(0)} = 0 \text{ in } \Omega_n \tag{1.57}$$

$$\boldsymbol{u}_n^{(0)} \cdot \boldsymbol{n} = 0 \text{ on } \Gamma \tag{1.58}$$

$$-\phi \left[(\boldsymbol{n} \cdot \nabla_{\boldsymbol{y}}) \boldsymbol{u}_n^{(0)}\right] \cdot \boldsymbol{\tau} = \boldsymbol{u}_n^{(0)} \cdot \boldsymbol{\tau} \text{ on } \Gamma \tag{1.59}$$

Now we exploit linearity of equations (1.56-1.59) together with (1.55) to formulate the following ansatz for the solution:

$$\boldsymbol{u}_n^{(0)}(\boldsymbol{x}, \boldsymbol{y}, t) = -\mathsf{W}(\boldsymbol{x}, \boldsymbol{y}) \nabla_{\boldsymbol{x}} p_n^{(0)}(\boldsymbol{x}, t) \tag{1.60}$$

$$p_n^{(1)}(\boldsymbol{x}, \boldsymbol{y}) = -\boldsymbol{P}_n(\boldsymbol{x}, \boldsymbol{y}) \cdot \nabla_{\boldsymbol{x}} p_n^{(0)}(\boldsymbol{x}, t) + \tilde{p}(\boldsymbol{x}, t), \tag{1.61}$$

where the cell fields $(\mathsf{W}, \boldsymbol{P}_n)$ satisy the following Stokes' type problem:

$$\nabla_{\boldsymbol{y}} \boldsymbol{P}_{\boldsymbol{n}} = \bar{\mu} \nabla_{\boldsymbol{y}}^2 \mathsf{W}^{\mathsf{T}} + \mathsf{I} \quad \text{in } \Omega_n \tag{1.62}$$

$$\nabla_{\boldsymbol{y}} \cdot \mathsf{W}^{\mathsf{T}} = 0 \quad \text{in } \Omega_n \tag{1.63}$$

$$\mathsf{W}^{\mathsf{T}} \boldsymbol{n} = 0 \quad \text{on } \Gamma \tag{1.64}$$

$$-\phi[(\nabla_{\boldsymbol{y}} \mathsf{W}^{\mathsf{T}}) \boldsymbol{n}] \boldsymbol{\tau} = \mathsf{W}^{\mathsf{T}} \boldsymbol{\tau} \quad \text{on } \Gamma \tag{1.65}$$

The above system of partial differential equations is supplemented by periodicity conditions in $\boldsymbol{y}$ together with suitable conditions that guarantee uniqueness for the auxiliary vector $\boldsymbol{P}_n$, for example:

$$\langle \boldsymbol{P}_n \rangle_n = 0. \tag{1.66}$$

We are now able to provide a macroscale equation for the average capillary velocity $\left\langle \boldsymbol{u}_n^{(0)} \right\rangle_n$. Integrating (1.60) over Ω_n we obtain:

$$\left\langle \boldsymbol{u}_n^{(0)} \right\rangle_n = -\mathsf{K}\nabla_{\boldsymbol{x}} p_n^{(0)} \tag{1.67}$$

where K is the second order permeability tensor for the capillary flow defined by:

$$\mathsf{K} = \langle W \rangle_n \,, \tag{1.68}$$

or, componentwise,

$$K_{ij} = \frac{1}{|\Omega_n|} \int_{\Omega_n} W_{ij} \, \mathrm{d}\boldsymbol{y} \quad i,j \in (1,2,3).$$

The average velocity profile in the capillaries thus obeys an anisotropic Darcy's law at the macroscale: the flow is driven by the leading order pressure in the capillaries $p_n^{(0)}$, whereas the microstructure is encoded in the permeability tensor K.

To obtain a macroscale equation for $p_n^{(0)}$, we collect the coefficients of order ϵ in (1.50):

$$\nabla_{\boldsymbol{x}} \cdot \boldsymbol{u}_n^{(0)} = -\nabla_{\boldsymbol{y}} \cdot \boldsymbol{u}_n^{(1)}. \tag{1.69}$$

Integral average of condition (1.69) gives:

$$\left\langle \nabla_{\boldsymbol{x}} \cdot \boldsymbol{u}_n^{(0)} \right\rangle_n = -\left\langle \nabla_{\boldsymbol{y}} \cdot \boldsymbol{u}_n^{(1)} \right\rangle_n = -\frac{1}{|\Omega_n|} \int_{\Gamma} \boldsymbol{u}_n^{(1)} \cdot \boldsymbol{n} \, \mathrm{dS}_y, \tag{1.70}$$

where we used the divergence theorem in $\boldsymbol{y}$ and exploited $\boldsymbol{y}$-periodicity. Further, the ϵ^1 contribution in the interface condition (1.53) yields:

$$\boldsymbol{u}_n^{(1)} \cdot \boldsymbol{n} = \bar{\Phi}_b^{(0)} \quad \text{on } \Gamma, \tag{1.71}$$

where $\bar{\Phi}_b^{(0)} := \bar{\Phi}_b(p_n^{(0)}, p_t^{(0)}, c_n^{(0)}, c_t^{(0)})$, such that

$$\left\langle \nabla_{\boldsymbol{x}} \cdot \boldsymbol{u}_n^{(0)} \right\rangle_n = -\frac{1}{|\Omega_n|} \int_{\Gamma} \bar{\Phi}_b^{(0)} \, \mathrm{dS}_y. \tag{1.72}$$

In order to obtain a scalar equation for the leading order pressure $p_n^{(0)}$, it is convenient to exploit the previously derived linear relationship between the leading order capillary velocity and pressure (1.67). We first make use of the generalized Reynold's transport theorem (Holmes, 1995) with respect to $\boldsymbol{x}$ to relate the cell average of the macroscale divergence of the leading order velocity field $\boldsymbol{u}_n^{(0)}$ to the divergence of its average (which are in principle different because $\Omega_n = \Omega_n(\boldsymbol{x}, \boldsymbol{y})$), that is:

$$\nabla_{\boldsymbol{x}} \cdot \left\langle \boldsymbol{u}_n^{(0)} \right\rangle_n = \left\langle \nabla_{\boldsymbol{x}} \cdot \boldsymbol{u}_n^{(0)} \right\rangle_n + \frac{1}{|\Omega_n|} \int_{\Omega_n} \nabla_{\boldsymbol{y}} \cdot \left((\nabla_{\boldsymbol{x}} \boldsymbol{y}) \boldsymbol{u}_n^{(0)} \right) \, \mathrm{d}\boldsymbol{y}. \tag{1.73}$$

Application of the divergence theorem in $\boldsymbol{y}$ in the right hand side of (1.73) yields:

$$\nabla_{\boldsymbol{x}} \cdot \left\langle \boldsymbol{u}_n^{(0)} \right\rangle_n = \left\langle \nabla_{\boldsymbol{x}} \cdot \boldsymbol{u}_n^{(0)} \right\rangle_n + \frac{1}{|\Omega_n|} \int_\Gamma \boldsymbol{u}_n^{(0)} \cdot \boldsymbol{q} \, \mathrm{dS}_y, \tag{1.74}$$

where, according to preexisting literature in multiscale analysis (see, e.g. Burridge and Keller (1981); Holmes (1995); Penta et al. (2014)), we exploited the following notation:

$$\boldsymbol{q} := (\nabla_{\boldsymbol{x}} \boldsymbol{r}(\boldsymbol{x}, \boldsymbol{y}))^{\mathsf{T}} \boldsymbol{n}, \tag{1.75}$$

where $\boldsymbol{r}(\boldsymbol{x}, \boldsymbol{y}) = \boldsymbol{y}(\boldsymbol{x})|_\Gamma$ denotes the interface position vector (see figure 1.1). Substituting equations (1.67) and (1.72) into (1.74) we finally obtain:

$$-\nabla_{\boldsymbol{x}} \cdot \left\langle \boldsymbol{u}_n^{(0)} \right\rangle_n = \nabla_{\boldsymbol{x}} \cdot \left(\mathsf{K} \nabla_{\boldsymbol{x}} p_n^{(0)} \right) = \frac{1}{|\Omega_n|} \int_\Gamma (\bar{\Phi}_b^{(0)} - \boldsymbol{u}_n^{(0)} \cdot \boldsymbol{q}) \, \mathrm{dS}_y. \tag{1.76}$$

The fluid flow in the capillaries compartment is not incompressible at the macroscale. The effective source term appearing on the right hand side of (1.76) is firstly due to the leading order blood flux $\bar{\Phi}_b^{(0)}$. Hence, the microscale exchange between the interstitial and capillary compartment across the interface Γ translates into a volumetric contribution on the global length scale. The second term at the right hand side of (1.76) is the apparent flux due to possible variations of the microscale geometry with respect to the macroscale $\boldsymbol{x}$.

A macroscale equation for the leading order concentration in the capillaries is obtained collecting coefficients of ϵ^0 in (1.51), (1.52):

$$\nabla_{\boldsymbol{y}}^2 c_n^{(0)} = 0 \qquad \text{in } \Omega_n \tag{1.77}$$

$$\nabla_{\boldsymbol{y}} c_n^{(0)} \cdot \boldsymbol{n} = 0 \qquad \text{on } \Gamma. \tag{1.78}$$

This is a Laplace boundary value problem, with periodicity condition in $\boldsymbol{y}$ and homogeneous Neumann condition on Γ, whose solution

$$c_n^{(0)} = c_n^{(0)}(\boldsymbol{x}, t) \tag{1.79}$$

is constant with respect to $\boldsymbol{y}$. Collecting terms of order ϵ^1 in (1.51), (1.52) we obtain the following differential problem for $c_n^{(1)}$:

$$\nabla_{\boldsymbol{y}}^2 c_n^{(1)} = 0 \quad \text{in } \Omega_n \tag{1.80}$$

$$\nabla_{\boldsymbol{y}} c_n^{(1)} \cdot \boldsymbol{n} = -\nabla_{\boldsymbol{x}} c_n^{(0)} \cdot \boldsymbol{n} \quad \text{on } \Gamma, \tag{1.81}$$

where we accounted for the zero-th order incompressibility costraint (1.57) and for (1.79) to obtain equation (1.80), whereas (1.58) was exploited to get the interface condition (1.81). The solution

of (1.80-1.81) is unique up to an arbitrary $\boldsymbol{y}$-constant function; as the leading order concentration $c_n^{(0)}$ is locally constant (1.79) and the problem is linear, we can state the following ansatz for the solution:

$$c_n^{(1)} = -\boldsymbol{a} \cdot \nabla_{\boldsymbol{x}} c_n^{(0)} + \bar{c}(\boldsymbol{x}, t), \tag{1.82}$$

where the auxiliary vector $\boldsymbol{a}(\boldsymbol{x}, \boldsymbol{y})$ solves the cell problem:

$$\nabla_{\boldsymbol{y}}^2 \boldsymbol{a} = 0 \quad \text{in } \Omega_n \tag{1.83}$$

$$(\nabla_{\boldsymbol{y}} \boldsymbol{a})\boldsymbol{n} = \boldsymbol{n} \quad \text{on } \Gamma \tag{1.84}$$

As previously, a further condition for $\boldsymbol{a}$ is required to ensure uniqueness, for example

$$\langle \boldsymbol{a} \rangle_n = 0. \tag{1.85}$$

Now we seek for a macroscale equation for the leading order concentration in the capillaries $c_n^{(0)}$. We start by equating ϵ^2 coefficients in (1.51),(1.52) to get:

$$\begin{aligned} \frac{\partial c_n^{(0)}}{\partial t} + \nabla_{\boldsymbol{x}} \cdot \left(c_n^{(0)} \boldsymbol{u}_n^{(0)}\right) - A_n \nabla_{\boldsymbol{x}} \cdot \left(\nabla_{\boldsymbol{y}} c_n^{(1)}\right) - A_n \nabla_{\boldsymbol{x}}^2 c_n^{(0)} + \nabla_{\boldsymbol{y}} \cdot \left(c_n^{(0)} \boldsymbol{u}_n^{(1)}\right) \\ + \nabla_{\boldsymbol{y}} \cdot \left(c_n^{(1)} \boldsymbol{u}_n^{(0)}\right) - A_n \nabla_{\boldsymbol{y}}^2 c_n^{(2)} - A_n \nabla_{\boldsymbol{y}} \cdot \left(\nabla_{\boldsymbol{x}} c_n^{(1)}\right) = 0 \quad \text{in } \Omega_n, \end{aligned} \tag{1.86}$$

$$\left(c_n^{(0)} \boldsymbol{u}_n^{(1)} + c_n^{(1)} \boldsymbol{u}^{(0)} - A_n \nabla_{\boldsymbol{y}} c_n^{(2)} - A_n \nabla_{\boldsymbol{x}} c_n^{(1)}\right) \cdot \boldsymbol{n} = \bar{\Phi}_d^{(0)} \quad \text{on } \Gamma. \tag{1.87}$$

Integral average of (1.86) over Ω_n, when the divergence theorem together with $\boldsymbol{y}$-periodicity are enforced, yields:

$$\begin{aligned} \frac{\partial c_n^{(0)}}{\partial t} + \left\langle \nabla_{\boldsymbol{x}} \cdot \left(c_n^{(0)} \boldsymbol{u}_n^{(0)}\right) \right\rangle_n - A_n \nabla_{\boldsymbol{x}}^2 c_n^{(0)} \\ + \frac{1}{|\Omega_n|} \int_\Gamma \bar{\Phi}_d^{(0)} \, \mathrm{dS}_y - A_n \left\langle \nabla_{\boldsymbol{x}} \cdot \left(\nabla_{\boldsymbol{y}} c_n^{(1)}\right) \right\rangle_n = 0. \end{aligned} \tag{1.88}$$

The interface contributions have been evaluated by means of (1.87) and condition (1.79) has been explicitly exploited. The resulting macroscale equation (1.88) can be rewritten exploiting the Reynolds' transport theorem in $\boldsymbol{x}$ and using the solution for $c_n^{(1)}$ (1.82), so that, rearranging terms, we finally obtain:

$$\begin{aligned} \frac{\partial c_n^{(0)}}{\partial t} + \nabla_{\boldsymbol{x}} \cdot \left(c_n^{(0)} \left\langle \boldsymbol{u}_n^{(0)} \right\rangle_n - \mathsf{D}_n \nabla_{\boldsymbol{x}} c_n^{(0)}\right) - \tilde{\boldsymbol{u}}_n \cdot \nabla_{\boldsymbol{x}} c_n^{(0)} = \\ = r_n c_n^{(0)} - \frac{1}{|\Omega_n|} \int_\Gamma \bar{\Phi}_d^{(0)} \, \mathrm{dS}_y, \end{aligned} \tag{1.89}$$

$$r_n := \frac{1}{|\Omega_n|} \int_\Gamma \boldsymbol{u}_n^{(0)} \cdot \boldsymbol{q} \, \mathrm{dS}_y; \quad \tilde{\boldsymbol{u}}_n := \frac{A_n}{|\Omega_n|} \int_\Gamma (\nabla_{\boldsymbol{y}} \boldsymbol{a}) \boldsymbol{q} \, \mathrm{dS}_y, \tag{1.90}$$

$$\mathsf{D}_n := A_n \left(\mathsf{I} - \frac{1}{|\Omega_n|} \int_{\Omega_n} (\nabla_{\boldsymbol{y}} \boldsymbol{a})^{\mathsf{T}} \, \mathrm{d}\boldsymbol{y} \right), \tag{1.91}$$

or, componentwise

$$D_n^{ij} = A_n \left(\delta_{ij} - \frac{1}{|\Omega_n|} \int_{\Omega_n} \frac{\partial a_j}{\partial y_i} \, \mathrm{d}\boldsymbol{y} \right) = A_n \left(\delta_{ij} - \frac{1}{|\Omega_n|} \int_{\Gamma} a_j n_i \, \mathrm{dS}_y \right), \; i, j \in (1, 2, 3).$$

Here, the contributions due to the scalar r_n and the vector $\tilde{\boldsymbol{u}}_n$ can be viewed as effective reaction factor and correction transport velocity, respectively, due to slow modulation of the interface Γ. The second order tensor D_n represents the effective diffusivity tensor for the capillary compartment.

The differential problem given by (1.67,1.76,1.89) (even when (1.60) is used to express $\boldsymbol{u}_n^{(0)}$ as a function of $p_n^{(0)}$) for the capillaries variables $\left\langle \boldsymbol{u}_n^{(0)} \right\rangle_n, c_n^{(0)}, p_n^{(0)}$, is not a closed system, because the blood and drug fluxes $\Phi_b^{(0)}$ and $\Phi_d^{(0)}$ depend on the interstitial variables too. Hence, we proceed to derive the macroscale differential system for the interstitial compartment, to write down a closed coupled problem for both interstitial and capillary variables.

1.4.2 Interstitial problem

The equations (1.31,1.32,1.34) for fluid and drug transport in Ω_t, after the two-scales reformulations, read:

$$\epsilon \boldsymbol{u}_t = -\bar{\kappa} \nabla_{\boldsymbol{y}} p_t - \epsilon \bar{\kappa} \nabla_{\boldsymbol{x}} p_t \quad \text{in } \Omega_t \tag{1.92}$$

$$\nabla_{\boldsymbol{y}} \cdot \boldsymbol{u}_t + \epsilon \nabla_{\boldsymbol{x}} \cdot \boldsymbol{u}_t = 0 \quad \text{in } \Omega_t \tag{1.93}$$

$$\begin{aligned} &\epsilon^2 \frac{\partial c_t}{\partial t} + \nabla_{\boldsymbol{x}} \cdot \left(\epsilon^2 c_t \boldsymbol{u}_n - \epsilon A_n \nabla_{\boldsymbol{y}} c_t - \epsilon^2 A_t \nabla_{\boldsymbol{x}} c_t \right) \\ &+ \nabla_{\boldsymbol{y}} \cdot \left(\epsilon c_t \boldsymbol{u}_n - A_t \nabla_{\boldsymbol{y}} c_t - \epsilon A_t \nabla_{\boldsymbol{x}} c_t \right) = -\epsilon^2 \bar{h}(c_t) \end{aligned} \tag{1.94}$$

with interface conditions

$$\left(\epsilon c_t \boldsymbol{u}_t - A_t \nabla_{\boldsymbol{y}} c_t - \epsilon A_t \nabla_{\boldsymbol{x}} c_t \right) \cdot \boldsymbol{n}_t = -\epsilon^2 \bar{\Phi}_d \text{ on } \Gamma \tag{1.95}$$

$$\boldsymbol{u}_t \cdot \boldsymbol{n}_t = -\epsilon \bar{\Phi}_b \text{ on } \Gamma. \tag{1.96}$$

Our aim is to determine effective differential equations for the leading order interstitial fields $p_t^{(0)}$, $c_t^{(0)}$, $\left\langle \boldsymbol{u}_t^{(0)} \right\rangle_t$. We start equating coefficients of ϵ^0 in (1.92) to obtain:

$$\nabla_{\boldsymbol{y}} p_t^{(0)} = 0 \rightarrow p_t^{(0)} = p_t^{(0)}(\boldsymbol{x}, t), \tag{1.97}$$

so that the leading order interstitial pressure is locally constant.

Equating coefficients of ϵ^1 in (1.92) and of ϵ^0 in (1.93) and (1.96) we get:

$$\boldsymbol{u}_t^{(0)} = -\bar{\kappa}\nabla_{\boldsymbol{y}} p_t^{(1)} - \bar{\kappa}\nabla_{\boldsymbol{x}} p_t^{(0)} \text{ in } \Omega_t \tag{1.98}$$

$$\nabla_{\boldsymbol{y}} \cdot \boldsymbol{u}_t^{(0)} = 0 \text{ in } \Omega_t \tag{1.99}$$

$$\boldsymbol{u}_t^{(0)} \cdot \boldsymbol{n}_t = 0 \text{ on } \Gamma. \tag{1.100}$$

Now we can substitute relationship (1.98) into (1.99-1.100), such that, since (1.97) applies, we can write the following Laplace problem for $p_t^{(1)}$

$$\nabla_{\boldsymbol{y}}^2 p_t^{(1)} = 0 \text{ in } \Omega_t \tag{1.101}$$

$$\nabla_{\boldsymbol{y}} p_t^{(1)} \cdot \boldsymbol{n}_t = -\nabla_{\boldsymbol{x}} p_t^{(0)} \cdot \boldsymbol{n}_t \text{ on } \Gamma \tag{1.102}$$

The corresponding solvability condition

$$\int_\Gamma \nabla_{\boldsymbol{x}} p_t^{(0)} \cdot \boldsymbol{n}_t \, \mathrm{dS}_y = 0 \tag{1.103}$$

is satisfied because

$$\int_\Gamma \nabla_{\boldsymbol{x}} p_t^{(0)} \cdot \boldsymbol{n}_t \, \mathrm{dS}_y = \int_{\partial\Omega_t} \nabla_{\boldsymbol{x}} p_t^{(0)} \cdot \boldsymbol{n}_t \, \mathrm{dS}_y = \int_{\Omega_t} \nabla_{\boldsymbol{y}} \cdot \nabla_{\boldsymbol{x}} p_t^{(0)} \, \mathrm{d}\boldsymbol{y} = 0, \tag{1.104}$$

where we have used $\boldsymbol{y}$-periodicity and the divergence theorem, as well as the fact that $p_t^{(0)}$ is locally constant (1.97).

Now we exploit the linearity of the problem (1.101)-(1.102) to propose a solution of the form:

$$p_t^{(1)} = -\boldsymbol{P}_t(\boldsymbol{x}, \boldsymbol{y}) \cdot \nabla_{\boldsymbol{x}} p_t^{(0)} + \tilde{p}_t(\boldsymbol{x}), \tag{1.105}$$

where the auxiliary vector $\boldsymbol{P}_t$ solves the following cell problems:

$$\nabla_{\boldsymbol{y}}^2 \boldsymbol{P}_t = 0 \qquad \text{in } \Omega_t \tag{1.106}$$

$$(\nabla_{\boldsymbol{y}} \boldsymbol{P}_t)\boldsymbol{n}_t = \boldsymbol{n}_t \qquad \text{on } \Gamma. \tag{1.107}$$

The above system of equations is supplemented by periodicity conditions in $\boldsymbol{y}$ together with suitable uniqueness conditions for $\boldsymbol{P}_t$. For example we can impose:

$$\langle \boldsymbol{P}_t \rangle_t = \boldsymbol{0}. \tag{1.108}$$

An integral averaging of (1.98) over Ω_t provides the macroscale equation for the velocity in the tumor interstitium,

$$\left\langle \boldsymbol{u}_t^{(0)} \right\rangle_t = -\bar{\kappa}\mathsf{E}\nabla_{\boldsymbol{x}} p_t^{(0)}, \tag{1.109}$$

where the second order tensor E is defined by:

$$\mathsf{E}\colon = \mathsf{I} - \frac{1}{|\Omega_t|}\int_{\Omega_t} (\nabla_y \boldsymbol{P}_t)^{\mathsf{T}}\, \mathrm{d}\boldsymbol{y}, \tag{1.110}$$

or, in component notation:

$$E_{ij} = \delta_{ij} - \frac{1}{|\Omega_t|}\int_{\Omega_t} \frac{\partial P_t^j}{\partial y_i}\, \mathrm{d}\boldsymbol{y} = \delta_{ij} + \frac{1}{|\Omega_t|}\int_{\Gamma} P_t^j n_i \,\mathrm{dS}_y. \tag{1.111}$$

Also in the interstitial compartment, the average velocity profile is therefore given by an anisotropic Darcy's law. Then, the whole system can be viewed as a double porous medium on the macroscale. As before, the role of the microstructure is encoded in the permeability tensor, which is given by E in the tissue interstitium.

To close the entire macroscale model, we need a macroscale equation for the leading order interstitial pressure $p_t^{(0)}$ and the drug concentration $c_t^{(0)}$. We recognize that the interstitial relationships (1.93-1.96) are formally analogous to equations (1.50-1.53), provided that the following identifications are made:

$$\boldsymbol{u}_n \to \boldsymbol{u}_t; \quad c_n \to c_t; \quad \bar{\Phi}_b \to -\bar{\Phi}_b; \quad \bar{\Phi}_d \to -\bar{\Phi}_d; \quad \frac{\partial c_n}{\partial t} \to \frac{\partial c_t}{\partial t} + \bar{h}(c_t); \quad A_n \to A_t;$$
$$|\Omega_n| \to |\Omega_t| \tag{1.112}$$

and

$$\boldsymbol{n} \to \boldsymbol{n}_t = -\boldsymbol{n}. \tag{1.113}$$

By applying in the interstitial compartment the same asymptotic analysis previously carried out for the capillary compartment in equations (1.50-1.53) to (1.93-1.96), we obtain the macroscale equations (of the form (1.76), (1.89)):

$$-\nabla_{\boldsymbol{x}} \cdot \left\langle \boldsymbol{u}_t^{(0)} \right\rangle_t = \nabla_{\boldsymbol{x}} \cdot \left(\bar{\kappa}\mathsf{E}\nabla_{\boldsymbol{x}} p_t^{(0)} \right) = -\frac{1}{|\Omega_t|}\int_{\Gamma} (\bar{\Phi}_b^{(0)} - \boldsymbol{u}_n^{(0)} \cdot \boldsymbol{q})\,\mathrm{dS}_y. \tag{1.114}$$

and

$$\begin{aligned} \frac{\partial c_t^{(0)}}{\partial t} + \nabla_{\boldsymbol{x}} \cdot \left(c_t^{(0)} \left\langle \boldsymbol{u}_t^{(0)} \right\rangle_t - \mathsf{D}_t \nabla_{\boldsymbol{x}} c_t^{(0)} \right) - \tilde{\boldsymbol{u}}_t \cdot \nabla_{\boldsymbol{x}} c_t^{(0)} = \\ = r_t c_t^{(0)} + \frac{1}{|\Omega_t|}\int_{\Gamma} \bar{\Phi}_d^{(0)}\, \mathrm{dS}_y - \bar{h}(c_t^{(0)}), \end{aligned} \tag{1.115}$$

where

$$r_t\colon = -\frac{1}{|\Omega_t|}\int_{\Gamma} \boldsymbol{u}_t^{(0)} \cdot \boldsymbol{q}\, \mathrm{dS}_y; \quad \tilde{\boldsymbol{u}}_t\colon = -\frac{A_t}{|\Omega_t|}\int_{\Gamma} (\nabla_{\boldsymbol{y}} \boldsymbol{b})\boldsymbol{q}\, \mathrm{dS}_y \tag{1.116}$$

$$\mathsf{D}_t\colon = A_t \left(\mathsf{I} - \frac{1}{|\Omega_t|}\int_{\Omega_t} (\nabla_{\boldsymbol{y}} \boldsymbol{b})^{\mathsf{T}}\, \mathrm{d}\boldsymbol{y} \right), \tag{1.117}$$

or, componentwise

$$D_t^{ij} = A_t \left(\delta_{ij} - \frac{1}{|\Omega_t|} \int_{\Omega_t} \frac{\partial b_j}{\partial y_i} \, \mathrm{d}\boldsymbol{y} \right) = A_t \left(\delta_{ij} + \frac{1}{|\Omega_t|} \int_{\Gamma} b_j n_i \, \mathrm{dS}_y \right), \quad i,j \in (1,2,3).$$

The auxiliary vector $\boldsymbol{b}(\boldsymbol{x},\boldsymbol{y})$ solves the cell problem (1.83-1.84) in the interstitial domain, namely:

$$\nabla_{\boldsymbol{y}}^2 \boldsymbol{b} = 0 \quad \text{in } \Omega_t \tag{1.118}$$

$$(\nabla_{\boldsymbol{y}} \boldsymbol{b}) \boldsymbol{n}_t = \boldsymbol{n}_t \quad \text{on } \Gamma, \tag{1.119}$$

where, again, a further condition for $\boldsymbol{b}$ is required to ensure uniqueness, for example

$$\langle \boldsymbol{b} \rangle_t = 0. \tag{1.120}$$

1.4.3 Discussion of results

The system of equations (1.76,1.67,1.89,1.114,1.109,1.115) represents the macroscale differential model for the leading order fields $p_n^{(0)}$, $\langle \boldsymbol{u}_n^{(0)} \rangle_n$, $c_n^{(0)}$, $p_t^{(0)}$, $\left\langle \boldsymbol{u}_t^{(0)} \right\rangle_t$ $c_t^{(0)}$, which describe the behavior of the fluid and drug dynamics in vascularized tissues. Summarizing, the resulting equations in non-conservative form are

$$\begin{cases} \dfrac{\partial c_n^{(0)}}{\partial t} + \left(\langle \boldsymbol{u}_n^{(0)} \rangle_n - \tilde{\boldsymbol{u}}_n \right) \cdot \nabla_{\boldsymbol{x}} c_n^{(0)} - \nabla_{\boldsymbol{x}} \cdot \left(\mathsf{D}_n \nabla_{\boldsymbol{x}} c_n^{(0)} \right) = -\mathcal{R}_n[c_n^{(0)}] & (1.121) \\ \dfrac{\partial c_t^{(0)}}{\partial t} + \left(\left\langle \boldsymbol{u}_t^{(0)} \right\rangle_t - \tilde{\boldsymbol{u}}_t \right) \cdot \nabla_{\boldsymbol{x}} c_t^{(0)} - \nabla_{\boldsymbol{x}} \cdot \left(\mathsf{D}_t \nabla_{\boldsymbol{x}} c_t^{(0)} \right) = -\mathcal{R}_t[c_t^{(0)}] & (1.122) \\ \nabla_{\boldsymbol{x}} \cdot \left(\mathsf{K} \nabla_{\boldsymbol{x}} p_n^{(0)} \right) = \dfrac{S}{|\Omega_n|} \bar{\Phi}_b^{(0)} - \dfrac{1}{|\Omega_n|} \displaystyle\int_{\Gamma} \boldsymbol{u}_n^{(0)} \cdot \boldsymbol{q} \, \mathrm{dS}_y & (1.123) \\ \nabla_{\boldsymbol{x}} \cdot \left(\bar{\kappa} \mathsf{E} \nabla_{\boldsymbol{x}} p_t^{(0)} \right) = -\dfrac{S}{|\Omega_t|} \bar{\Phi}_b^{(0)} + \dfrac{1}{|\Omega_t|} \displaystyle\int_{\Gamma} \boldsymbol{u}_t^{(0)} \cdot \boldsymbol{q} \, \mathrm{dS}_y & (1.124) \\ \langle \boldsymbol{u}_n^{(0)} \rangle_n = -\mathsf{K} \nabla_{\boldsymbol{x}} p_n^{(0)} & (1.125) \\ \left\langle \boldsymbol{u}_t^{(0)} \right\rangle_t = -\bar{\kappa} \mathsf{E} \nabla_{\boldsymbol{x}} p_t^{(0)}, & (1.126) \end{cases}$$

where the reaction operators $\mathcal{R}_n$ and $\mathcal{R}_t$ are defined as follows:

$$\mathcal{R}_n[c_n^{(0)}] := \frac{S}{|\Omega_n|} \bar{\Phi}_d^{(0)} + c_n^{(0)} \nabla_{\boldsymbol{x}} \cdot \langle \boldsymbol{u}_n^{(0)} \rangle_n - r_n c_n^{(0)} \tag{1.127}$$

$$\mathcal{R}_t[c_t^{(0)}] := -\frac{S}{|\Omega_t|} \bar{\Phi}_d^{(0)} + c_t^{(0)} \nabla_{\boldsymbol{x}} \cdot \left\langle \boldsymbol{u}_t^{(0)} \right\rangle_t - r_t c_t^{(0)} + \bar{h}(c_t^{(0)}). \tag{1.128}$$

Since the fluxes $\bar{\Phi}_b^{(0)}$, $\bar{\Phi}_d^{(0)}$ and the reaction function $\bar{h}$ depend on $p_n^{(0)}$, $p_t^{(0)}$, $c_n^{(0)}$, $c_t^{(0)}$ only, then they are also $\boldsymbol{y}$-constant and

$$S(\boldsymbol{x}) = \int_{\Gamma} \mathrm{dS}_y \tag{1.129}$$

is the unit cell capillary walls surface. The system (1.121-1.126) provides a closed homogenized model for the leading order macroscale variables, as the fields $\boldsymbol{u}_n^{(0)}$ and $\boldsymbol{u}_t^{(0)}$ can be expressed as functions of $p_n^{(0)}$ and $p_t^{(0)}$ only as follows:

$$\boldsymbol{u}_n^{(0)} = -\mathsf{W}\nabla_{\boldsymbol{x}} p_n^{(0)} \tag{1.130}$$

$$\boldsymbol{u}_t^{(0)} = -\bar{\kappa}\left(\mathsf{I} - (\nabla_{\boldsymbol{y}}\boldsymbol{P}_t)^{\mathsf{T}}\right)\nabla_{\boldsymbol{x}} p_t^{(0)}, \tag{1.131}$$

where we exploited (1.60) and (1.98,1.105), respectively.

The fluid dynamics is described by the double porous medium model (1.125,1.126), with mass exchange between compartments, due to both the blood leakage and by the effective mass flux driven by spatial heterogeneities, at the right hand sides of (1.123-1.124).

The drug dynamics is described by the advection-diffusion-reaction model (1.121-1.122). Both the interstitial and the capillary advection are due to the corresponding fluid flow, up to a correction factor that accounts for possible lack of macroscopic uniformity in the system. The reaction operators (1.127-1.128) encode the drug exchange between the two compartments, the influence of the blood leakage on the drug dynamics and the effective reaction related to macroscopic changes of the microstructure. Chemical reactions occuring in the interstitium are also taken into account.

The whole model holds over the macroscale, where the difference between interstitial and capillary compartment is immaterial. Nevertheless, the role of the microstructure can be understood in the model, as the cell volumes fractions $|\Omega_n|(\boldsymbol{x})$, $|\Omega_t|(\boldsymbol{x})$ and interface area $S(\boldsymbol{x})$ appear explicitly. Furthermore, the macroscale hydraulic conductivity and diffusion tensors $\mathsf{E}(\boldsymbol{x})$, $\mathsf{K}(\boldsymbol{x})$, $\mathsf{D}_t(\boldsymbol{x})$, $\mathsf{D}_n(\boldsymbol{x})$ defined by (1.110,1.68,1.91, 1.117), can be obtained after solving the cell problems (1.106-1.107), (1.62-1.65), (1.118-1.119), (1.83-1.84), respectively.

The unit cell geometry is needed to compute contributions that account for macroscopic changes of the microstructure (i.e. any term including the vector $\boldsymbol{q}$, defined in (1.75)). We summarize the steps needed to compute the solution of the differential problem (1.121-1.126) as follows:

1. Given a macroscale domain $\Omega_H \subset \mathbb{R}^3$ and a time interval $(0, T)$, $T \in \mathbb{R}^+$, fix suitable initial conditions in Ω_H and provide boundary conditions on $\partial\Omega_H$.

2. Define the cell geometry as a function of $\boldsymbol{x}$, such that, in particular, $|\Omega_n|(\boldsymbol{x})$, $|\Omega_t|(\boldsymbol{x})$, $S(\boldsymbol{x})$ and $\boldsymbol{r}(\boldsymbol{x}, \boldsymbol{y})$ are prescribed.

3. Fix the interstitial hydraulic conductivity $\bar{\kappa}$ and the effective viscosity $\bar{\mu}(\boldsymbol{x})$. A suitable prescription for the fluid and drug fluxes $\bar{\Phi}_b$, $\bar{\Phi}_d$ and interstitial reaction function $\bar{h}$ is also needed.

4. For every $\boldsymbol{x} \in \Omega_H$, solve the cell problems (1.106-1.107), (1.62-1.65), (1.118-1.119), (1.83-1.84) to compute the auxiliary cell variables $\boldsymbol{P}_t$, W, $\boldsymbol{b}$, $\boldsymbol{a}$.

5. Compute the correction velocities $\tilde{\boldsymbol{u}}_n$, $\tilde{\boldsymbol{u}}_t$ and the macroscale coefficients encoded in the effective tensors E, K, D_t, D_n, using definitions (1.90),(1.116), (1.110,1.68,1.91, 1.117), respectively.

6. For every $\boldsymbol{x} \in \Omega_H$ and for every $t \in (0, T)$, solve the differential problem (1.121-1.126), equipped with the macroscale boundary and interface conditions prescribed in step 1, to obtain $p_n^{(0)}$, $\left\langle \boldsymbol{u}_n^{(0)} \right\rangle_n$, $c_n^{(0)}$, $p_t^{(0)}$, $\left\langle \boldsymbol{u}_t^{(0)} \right\rangle_t$, $c_t^{(0)}$.

Remark 1.4. Note that the mathematical model we obtained can be discretized on a coarse "macro" computational grid, while the relevant physical phenomena are now captured on the tissue scale. A numerical solution of the original problem (1.29-1.39) would require an extremely fine grid to capture the detail of the microstructure, which is characterized by the intercapillary distance d. Instead, as the effective governing equations (1.121-1.126) need to be solved on the macroscale, a much coarser grid can be used. The role of the microstructure is now encoded in standard differential cell problems, to be solved for every macroscale computational node (see figure 1.1). Finally, whenever macroscopic uniformity applies, the representative cell does not depend on the macroscale any longer, and an average representative radius for the capillaries can be fixed. In this particular case, the system dramatically simplifies, as every correction factor due to macroscopic changes of the microstructure (i.e including the vector $\boldsymbol{q}$) vanishes, the cell problems depend on the microscale $\boldsymbol{y}$ only and they are to be solved once for every $\boldsymbol{x} \in \Omega_H$, to give the constant macroscale coefficients E,K,D_n,D_t.

Comparison with the model proposed by Shipley & Chapman Shipley and Chapman (2010)

The fluid and drug transport model reported in Shipley and Chapman (2010) can be obtained as a particular case of (1.121-1.126), under the following simplifying assumptions:

1. Macroscopic uniformity, i.e. the microstructure is unique; hence $\boldsymbol{q} = 0$, and r_n, r_t, $\tilde{\boldsymbol{u}}_n$, $\tilde{\boldsymbol{u}}_t$ vanish. $|\Omega_n|$, $|\Omega_t|$, S are simply constant numbers.

2. Fluid flow in the capillaries is assumed as Newtonian, i.e. $\bar{\mu}$ is constant.

3. Diffusion is negligible compared to advection, i.e. A_n , $A_t \to 0$, hence the macroscale diffusivity contribution is neglected.

4. The Starling's law for the blood flux neglects the osmotic pressure drop due to the drug concentration and a relationship of the type $\phi_b = L_p(p_n - p_t)$ is chosen. As a result, we obtain:

$$\bar{\Phi}_b^{(0)} = \bar{L}_p \left(p_n^{(0)} - p_t^{(0)} \right), \tag{1.132}$$

where

$$\bar{L}_p = \frac{L_p L^2 \mu}{d^3} \tag{1.133}$$

is the non-dimensional vessel conductivity. In this case, the fluid and drug dynamics are decoupled, as the solution for the fluid variables does not depend on the interstitial and capillary concentrations any longer.

5. The membrane law for the drug flux ignores the advection of macromolecules across the interface and a relationship of the type $\phi_d = P(c_n - c_t)$ is chosen, leading to:

$$\bar{\Phi}_d^{(0)} = \bar{\Upsilon} \left(c_n^{(0)} - c_t^{(0)} \right), \tag{1.134}$$

where

$$\bar{\Upsilon} = \frac{P \mu L}{C d^3} \tag{1.135}$$

is the non-dimensional diffusive permeability of the capillary walls.

6. Linear uptake in the interstitium, that is $h(c_t) = \gamma c_t$ and

$$\bar{h}(c_t^{(0)}) = \overline{\mathrm{Da}} c_t^{(0)}, \tag{1.136}$$

where $\overline{\mathrm{Da}}$ is the Damkohler number given by:

$$\overline{\mathrm{Da}} = \frac{\gamma L \mu}{C d^2}. \tag{1.137}$$

Whenever the above simplifying assumptions hold, the system (1.121-1.126), in conservative form, reduces to:

$$\begin{cases} \dfrac{\partial c_n^{(0)}}{\partial t} + \nabla_{\boldsymbol{x}} \cdot \left(c_n^{(0)} \left\langle \boldsymbol{u}_n^{(0)} \right\rangle_n \right) = -\dfrac{S\bar{\Upsilon}}{|\Omega_n|}(c_n^{(0)} - c_t^{(0)}) & (1.138) \\ \dfrac{\partial c_t^{(0)}}{\partial t} + \nabla_{\boldsymbol{x}} \cdot \left(c_t^{(0)} \left\langle \boldsymbol{u}_t^{(0)} \right\rangle_t \right) = \dfrac{S\bar{\Upsilon}}{|\Omega_t|}(c_n^{(0)} - c_t^{(0)}) - \overline{\mathrm{Da}} c_t^{(0)} & (1.139) \\ \nabla_{\boldsymbol{x}} \cdot \left(\mathsf{K} \nabla_{\boldsymbol{x}} p_n^{(0)} \right) = \dfrac{S}{|\Omega_n|} \bar{L}_p (p_n^{(0)} - p_t^{(0)}) & (1.140) \\ \nabla_{\boldsymbol{x}} \cdot \left(\bar{\kappa} \mathsf{E} \nabla_{\boldsymbol{x}} p_t^{(0)} \right) = -\dfrac{S}{|\Omega_t|} \bar{L}_p (p_n^{(0)} - p_t^{(0)}) & (1.141) \\ \left\langle \boldsymbol{u}_n^{(0)} \right\rangle_n = -\mathsf{K} \nabla_{\boldsymbol{x}} p_n^{(0)} & (1.142) \\ \left\langle \boldsymbol{u}_t^{(0)} \right\rangle_t = -\bar{\kappa} \mathsf{E} \nabla_{\boldsymbol{x}} p_t^{(0)}. & (1.143) \end{cases}$$

Equations of the form (1.138-1.143) have been derived by Shipley and Chapman (2010) for the fluid and drug transport in vascularized tissues (up to notation issues). The cell problems related to the solutions for the effective hydraulic conductivity tensors K and E, given by (1.62-1.65) and (1.106-1.107), respectively, are exactly the same introduced above and the same is true for the various arising non-dimensional numbers, even though in Shipley and Chapman (2010) a different scaling approach is performed. In fact, accounting for relationships (1.27), (1.43) and (1.40), the non-dimensional numbers appearing in (1.138-1.143) can be equivalently rewritten as

$$\bar{\Upsilon} = \frac{PL}{Ud}, \quad \overline{\mathrm{Da}} = \frac{\gamma L}{U}, \quad \bar{L}_p = \frac{L_p L^2 \mu}{d^3}, \quad \bar{\kappa} = \frac{k}{d^2}, \tag{1.144}$$

such that, in our notation, they are defined exactly the same way as their corresponding counterparts in Shipley and Chapman (2010)[1].

Remark 1.5. Equations (1.140-1.143) exactly match the double porous medium model in Shipley and Chapman (2010), whereas (1.138-1.139) agree with one of the drug dynamics model derived by the authors [2], where the interstitial and capillary concentrations can be tracked independently. It is worth remarking that their derivation adopts a different viewpoint, as every non-dimensional number in their formulation is scaled with respect to ϵ on the basis of an *a priori* order of magnitude estimate. It is worth noting that assumption 3 is not exploited by the authors; diffusion plays a role in the derivation of the model, but does not appear at leading order. Furthermore, they discuss different types of interface conditions, including the membrane law, continuity, and jump between the interstitial and capillary concentrations across the capillary walls. As a result, they do not obtain a unique formulation for the drug dynamics, rather, several different options are presented.

[1] Up to notation issues. In Shipley and Chapman (2010), the diffusive permeability of the membrane P, the reaction uptake rate γ and the non-dimensional vessels conductivity $\bar{L}_p$ are denoted by r, λ and $\bar{R}$ respectively.

[2] Page 1484, paragraph 3.2.4, Shipley and Chapman (2010)

Nevertheless, the resulting models can be viewed as either particular or limiting cases of equations of the type (1.138-1.139), as reported in Shipley (2008).

1.5 Conclusions

In this work we have started from the balance laws (1.29-1.34), a system of partial differential equations (in non-dimensional form) for the fluid and drug transport in the tumor interstitium and its embedded microvasculature. The flow coupling across the capillary walls has been enforced by the interface conditions (1.35-1.39), which account for blood and drug transcapillary exchange across the vessels walls. We exploited the strong spatial scale separation between the tumor characteristic length and the mean intercapillary distance, to obtain a closed differential problem for the leading order quantities $p_n^{(0)}$, $p_t^{(0)}$, $c_n^{(0)}$, $c_t^{(0)}$, $\left\langle \boldsymbol{u}_n^{(0)} \right\rangle_n$, $\left\langle \boldsymbol{u}_t^{(0)} \right\rangle_t$ on the tissue scale, by means of the homogenization technique, under the assumption of local periodicity only; macroscopic variations of the microstructure are therefore allowed.

According to the resulting system of equations, the fluid flow obeys a double porous medium model, where the effective hydraulic conductivity tensors can be computed solving standard differential cell problems. Mass sources contributions account for both the effective transport between the capillary and interstitial compartments and macroscopic changes of the microvasculature.

The effective governing equations for drug transport comprise a double generalized advection-diffusion-reaction model, where the reaction operators account for the transvascular exchange of drug across the capillary walls, as well as the influence of the blood transfer and slow modulation of the microvasculature geometry. Chemical reactions which might occur in the tumor interstitium are also taken into account. The role of the microstructure is also encoded in the effective diffusivity tensors, which can be computed solving classical differential cell problems on a single unit cell.

Our main result is to provide a mathematical model that retains the most physical phenomena of the biophysical system on the tissue scale: the role of the microvasculature is recovered via the effective macroscale coefficients of the model, which can be calculated solving standard differential problems on a single cell for every macroscale point $\boldsymbol{x}$. Further, an interesting feature of our model resides in its computational convenience.

The mathematical model reported in Shipley and Chapman (2010) can be recovered from our model under a number of simplifying assumptions. Remarkable differences are that diffusion plays here a role at the tissue scale, and the interplay between fluid and drug transport is accounted for, via a general Kedem-Katchalsky model for the interface fluxes. The osmotic pressure due to the

difference in drug concentrations is retained, such that the blood and drug dynamics are coupled. Furthermore, we also permit macroscopic variations of the microstructure and compute the arising effective velocities, reactions and fluxes. In general, the main effort of the current work is in addressing more generality in the physics of the biological system, in terms of a fully non-equilibrium, non-linear formulation for the blood and drug interplay, together with possibly non-linear reactions that might occur in the tissue. The effective governing equations do not depend explicitly on specific physical regimes: however, simplified cases can be obtained performing an *a posteriori* estimate of the non-dimensional numbers, depending on the actual system at hand. Finally, local periodicity only is assumed, and the present model still apply when spatial heterogeneities, which often occur in tumor vasculatures, appear.

Nevertheless, some simplifying assumptions still apply. In particular, we did not account for a fully non-Newtonian rheology of the blood, even though (slow) variations of the relative viscosity with respect to the effective capillary radius are allowed. The microstructure can vary over the macroscale, but is fixed in time, such that we do not account for adaptation or re-modelling issues (see for example Pries et al. (1998); Owen et al. (2008)). The elastic deformability of the porous structure is neglected, even though for a certain class of tissues, the elastic (or visco-elastic) properties of the porous solid mass cannot be ignored. In this scenario, it has been shown that the hydraulic conductivity of the tissue depends also on the tissue strains (Netti et al., 2000), and poroelastic modeling approaches with anisotropic dependence of the hydraulic conductivity upon tissue deformation has been recently explored (Bottaro and Ansaldi, 2012)

This work aims to be theoretical starting point, to test both the impact of the vascular geometry and the influence of drug parameters on the tumor fluid dynamics. This mathematical framework can be exploited to simulate numerically the fluid and drug transport coupling on real tumor geometries extracted from medical images. Numerical results can be compared to clinical data to achieve validation whereas, in the long term, predictions from this model could help to improve anti-cancer strategies.

CHAPTER 2

The role of the microvascular tortuosity in tumor transport phenomena

2.1 Introduction

The bio-physical mechanisms that drive solute and blood transport through a malignant mass have inspired a large literature in the last decades, both from an experimental and from a mathematical modelling viewpoint. The ability of an injected anti-cancer or tracker molecule to reach the target cancer cells depends on several key mechanisms which can be regarded as transport *barriers*: advection in the blood vessels, leakage from the microvascular walls, transport in the interstitial space and interactions with the tumor cells membrane (Jain, 1987b). Experimental measurements, as well as validated mathematical models which highlight the determinants of tumor blood convection, can therefore play a role in the improvement of anti-cancer therapies.

The tumor system is characterized by several abnormal features, including a leaking and tortuous microvascular network (Hashizume, 2000), the lack of a functional lymphatic drenage, elevated and heterogeneous interstitial pressure through the tumor volume. Jain and Baxter (1988) developed a phenomenological mathematical model to describe the blood transport in the tumor mass. The

authors considered an isotropic spherical solid tumor, where the blood leakage through the vessels is modeled as an effective source for the interstitial Darcian fluid. As a result, they can track significant spatial variations in the interstitial pressure profile, which rapidly increases from the tumor boundary to the center, so that the pressure difference between blood vessels and tumor interstitium decreases accordingly. The blood convection is improved (i.e. the interstitial pressure is damped) by decreasing the tumor radius, the vascular hydraulic conductivity and the exchange surface-to-volume ratio and by increasing the tumor hydraulic conductivity. The model by Jain and Baxter (1988) has been experimentally validated in Boucher et al. (1990), while the role of the revelant measured blood flow determinants, as well as a discussion regarding recently developed normalization therapies, is highlighted in Jain et al. (2007).

In this work, we start from the multiscale double Darcy model developed by Shipley and Chapman (2010) for interstitial and capillary fluid transport, which is derived exploiting the sharp length scale separation between the intercapillary distance and the tumor characteristic dimensions. The model accounts for both the interstitial and blood vessels flow and the effective hydraulic conductivities are computed numerically solving the classical Laplace and Stokes' problem in a reference prototypical cell. We solved the isotropic tissue scale model for several cell geometries in order to capture the tortuosity impact on blood convection in the tumor mass. The model solution formally takes the same functional form as in Jain and Baxter (1988), but spatial variations of the microvascular pressure are allowed and new parameters which describe the capillary network hydraulic properties arise. For increasing vascular tortuosity, we predict a dramatic capillary hydraulic conductivity damp which highly compromises fluid flow within the tumor. The novel contribution of this work is the qualitative and quantitative evaluation of the vascular geometric complexity on the blood transport process. On the basis of our analysis, we suggest that anti-cancer therapies related to a blood flow improvement should focus on geometric vessels regularization.

The work is organized as follows:

- In Section 2.2 we introduce the multiscale homogenized model by Shipley and Chapman (2010), which is starting point of the present analysis.

- In section 2.3 we present and discuss the 3D numerical solution of the capillary and interstitial microscale cell problems for the macroscale isotropic setting.

- In section 2.4 we present and discuss the macroscopic model solution and the impact of the microvascular tortuosity on tumor blood convection is pointed out.

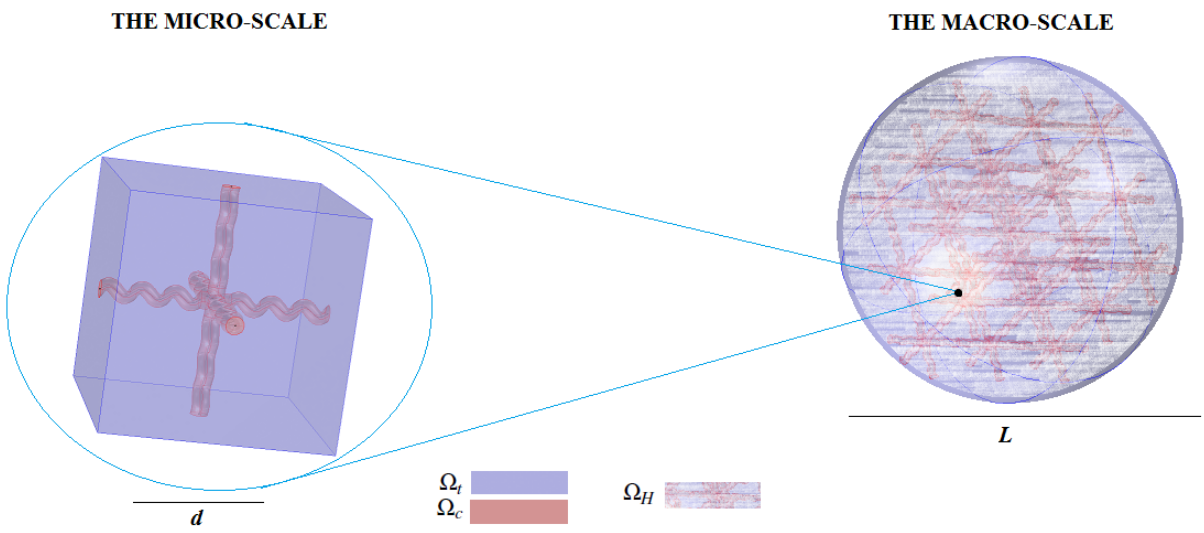

Figure 2.1: *A schematic representation of the micro and macro scales. On the left hand side, the microscale cell Ω is shown and the difference between the interstitial and capillary compartment Ω_t and Ω_c is pointed out. On the right hand side, the homogenized domain Ω_H, where the microstructure is smoothed out, is shown.*

- In section 2.5 we compare our results with those obtained by Jain and Baxter (1988) and discuss the role of the key blood flow determinants.
- In secton 2.6 concluding remarks are presented.

2.2 Mathematical Model

In a recent paper Shipley and Chapman (2010) derive a mathematical model to describe the fluid dynamics in a vascularized tumor at the tissue scale, on the basis of the multiscale homogenization technique (Sanchez-Palencia, 1983; Holmes, 1995). They define the interstitial and capillary phases as two individual compartments on the microscale, where Darcy and Stokes regimes apply, respectively. The coupling between the two compartments is provided by continuity of the blood flux, which is prescribed by means of the Starling's law, i.e. proportional to the fluid pressure drop across the vessels walls. Then, the multiple scales technique is exploited, under assumption of local periodicity, to derive a double Darcy model. The final set of equations comprises effective mass sources, accounting for the blood leakage on the macroscale, and the macroscopic fluid dynamics of both the tumor interstitium and the capillary network. The crucial assumption underneath the homogenization technique is the sharp length scale separation between the local scale, where distinct microscopic features of the physical system can be identified, and the macroscale, where only global variations of the relevant field of interest can be captured, as shown in Figure 2.1.

According to Shipley and Chapman (2010), we relate the characteristic local scale d to the

Parameter	Description	Value	Physiological range (Reference)	Value in S.I. units
L_p [cm/(mm Hg · s)]	Normalized Vessel hydraulic permeability	$2.38 \cdot 10^{-7}$	$3.6 \cdot 10^{-8} - 1.8 \cdot 10^{-6}$ (Jain et al., 2007)	$1.79 \cdot 10^{-11}$ [m/(Pa · s)]
κ [cm^2/(mm Hg · s)]	Tumor hydraulic conductivity	$2.8 \cdot 10^{-7}$	$1.7 - 3.2 \cdot 10^{-7}$ (Boucher et al., 1998)	$2.10 \cdot 10^{-13}$ [m^2/(Pa · s)]
μ [Pa · s]	Blood viscosity	$4.0 \cdot 10^{-3}$	$4.0 \cdot 10^{-3}$ (Rand et al., 1964)	$4 \cdot 10^{-3}$ [Pa · s]
Ξ [Dimensionless]	Slip coefficient	1	1 (Shipley and Chapman, 2010)	
r_c [Dimensionless]	Capillary radius	0.07		
l [Dimensionless]	One-side branch length	0.8		
h [Dimensionless]	Cylindrical link height	0.24		
l_c [Dimensionless]	Total branch length $(2l + h)$	1.84		
$\lvert\Omega\rvert$ [Dimensionless]	Cell volume $((2l + h)^3)$	6.23		
R [Dimensionless]	Tumor radius	0.5		
d [μm]	Reference micro-scale	40		$4 \cdot 10^{-5}$[m]
L [cm]	Reference macro-scale	1		10^{-2}[m]
$i.c.d.$ [μm]	Intercapillary distance $((2l + h) \cdot d)$	73.6	$61.9 - 93.7$ (Yoshii and Sugiyama, 1988)	$7.36 \cdot 10^{-5}$[m]
S/V [cm^{-1}]	Surface-to-volume ratio $(S/\lvert\Omega\rvert \cdot d^{-1})$	$92.3 - 130.4$	$50 - 250$ (Jain et al., 2007)	$9.23 - 13.04 \cdot 10^3$[m^{-1}]
D [μm]	Capillary diameter $(2r_c \cdot d)$	5.6	$4.4 - 15$ (Asaishi et al., 1981)	$5.6 \cdot 10^{-6}$[m]
R [cm]	Tumor radius (RL)	0.5	$0.5 - 2.2$ (Hahnfeldt et al., 1999)	$5 \cdot 10^{-3}$[m]
α_J [Dimensionless]	$\mathrm{R}\sqrt{\frac{L_p \mathrm{S}}{\kappa \mathrm{V}}}$		$3.5 - 17$ (Jain et al., 2007)	

Table 2.1: *Parameters values exploited for analytical analysis and numerical computing. We set non-dimensional microscale and macroscale parameters such that, once the representative lengths are chosen, their dimensional counterparts values belong to the physiological range reported in the literature.*

intercapillary distance among vessels, whereas we identify the macroscale with a representative average tumor length L. Their ratio is

$$\epsilon = \frac{d}{L} \ll 1 \tag{2.1}$$

so that we can define two independent spatial variables $\boldsymbol{x}$ and $\boldsymbol{y}$,

$$\boldsymbol{y} := \frac{\boldsymbol{x}}{\epsilon}, \tag{2.2}$$

spanning the *macro* and *micro* scale, respectively. On the microscale, because of $\boldsymbol{y}$-periodicity, the domain Ω is a single cell, which is composed by the interstitial compartment Ω_t, the capillary compartment Ω_c and the interface $\Gamma = \partial\Omega_t \cap \partial\Omega_c$. The geometric information on the microvasculature turns out to be encoded in the hydraulic conductivity tensors, which are computed solving classical microscale differential problems on the representative cell.

This analysis focuses on the impact of the geometric properties of the capillary network on blood convection in tumors. We assume that the ansatzs underlying the model by Shipley and Chapman (2010) hold: the blood flow phase is Newtonian, the osmotic pressure due to possible differences in drug concentration is neglected and macroscopic variations of the microstructure are ignored (see Penta et al. (2013), where these assumptions are relaxed).Thus, denoting the homogenized domain by $\Omega_H \subset \mathbb{R}^3$, the non-dimensional governing macroscale system of partial differential equations

which describes the fluid-dynamics of a vascularized tumor for every $\boldsymbol{x} \in \Omega_H$ reads (Shipley and Chapman, 2010):

$$\begin{cases} \nabla_{\boldsymbol{x}} \cdot (\mathsf{K}\nabla_{\boldsymbol{x}} p_c) = \dfrac{S}{|\Omega_c|}\bar{L}_p(p_c - p_t) \qquad \text{in } \Omega_H & (2.3) \\ \nabla_{\boldsymbol{x}} \cdot (\bar{\kappa}\mathsf{E}\nabla_{\boldsymbol{x}} p_t) = -\dfrac{S}{|\Omega_t|}\bar{L}_p(p_c - p_t) \qquad \text{in } \Omega_H & (2.4) \\ \boldsymbol{u}_c = -\mathsf{K}\nabla_{\boldsymbol{x}} p_c & (2.5) \\ \boldsymbol{u}_t = -\bar{\kappa}\mathsf{E}\nabla_{\boldsymbol{x}} p_t, & (2.6) \end{cases}$$

where p_c, p_t are the macroscopic capillary and interstitial pressure fields, respectively, and $\boldsymbol{u}_c$, $\boldsymbol{u}_t$ are the corresponding tissue scale Darcy velocities. The non-dimensional numbers $\bar{L}_p$ and $\bar{\kappa}$ are defined by:

$$\bar{L}_p = \frac{L_p \mu L^2}{d^3}; \quad \bar{\kappa} = \frac{\kappa\mu}{d^2}, \tag{2.7}$$

where L_p and κ are the physiological vascular hydraulic permeability and tumor hydraulic conductivity, respectively (see Table 2.1). The cell exchange surface S and subvolumes size $|\Omega_t|$ and $|\Omega_c|$ are

$$|\Omega_m| = \int_{\Omega_m} \mathrm{d}\boldsymbol{y} \qquad m = t, c, \quad S = \int_{\Gamma} \mathrm{dS}_y. \tag{2.8}$$

The tensors K and $\bar{\kappa}\mathsf{E}$ play the role of effective capillary and interstitial hydraulic conductivity and they are defined by:

$$\mathsf{K} = \langle W \rangle_c, \quad \mathsf{E} := \mathsf{I} - \left\langle (\nabla_{\boldsymbol{y}} \boldsymbol{P}^t)^{\mathsf{T}} \right\rangle_t, \tag{2.9}$$

where the brackets $\langle \bullet \rangle_m$ denote the cell integral average operator

$$\langle \bullet \rangle_m = \frac{1}{|\Omega_m|} \int_{\Omega_m} \bullet \, \mathrm{d}\boldsymbol{y} \qquad m = t, c. \tag{2.10}$$

The auxiliary velocity tensor $\mathsf{W}(\boldsymbol{y})$ and the auxiliary pressure vector $\boldsymbol{P}^t(\boldsymbol{y})$ satisfy the following *cell* problems:

$$\begin{cases} \nabla^2_{\boldsymbol{y}} \mathsf{W}^{\mathsf{T}} - \nabla_{\boldsymbol{y}} \boldsymbol{P}^c + \mathsf{I} = 0 \quad \text{in } \Omega_c & (2.11) \\ \nabla_{\boldsymbol{y}} \cdot \mathsf{W}^{\mathsf{T}} = 0 \quad \text{in } \Omega_c & (2.12) \\ \mathsf{W}^{\mathsf{T}} \boldsymbol{n} = 0 \quad \text{on } \Gamma & (2.13) \\ \mathsf{W}^{\mathsf{T}} \boldsymbol{\tau} = -\phi[(\nabla_{\boldsymbol{y}} \mathsf{W}^{\mathsf{T}})\boldsymbol{n}]\boldsymbol{\tau} \quad \text{on } \Gamma, & (2.14) \end{cases}$$

$$\begin{cases} \nabla^2_{\boldsymbol{y}} \boldsymbol{P}^t = 0 \quad \text{in } \Omega_t & (2.15) \\ (\nabla_{\boldsymbol{y}} \boldsymbol{P}^t)\boldsymbol{n} = \boldsymbol{n} \quad \text{on } \Gamma, & (2.16) \end{cases}$$

where suitable uniqueness conditions for the auxiliary pressures $\boldsymbol{P}^t$ and $\boldsymbol{P}^c$ are to be enforced. For example we can impose

$$\langle \boldsymbol{P}^c \rangle_c = 0 \quad \text{in } \Omega_c \quad \text{and} \quad \langle \boldsymbol{P}^t \rangle_t = 0 \quad \text{in } \Omega_t.$$

Exploiting the $\boldsymbol{y}$-periodicity, the problems for $\mathsf{W}(\boldsymbol{y})$ and $\boldsymbol{P}^t(\boldsymbol{y})$ are then closed by periodic conditions on the cell boundaries $\partial\Omega_c \setminus \Gamma$ and $\partial\Omega_t \setminus \Gamma$, respectively. Here, $\boldsymbol{n}$ represent the outward unit vector normal to the interface and $\boldsymbol{\tau}$ is any vector tangent to Γ. The differential problem (2.15-2.16) is an inhomogeneous Laplace problem for each component of the vector $\boldsymbol{P}^t$, whereas (2.11-2.14) is a Stokes' type boundary value problem, which is equipped by the slippery (Beavers and Joseph, 1967; Jones, 1973) interface conditions (2.14) via the non-dimensional number

$$\phi = \frac{\sqrt{\bar{\kappa}}}{\Xi}, \tag{2.17}$$

which accounts for the slip over a porous surface, where Ξ is a non dimensional parameter. According to the physiological data reported in Table 2.1

$$\phi \ll 1 \tag{2.18}$$

so that the cell problems given by (2.11-2.14) and (2.15-2.16), rewrite, componentwise:

$$\begin{cases} \dfrac{\partial^2 W_{ji}}{\partial y_k \partial y_k} + \dfrac{\partial P_i^c}{\partial y_j} + \delta_{ij} = 0 \quad \text{in } \Omega_c & (2.19) \\ \dfrac{\partial W_{ji}}{\partial y_j} = 0 \quad \text{in } \Omega_c & (2.20) \\ W_{ij} = 0 \quad \text{on } \Gamma, & (2.21) \end{cases}$$

$$\begin{cases} \dfrac{\partial^2 P_i^t}{\partial y_k \partial y_k} = 0 \quad \text{in } \Omega_t & (2.22) \\ \dfrac{\partial P_i^t}{\partial y_j} n_j = n_i \quad \text{on } \Gamma, & (2.23) \end{cases}$$

where $i, j, k = 1...3$ and summation over repeated indices is understood.

2.3 The microscale cell problems

2.3.1 The macroscopic isotropic setting

The macroscopic double-Darcy problem (2.3-2.6) is isotropic when the microscale geometry verifies the following identities:

$$\mathsf{K} = K_c \mathsf{I}, \quad K_c := \langle W_{11} \rangle_c = \langle W_{22} \rangle_c = \langle W_{33} \rangle_c \tag{2.24}$$

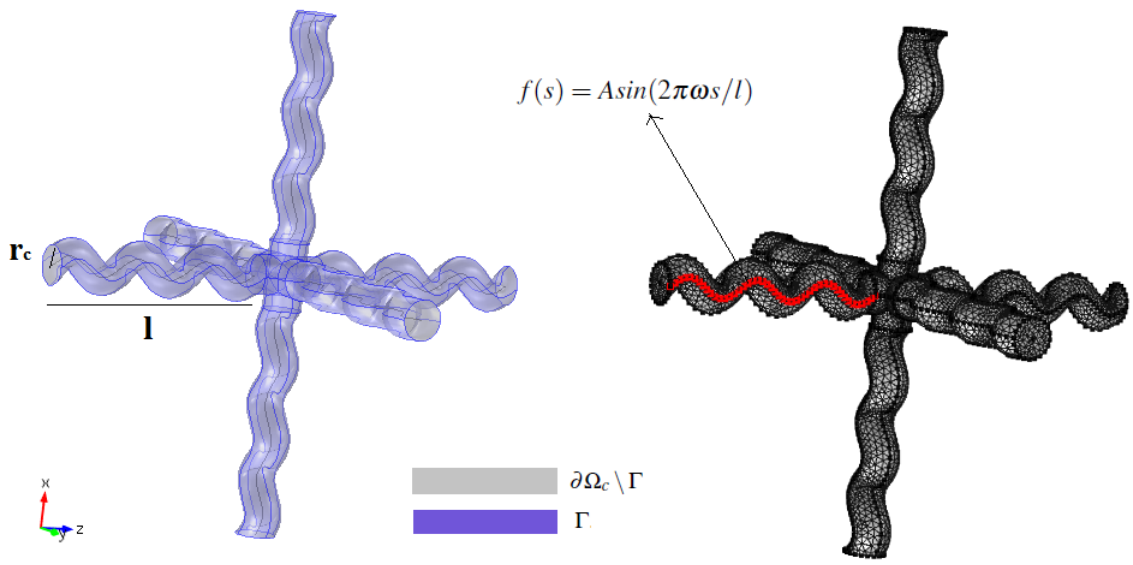

Figure 2.2: *An example of the microscale representative capillary cell portion Ω_c and its geometric features are depicted. On the left hand side, the tortuous geometry is shown, whereas r_c and l correspond to the capillary radius and the one-sided branch length, respectively. The difference between the capillary (dirichlet) walls Γ and the (periodic) outer faces $\partial\Omega_c \setminus \Gamma$ is pointed out. On the right hand side, the corresponding 3D computational mesh is shown and the analytic parametrization of the geometry is highlighted.*

$$\mathsf{E} = E_t \mathsf{I}, \quad E_t := \langle E_{11} \rangle_t = \langle E_{22} \rangle_t = \langle E_{33} \rangle_t \,. \tag{2.25}$$

This spherical characterization of the microvascular conductivity has not a physiological meaning "'per se"': it enables to account for a range of significant variations in the microstructure geometry and highlights the physical contribution of the homogenized model via a reduced number of parameters. This way, it provides quantitative results which can be compared to previous, experimentally validated isotropic models (Jain and Baxter, 1988; Boucher et al., 1990). In order to verify identities (2.24-2.25), we choose a prototypical rotation invariant microstructure, composed by three orthogonal branches, as shown in figure 2.2 and 2.3. The differential problems for W (2.19-2.21) and $\boldsymbol{P}^t$ (2.22-2.23), are three standard Stokes' and Laplace problems for $i = 1, 2, 3$ respectively and we can enforce rotation invariance to compute the solution for W and $\boldsymbol{P}^t$ by solving one Stokes' and Laplace problem only. In fact we can fix, for example, $i = 3$ in (2.19-2.21) and (2.22-2.23) without loss of generality, obtaining:

$$\begin{cases} \nabla_{\boldsymbol{y}}^2 \boldsymbol{w} - \nabla_{\boldsymbol{y}} P^c + \boldsymbol{e}_3 = 0 \quad \text{in } \Omega_c & (2.26) \\ \nabla_{\boldsymbol{y}} \cdot \boldsymbol{w} = 0 \quad \text{in } \Omega_c & (2.27) \\ \boldsymbol{w} = 0 \quad \text{on } \Gamma, & (2.28) \end{cases}$$

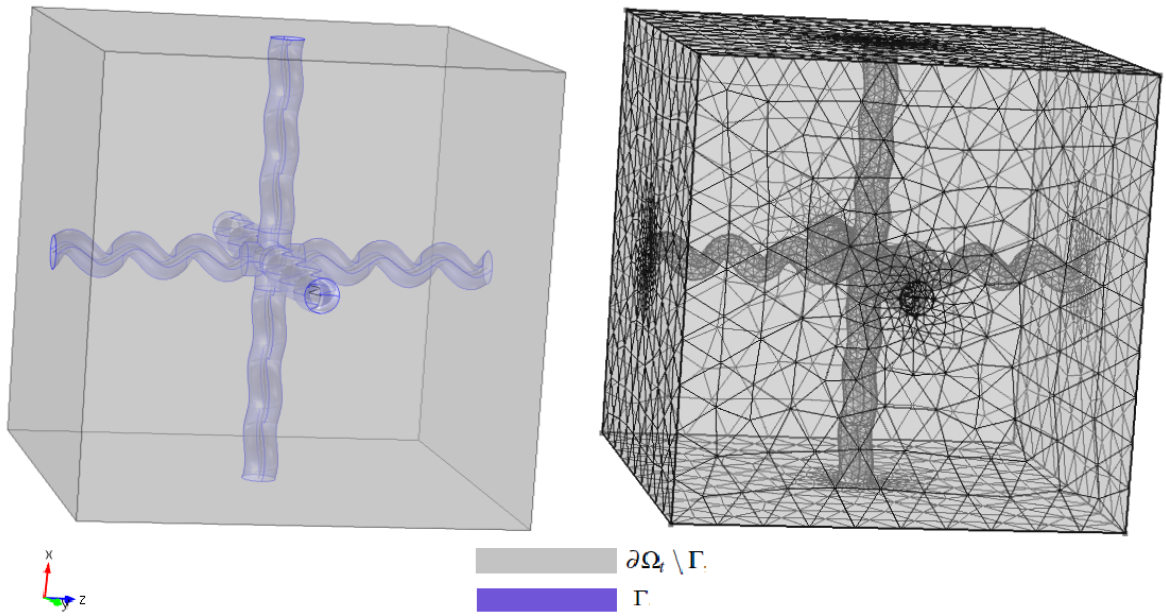

Figure 2.3: *An example of the microscale representative interstitial cell portion $\Omega_t = \Omega \setminus \Omega_c$. On the left hand side, the tortuous geometry is shown and the difference between the (Neumann) inner walls Γ and the (periodic) outer faces $\partial\Omega_t \setminus \Gamma$ is pointed out. On the right hand side, the corresponding 3D computational mesh is shown.*

$$\begin{cases} \nabla_{\boldsymbol{y}}^2 P^t = 0 \quad \text{in } \Omega_t & (2.29) \\ \nabla_{\boldsymbol{y}} P^t \cdot \boldsymbol{n} = n_3 \quad \text{on } \Gamma, & (2.30) \end{cases}$$

where we explicitly set, by components:

$$w_1 = W_{13},\ w_2 = W_{23},\ w_3 = W_{33},\ P^c = P_3^c,\ P^t = P_3^t. \tag{2.31}$$

Then, enforcing rotation invariance of the geometry with respect to the three orthogonal axes, we get

$$w_1 = W_{13} = W_{21} = W_{32}$$

$$w_2 = W_{23} = W_{31} = W_{12}$$

$$w_3 = W_{33} = W_{11} = W_{22}, \tag{2.32}$$

$$\frac{\partial P^t}{\partial y_1} = \frac{\partial P_3^t}{\partial y_1} = \frac{\partial P_1^t}{\partial y_2} = \frac{\partial P_2^t}{\partial y_3}$$

$$\frac{\partial P^t}{\partial y_2} = \frac{\partial P_3^t}{\partial y_2} = \frac{\partial P_1^t}{\partial y_3} = \frac{\partial P_2^t}{\partial y_1}$$

$$\frac{\partial P^t}{\partial y_3} = \frac{\partial P_3^t}{\partial y_3} = \frac{\partial P_1^t}{\partial y_1} = \frac{\partial P_2^t}{\partial y_2} \tag{2.33}$$

and the full solution for K and E can be recovered once definitions (2.9) are exploited.

In order to test the impact of the microvasculature tortuosity on the blood flow, we perform our analysis varying the geometrical configuration of Ω_c (and Ω_t accordingly). In particular, we design the center line of every branch by an analytical parametrization of the type:

$$f(s) = A \sin(2\pi\omega s/l), \tag{2.34}$$

where A represents the amplitude, ω the spatial frequency, l the one-sided branch length and s the local parametrization of the spatial coordinate, such that

$$0 \leq s \leq l,$$

as depicted in Figure 2.2. We identify the geometrical *tortuosity* by the two parameters ω and A.

Next we numerically solve the capillary and interstitial cell problems (2.19-2.21) and (2.22-2.23); then, exploiting the macroscopic isotropy (2.24-2.25), the analytical solution of the macroscale model (2.3-2.6) is provided for an isolated spherical tumor.

2.3.2 The capillary cell problem

We are interested in varying the geometrical tortuosity parameters ω and A of the reference cell and numerically compute the corresponding values of K (in particular K_c), S, $|\Omega_c|$. The results are reported in Table 2.2.

The numerical solution of the Stokes' problem (2.26-2.28) yields the usual parabolic profile for the straight cylindrical shaped reference configuration (see Figure 2.4). In this case, the solution, which is non-zero in the branch directed along $\boldsymbol{e}_3$ only (that is, the direction of the volume force), is almost equal to the one that would be experienced by a low-Reynolds number Newtonian fluid at unit viscosity, flowing in a cylindrical tube of radius r_c and subject to a uniform unit volume force along its axis, with periodic boundary conditions, i.e:

$$w_3 = \frac{r_c^2 - r_l^2}{4}, \quad w_1 = w_2 = 0, \quad 0 \leq r_l \leq r_c, \tag{2.35}$$

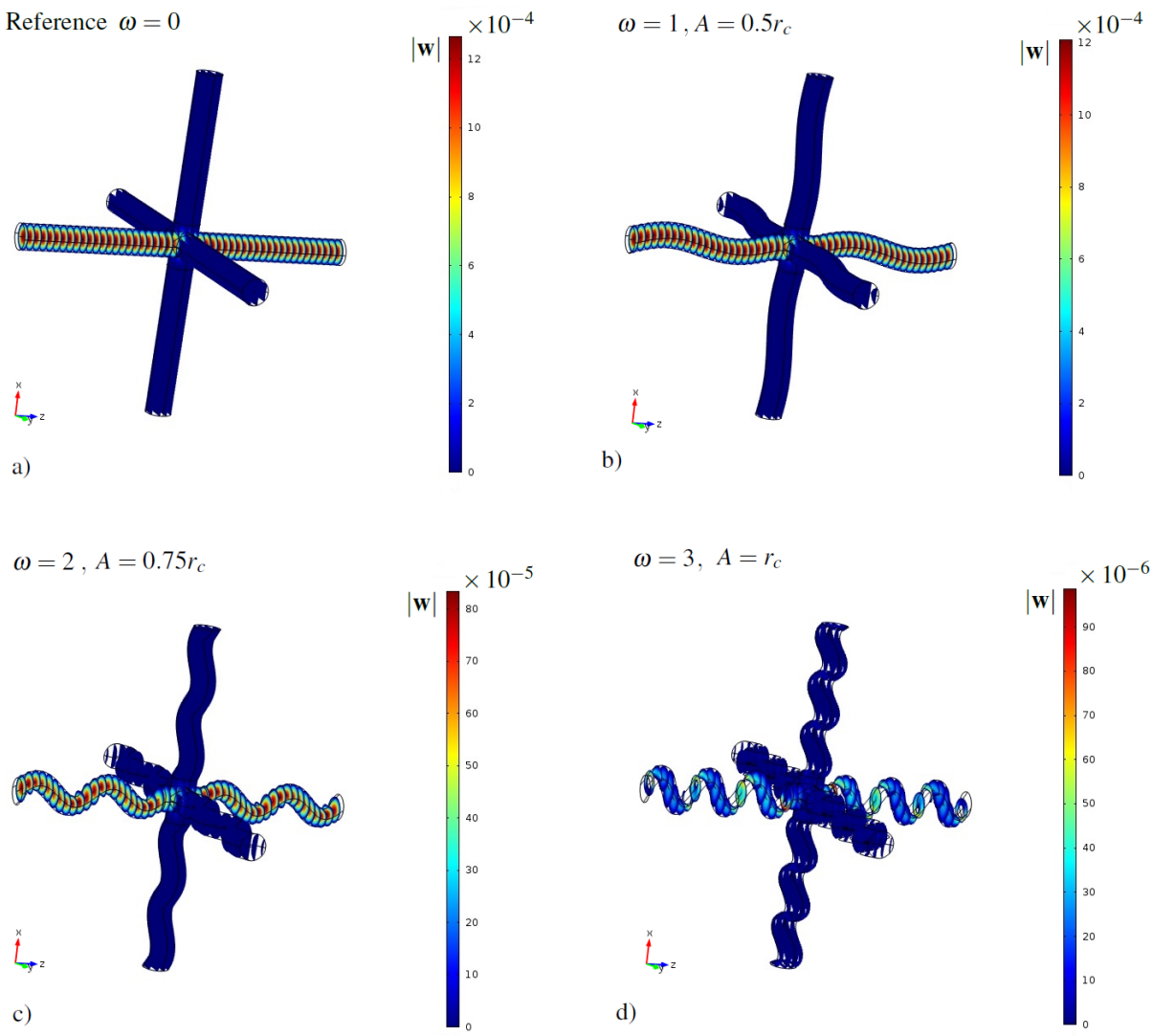

Figure 2.4: *Examples of numerical results for $\boldsymbol{w}$ in terms of its magnitude, where four representative geometries at increasing tortuosity are chosen. The solution retains a pseudo-parabolic profile for small pertubation of the reference configuration, whereas a sharp non-linear decrease with respect to geometrical tortuosity is observed at higher frequency.*

ω	A	$\lvert\Omega_c\rvert$	$\lvert\Omega_t\rvert(\lvert\Omega\rvert - \lvert\Omega_c\rvert)$	S	$K_c\,(\langle w_3\rangle_c)$	$\langle w_1\rangle_c$	$\langle w_2\rangle_c$	Kozeny constant
0	0	$8.1 \cdot 10^{-2}$	6.149	2.30	$2.20 \cdot 10^{-4}$	$2.83 \cdot 10^{-9}$	$2.89 \cdot 10^{-10}$	5.6
1	$0.25r_c$	$8.0 \cdot 10^{-2}$	6.15	2.30	$2.17 \cdot 10^{-4}$	$3.81 \cdot 10^{-8}$	$3.53 \cdot 10^{-8}$	5.6
1	$0.5r_c)$	$7.9 \cdot 10^{-2}$	6.151	2.30	$2.06 \cdot 10^{-4}$	$6.57 \cdot 10^{-8}$	$6.22 \cdot 10^{-8}$	5.7
1	$0.75r_c)$	$7.8 \cdot 10^{-2}$	6.152	2.31	$1.90 \cdot 10^{-4}$	$8.17 \cdot 10^{-8}$	$7.86 \cdot 10^{-8}$	6.0
1	r_c	$7.6 \cdot 10^{-2}$	6.154	2.32	$1.69 \cdot 10^{-4}$	$8.42 \cdot 10^{-8}$	$8.22 \cdot 10^{-8}$	6.3
2	$0.25r_c$	$7.9 \cdot 10^{-2}$	6.151	2.30	$2.05 \cdot 10^{-4}$	$6.26 \cdot 10^{-8}$	$5.85 \cdot 10^{-8}$	5.7
2	$0.5r_c$	$7.6 \cdot 10^{-2}$	6.154	2.33	$1.63 \cdot 10^{-4}$	$8.52 \cdot 10^{-8}$	$8.02 \cdot 10^{-8}$	6.5
2	$0.75r_c$	$7.2 \cdot 10^{-2}$	6.158	2.42	$1.08 \cdot 10^{-4}$	$4.64 \cdot 10^{-8}$	$4.85 \cdot 10^{-8}$	8.2
2	r_c	$6.9 \cdot 10^{-2}$	6.161	2.57	$6.24 \cdot 10^{-5}$	$2.17 \cdot 10^{-8}$	$2.30 \cdot 10^{-8}$	11.5
3	$0.25r_c$	$7.8 \cdot 10^{-2}$	6.152	2.32	$1.84 \cdot 10^{-4}$	$7.54 \cdot 10^{-8}$	$7.39 \cdot 10^{-8}$	6.1
3	$0.5r_c$	$7.2 \cdot 10^{-2}$	6.158	2.53	$7.71 \cdot 10^{-5}$	$3.66 \cdot 10^{-8}$	$4.51 \cdot 10^{-8}$	10.5
3	$0.75r_c$	$6.8 \cdot 10^{-2}$	6.162	2.82	$2.02 \cdot 10^{-5}$	$-2.64 \cdot 10^{-9}$	$3.60 \cdot 10^{-9}$	29.0
3	r_c	$6.5 \cdot 10^{-2}$	6.165	3.25	$4.89 \cdot 10^{-6}$	$-2.63 \cdot 10^{-8}$	$6.82 \cdot 10^{-9}$	80.0

Table 2.2: *Computational results for the non-dimensional capillary hydraulic conductivity K_c, cell exchange surface S and capillary cell volume portion $|\Omega_c|$ for thirteen cells of increasing tortuosity. Non-diagonal values of* K *are negligible with respect to K_c.*

where r_l denote the local radial coordinate. As a consequence, the maximum value for $|\boldsymbol{w}| = w_3$, which is reached in the center of the tube, is:

$$|\boldsymbol{w}|_{r_l=0} = \frac{r_c^2}{4} \approx 1.22 \cdot 10^{-3}, \tag{2.36}$$

and its average reads:

$$K_r = K_c|_{\omega=0} = \langle w_3\rangle_c\,|_{\omega=0} = \frac{1}{|\Omega_c|}\int_0^{l_c} \mathrm{d}z \int_0^{2\pi} \mathrm{d}\theta \int_0^{r_c} \frac{r_c^2 - r_l^2}{4} r_l\,\mathrm{d}r_l = \frac{\pi l_c r_c^4}{8|\Omega_c|} = 2.13 \cdot 10^{-4}, \tag{2.37}$$

where the values reported in Tables 2.1 and 2.2 have been used. In the non-tortuous case, the solution then agrees with the analytical solution (2.35), up to a small deviation in the central region of Ω_c, where branches cross each other. [1]

The solution for the tortuous geometric configurations deviates from a merely parabolic profile, as far as the frequency ω increases. Nevertheless, the cell average of the (non-zero) transversal components remain negligible with respect to K_c (see Table 2.2), so that the condition (2.24) for

[1] In this region, the solution in the branch directed along z is not subject to homogeneous Dirichlet boundary conditions, rather, it smoothly approaches zero to match that in the orthogonal branches and, as a result, we obtain a slightly higher value for the maximum $|\boldsymbol{w}|_{r_l=0} \approx 1.26 \cdot 10^{-3}$ and $K_r = 2.2 \cdot 10^{-4}$. Furthermore, the components w_1 and w_2 reduce to zero up to numerical errors, namely $|w_1/w_3| \ll 1$ and $|w_2/w_3| \ll 1$ everywhere in Ω_c.

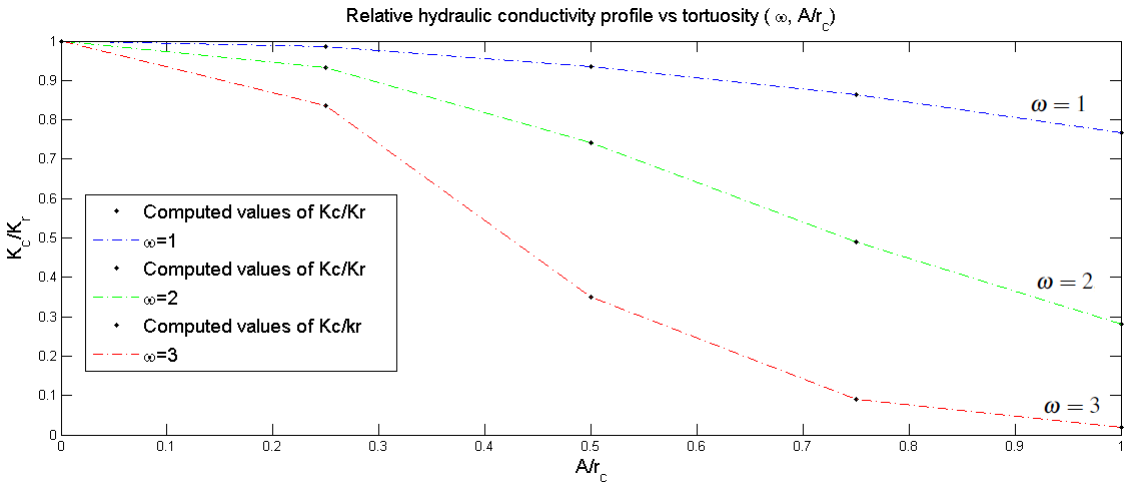

Figure 2.5: *Relative hydraulic conductivity profile as a function of relative amplitude. The black dots represent the results of the numerical simulations, whereas dashed lines emphasize the difference in the non-linear drop of the hydraulic conductivity at increasing frequency.*

macroscopic isotropy is satisfied, as

$$K_{ij} \ll K_c, \quad \forall\, i \neq j, \quad i, j = 1, 2, 3. \tag{2.38}$$

The normalized K_c versus A/r_c exhibits a non-linear monotonic decrease which is more marked at higher frequency ω (see Figure 2.5). The hydraulic conductivity K_c dramatically reduced at large tortuosity and an up to 45-fold K_c drop is observed.

Comparison with the perturbation theory

The observed non-linearity of the hydraulic conductivity versus tortuosity reflects that of Stokes' flow in wavy channels, where the solution can significantly deviate from the parabolic one. Nevertheless, under a number of simplifying assumptions, analytical solutions can be found by perturbative methods. Kitanidis and Dykaar (1997); Di Federico et al. (2002) developed an analytic method to determine the solution of the Stokes' problem for a 2D, axis symmmetric, periodic, waving channel, in terms of a power series expansion, under the assumption that the width is much smaller than the wavelength. They report a non-linear decrease of the flow discharge with respect to the channel amplitude at leading order whereas, to track variations with respect to the frequency, higher order terms in their asymptotic expansion are to be taken into account. A 3D generalization of their theory can be found in Malevich et al. (2006), where perturbation analysis is used to compute the waving channels permeability via power series in terms of a small asymptotic parameter, which measures the deviation of the channel with respect to a straight reference configuration. Also in this work, the authors exploit axial symmetry of the channel (which is not assumed here) and their procedure is only valid up to a critical value for their asymptotic parameter. Their results

show a non-linear decrease of the channel permeability as far as its perturbation with respect to the symmetry axis increases.

The most widely exploited assumption to derive the flow field in slowly vaving channels rely on the so called *lubrication* approximation (see e.g. Batchelor (2000); Malevich et al. (2006)). In such a framework, the flow is supposed to be parabolic as long as the characteristic *length* of the channel (which is its wavelength for periodic wavy ones) is much larger than the channel height (radius) and relative variations with respect a straight reference configuration are small. For example, in Shipley (2008), curvilinear coordinates are exploited to compute the permeability of the capillary compartment; when specialized to the isotropic and non-slippery case the capillary hydraulic conductivity reads:

$$K_c = \frac{\pi r_c^4 l_c^2}{8|\Omega_c|\gamma}, \tag{2.39}$$

where γ denotes the branch center line length (see Figure 2.2). In our case, the total branch center line length is $\gamma = 2|f| + h$, where $|f|$ denotes the one-sided branch center line length and h the linking cylinder height. Therefore, in our reference configuration, $\gamma = l_c$ and (2.39) matches the analytic profile provided in (2.37). Notice that, for a tortuous geometrical setting, $\gamma > l_c$ and hence (2.39) predicts a permeability drop of the type:

$$K_c \propto \frac{1}{\gamma}. \tag{2.40}$$

In the high frequency regime, the lubrication approximation does not apply and the solution exhibits large deviations from the parabolic profile (see Figure 2.4). However, when $\omega = 1$, the perturbation of the geometry with respect to the reference configuration is small enough that the numerical results agree with (2.40) (see Figure 2.6).

Even the capillary network formed by the cell portions Ω_c can be viewed as a porous medium (with unit porosity), with hydraulic conductivity given by the Kozeny-Carman formula, see Kozeny (1927); Carman (1937). Some manipulations are needed to exploit this analysis, for example Heijs and Lowe (1995) stipulate that

$$K_c = \frac{1}{c_0 S_c^2}; \quad S_c = \frac{S}{|\Omega_c|}, \tag{2.41}$$

where c_0 is the Kozeny constant, which increases with the geometrical tortuosity. Matyka et al. (2008) show that the Kozeny constant exhibits a quadratic dependence on the representative path length, which is in turn related to the geometrical tortuosity. We have numerically computed the Kozeny constant for several prototype geometries (see Table 2.2). Whenever deviations from the reference configurations are small (i.e $\omega = 1$), a relationship of the type (2.41) is sufficient to

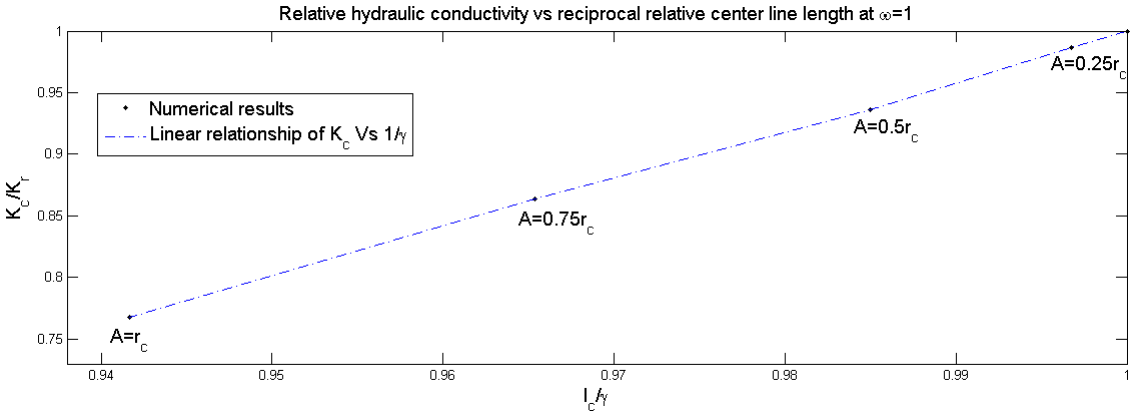

Figure 2.6: *Numerical results showing the linear relationship between the hydraulic conductivity and the reciprocal branch center line length, in qualitative agreement with Shipley (2008).*

describe the dependence of the capillary hydraulic conductivity on the geometrical properties of the network. Nevertheless, as the tortuosity increases, a quadratic decrease of K_c with respect to the surface-to-volume ratio $S/|\Omega_c|$ is not anymore observed, as a dramatic increase of c_0, which is not constant any longer, is observed.

2.3.3 The interstitial cell problem

We performed numerical simulations to compute P^t and hence capture variations of the interstitial conductivity E (in particular E_t) with respect to tortuosity, in the complementary geometry given by $\Omega_t = \Omega \setminus \Omega_c$ (see Figure 2.3). The numerical solution of the problem (2.29-2.30) is now weakly affected by tortuosity. According to Table 2.3, accounting for definition (2.9) and identifications (2.33), we deduce:

$$E_{ij} \ll E_t \quad \forall\, i \neq j, \quad i, j = 1, 2, 3, \tag{2.42}$$

that is, macroscopic isotropy condition (2.25) is satisfied. We further notice that, even though integral average variations of P^t along $\boldsymbol{e}_3$ are more relevant than those in the orthogonal directions, they are however much smaller than 1, such that, in the explored regimes, E slightly deviates from the identity tensor. This can be explained observing that spatial variations of P^t (relevant in the direction $\boldsymbol{e}_3$ of the Neumann datum only) are significant only in a narrow layer around the vessels (see Figure 2.7). Since

$$E_t = 1 - \left\langle \frac{\partial P^t}{\partial y_3} \right\rangle_t \tag{2.43}$$

and average is performed over Ω_t, with $|\Omega| \approx |\Omega_t|$ (see Table 2.1 and 2.2), we get

$$\left\langle \frac{\partial P^t}{\partial y_3} \right\rangle_t = \frac{1}{|\Omega_t|} \int_{\Omega_t} \frac{\partial P_3^t}{\partial y_3}\, \mathrm{d}\boldsymbol{y} \ \ll 1 \rightarrow E_t \approx 1. \tag{2.44}$$

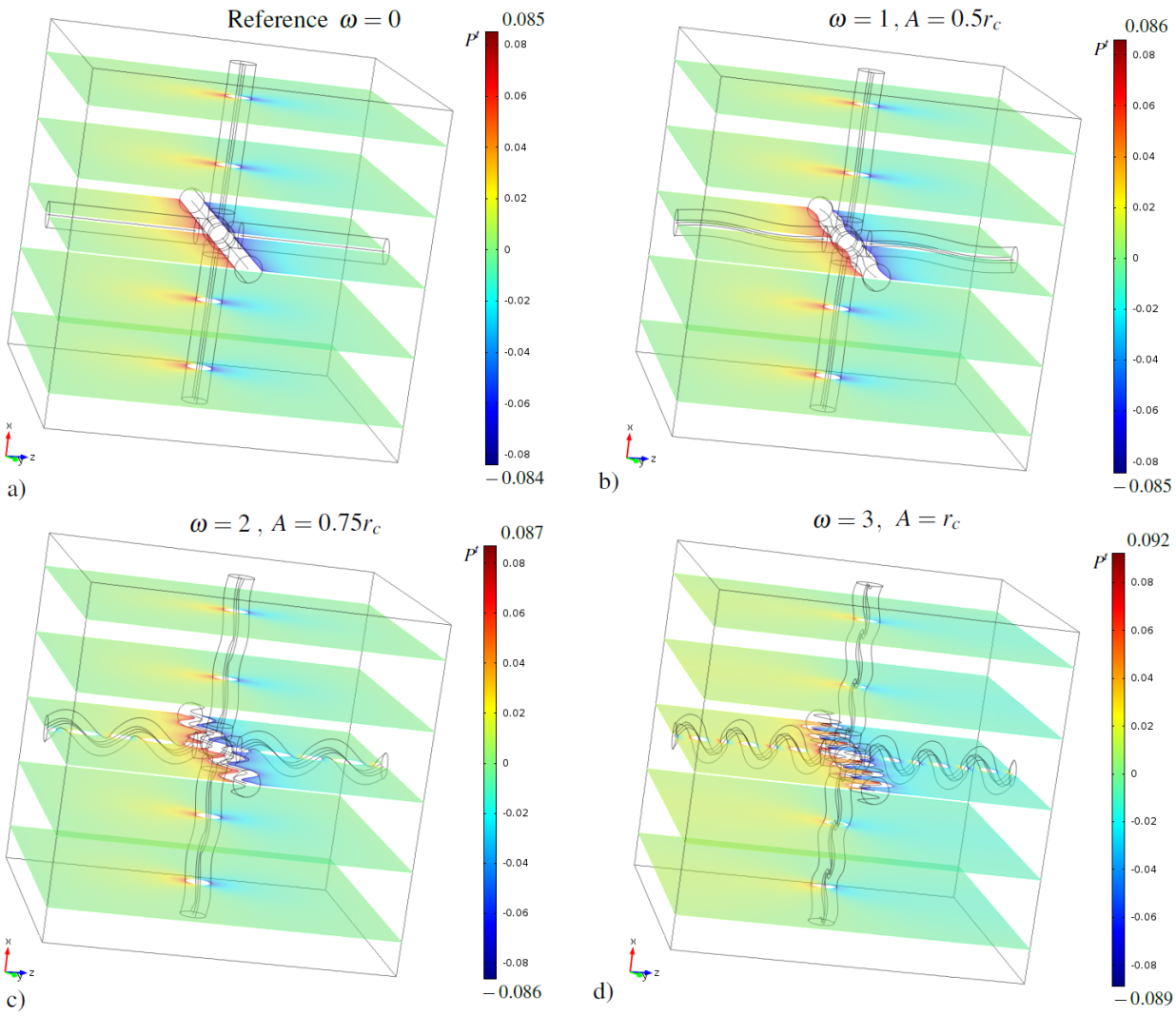

Figure 2.7: *Examples of numerical results for P^t, where four representative geometries (complementary to those shown in Figure 2.4) are chosen. The solution gradients only weakly contributes to the effective hydraulic conductivity* E *and no significant changes are observed by varying the geometrical tortuosity, see Table 2.3.*

ω	A	$E_t\left(1-\left\langle\frac{\partial P^t}{\partial y_3}\right\rangle_t\right)$	$\left\langle\frac{\partial P^t}{\partial y_1}\right\rangle_t$	$\left\langle\frac{\partial P^t}{\partial y_2}\right\rangle_t$
0	0	0.991	$1.23\cdot10^{-8}$	$-6.55\cdot10^{-8}$
1	$0.25r_c$	0.991	$-2.25\cdot10^{-5}$	$-7.35\cdot10^{-5}$
1	$0.5r_c$	0.991	$-1.40\cdot10^{-5}$	$-1.49\cdot10^{-5}$
1	$0.75r_c$	0.991	$-1.98\cdot10^{-5}$	$-2.02\cdot10^{-5}$
1	r_c	0.991	$-2.76\cdot10^{-5}$	$-2.71\cdot10^{-5}$
2	$0.25r_c$	0.991	$-6.36\cdot10^{-6}$	$-5.83\cdot10^{-6}$
2	$0.5r_c$	0.991	$-1.63\cdot10^{-5}$	$-1.50\cdot10^{-5}$
2	$0.75r_c$	0.992	$-3.30\cdot10^{-5}$	$-3.09\cdot10^{-5}$
2	r_c	0.992	$-5.46\cdot10^{-5}$	$-5.23\cdot10^{-5}$
3	$0.25r_c$	0.991	$-1.00\cdot10^{-5}$	$-6.89\cdot10^{-6}$
3	$0.5r_c$	0.992	$-5.09\cdot10^{-5}$	$-5.24\cdot10^{-6}$
3	$0.75r_c$	0.992	$-5.48\cdot10^{-5}$	$-3.47\cdot10^{-5}$
3	r_c	0.992	$1.00\cdot10^{-5}$	$1.00\cdot10^{-5}$

Table 2.3: *Computational results for the non-dimensional conductivity tensor* E. $E_t \approx 0.99$ *for every tortuosity regime explored. Non diagonal values of* E *are negligible with respect to* E_t.

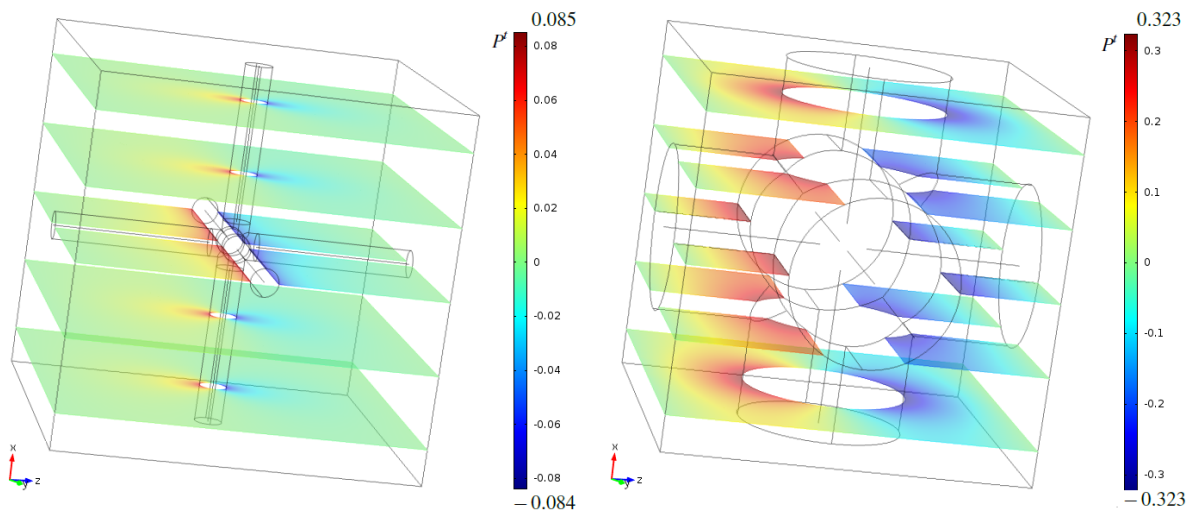

Figure 2.8: *Color map of* P^t *for two non-tortuous geometries, with different* $\frac{|\Omega_t|}{|\Omega|}$ *. On the left hand side, the reference geometry (which corresponds to the reference capillary compartment radius* r_c*) is characterized by small and localized spatial variation of the solution* $\frac{\partial P^t}{\partial y_3}$*. On the right hand side, the solution for* $\frac{|\Omega_t|}{|\Omega|} \approx 0.64$ *(which corresponds to a* $6r_c$ *capillary compartment radius) is shown. In the latter case, the interstitial volume fraction decreases and the spatial gradient of* P^t *increases, thus leading to a corresponding decrease in* E_t *(see definition* (2.9) *and Figure 2.9).*

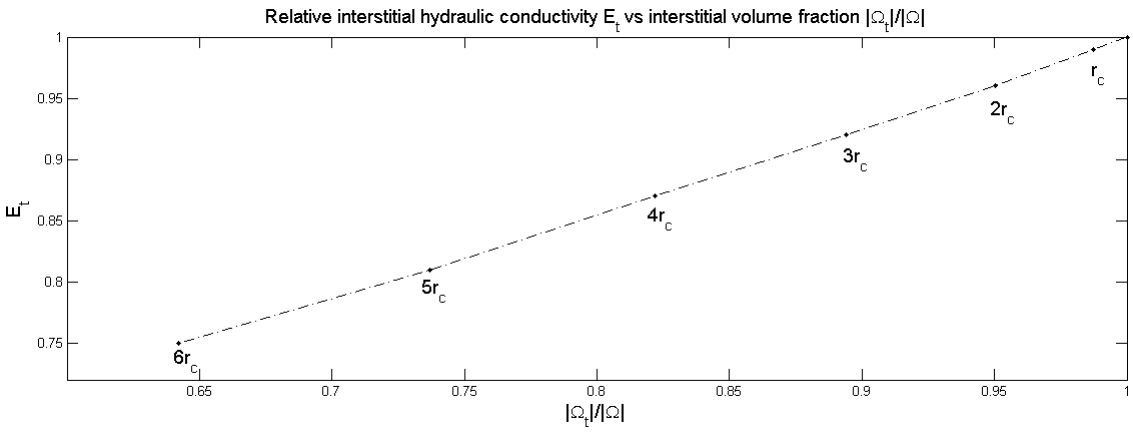

Figure 2.9: *A linear relationship between E_t and the interstitial volume fraction $\frac{|\Omega_t|}{|\Omega|}$. Black dots represent the numerical results which correspond to the various interstitial configurations obtained by varying the radius of each complementary capillary compartment branch from r_c to $6r_c$.*

The geometric role of E_t can be pointed out by decreasing the interstitial volume $|\Omega_t|$. We performed numerical tests for sample interstitial geometries Ω_t, complementary to increased volume and non tortuous capillary compartments Ω_c (see example Figure 2.8). We obtain an almost linear relationship for E_t versus interstitial volume fraction (see Figure 2.9). In particular, according to (2.6) and (2.25) the non-dimensional interstitial velocity is given by:

$$\boldsymbol{u}_t = -\bar{\kappa} E_t \nabla_{\boldsymbol{x}} p_t, \tag{2.45}$$

i.e. the Darcy's law applies with conductivity given by $\bar{\kappa} E_t$. The non-dimensional conductivity $\bar{\kappa}$ is directly related to the physiological value κ, which is obtained via experimental measurements over the whole tumor mass (i.e no distinction between the interstitial and capillary compartment is taken into account). On the basis of the numerical tests (see Figure 2.9), E_t can be viewed as a correction factor ($0 < E_t < 1$), which, according to the actual interstitial volume portion perfused by the fluid, reduces the average measured conductivity value.

In the following section, we present and discuss the analytical solution of the isotropic fluid transport problem (2.3-2.6). Since we focus mostly on the consequences of increased geometrical tortuosity, we exploit the numerical values reported in Table 2.1, 2.2 and 2.3 in the analysis that follows.

2.4 The macroscopic model

The macroscale differential problem (2.3-2.6), under isotropic conditions (2.24-2.25), reads:

$$\begin{cases} \nabla^2_{\boldsymbol{x}} p_c = M_c(p_c - p_t) & \text{in } \Omega_H & (2.46) \\ \nabla^2_{\boldsymbol{x}} p_t = -M_t(p_c - p_t) & \text{in } \Omega_H & (2.47) \\ \boldsymbol{u}_c = -K_c \nabla_{\boldsymbol{x}} p_c & & (2.48) \\ \boldsymbol{u}_t = -K_t \nabla_{\boldsymbol{x}} p_t, & & (2.49) \end{cases}$$

where

$$K_t = E_t \bar{\kappa}, \quad M_c = \frac{\bar{L}_p S}{K_c |\Omega_c|}, \quad M_t = \frac{\bar{L}_p S}{K_t |\Omega_t|}. \tag{2.50}$$

We consider a spherical macroscale domain Ω_H with radius R representing the tumor. In particular, we enforce radial symmetry: all the fields depend on the radial coordinate r only and the problem (2.46-2.47) rewrites

$$\begin{cases} \frac{1}{r}\frac{d^2}{dr^2}(r p_c) = M_c(p_c - p_t) & 0 < r < R & (2.51) \\ \frac{1}{r}\frac{d^2}{dr^2}(r p_t) = -M_t(p_c - p_t) & 0 < r < R & (2.52) \\ \frac{dp_c}{dr}|_{r=0} = \frac{dp_t}{dr}|_{r=0} = 0 & & (2.53) \\ p_c|_{r=R} = \bar{p} > 0, \quad p_t|_{r=R} = 0. & & (2.54) \end{cases}$$

The tumor is supposed to be isolated (Jain and Baxter, 1988; Jain et al., 2007). Hence, we prescribe the pressures on the tumor boundary (2.54), while symmetry in $r = 0$ implies null flux in the tumor center, corresponding to homogeneous Neumann boundary conditions (2.53). The choice (2.54) accounts for experimental observations (Boucher et al., 1990): the interstial fluid pressure is constant and smaller than the microvasculature pressure on the tumor surface. The flow driving force is the pressure difference $p_c - p_t$ and p_t can be set to zero on the tumor surface without loss of generality (Jain and Baxter, 1988; Jain et al., 2007). The radial components of the Darcy's velocities $u_c(r)$ and $u_t(r)$ are

$$u_c(r) = -K_c \frac{dp_c}{dr}, \quad u_t(r) = -K_t \frac{dp_t}{dr}. \tag{2.55}$$

The solution of the problem (2.51-2.54) can be obtained via direct integration (see A):

$$\hat{p}_c = \frac{1}{M_c + M_t}\left(M_t + \frac{M_c \sinh(\alpha \hat{r})}{\hat{r}\sinh(\alpha)}\right), \tag{2.56}$$

$$\hat{p}_t = \frac{M_t}{M_c + M_t}\left(1 - \frac{\sinh(\alpha \hat{r})}{\hat{r}\sinh(\alpha)}\right), \tag{2.57}$$

where $\hat{p}_c = p_c/\bar{p}$, $\hat{p}_t = p_t/\bar{p}$ are the relative capillary and interstitial pressure, respectively and $\hat{r} = r/R$ is the relative radial position, while

$$\alpha = R\sqrt{(M_c + M_t)}. \tag{2.58}$$

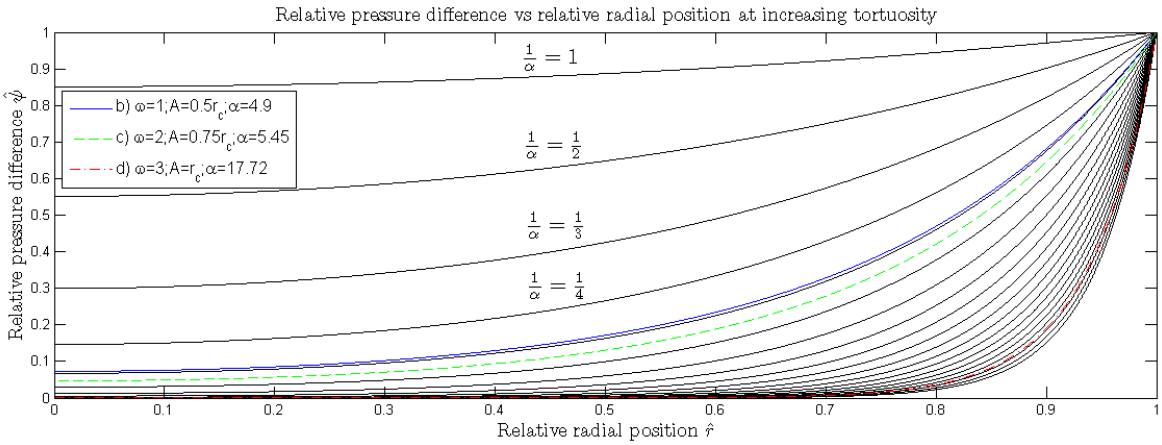

Figure 2.10: *The macroscale pressure difference versus relative radial position for $1 < \alpha < 20$ is shown. Key particular cases at increased tortuosity are displayed. The solution exhibits a sharp non-linear decreasing profile at increased tortuosity (the latter implying an increase in α), such that, for high geometrical complexity, no pressure difference and hence no convection of blood is observable in the tumor inner regions.*

The capillary and interstitial velocities can be written in terms of $\hat{u}_c = \dfrac{u_c R}{K_r \bar{p}}$ and $\hat{u}_t = \dfrac{u_t R}{K_t \bar{p}}$ by direct derivation:

$$\hat{u}_c = -\frac{K_c M_c}{K_r(M_c + M_t)} \left(\frac{\alpha \hat{r} \cosh(\alpha \hat{r}) - \sinh(\alpha \hat{r})}{\sinh(\alpha) \hat{r}^2} \right), \tag{2.59}$$

$$\hat{u}_t = \frac{M_t}{M_c + M_t} \left(\frac{\alpha \hat{r} \cosh(\alpha \hat{r}) - \sinh(\alpha \hat{r})}{\sinh(\alpha) \hat{r}^2} \right). \tag{2.60}$$

Finally, we define the relative pressure difference between the capillary and interstitial pressure as

$$\hat{\psi} = \hat{p}_c - \hat{p}_t = \frac{\sinh(\alpha \hat{r})}{\hat{r} \sinh(\alpha)}. \tag{2.61}$$

2.4.1 The impact of tortuosity on tumor blood convection

The relative pressure difference is plotted versus the relative radial position (see Figure 2.10). The relative pressure jump $\hat{\psi}$ is the driving force of the blood flow (see Figure 2.11 and 2.12) and exponentially decays in $1/\alpha$, where

$$\alpha = R \sqrt{\frac{\bar{L}_p S}{|\Omega_c| K_c} + \frac{\bar{L}_p S}{|\Omega_t| K_t}}. \tag{2.62}$$

As far as the tortuosity of the microvasculature grows, the surface to capillary volume ratio $S/|\Omega_c|$ increases, while the hydraulic conductivity K_c decreases (see Table 2.2), both contributing to an increase in α. In fact, for low tortuosity (i.e in the $\alpha < 5$ regime, see Figure 2.10), a non-zero pressure difference is observed even in the tumor center whereas, for higher values of α blood and

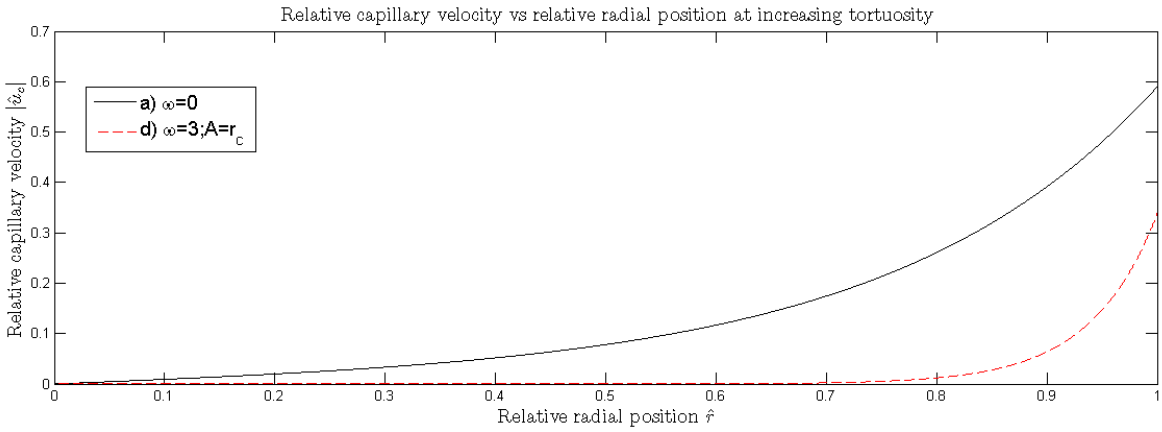

Figure 2.11: *The relative capillary velocity, which is inward directed, for the reference and most tortuous configuration. The blood flow, which is driven by the pressure difference $\hat{\psi}$, is impaired by tortuosity and rapidly approaches zero.(In the displayed case, the capillary flow reduces approximately to zero at $\hat{r} \simeq 0.7$).*

possible injected anti-cancer drugs cannot permeate the whole tumor mass. For example, in the most tortuous regime that we explore, no blood flow can permeate the tumor mass for $\hat{r} \simeq 0.7$.

The main feature of our multiscale formulation is to account for the hydraulic and geometric properties of the tissue interstitium and capillary compartment separately, such that, under fixed physiological conditions (see Table 2.1), we can quantitatively evaluate the role of the geometrical tortuosity in tumor blood convection. Even though we performe the present analysis accounting for a specific microscale configuration, we argue that our results are robust with respect to different geometric settings, provided that conditions (2.24-2.25) are met. Given the physiological setting encoded in α (the tumor radius R, vascular hydraulic permeability L_p and tumor tissue conductivity κ), we thus predict a strong dependence of the tumor blood convection with respect to tortuosity, such that geometrical regularization of the microvasculature network can improve blood flow within the tumor. Next, we compare the results of our model with the relevant literature and perform an analysis of the blood flow determinants which are captured by these different formulations.

2.5 Comparison with Jain and Baxter (1988)

The model for the fluid flow in a spherical solid tumor developed by Jain and Baxter (1988) and experimentally validated by Boucher et al. (1990) is based on a single compartment for the interstitial flow, which exchange fluid through the blood vessels walls. In particular, the interstitial velocity $\boldsymbol{u}_I$ is given by the isotropic Darcy's law:

$$\boldsymbol{u}_I = -\kappa \nabla p_I, \tag{2.63}$$

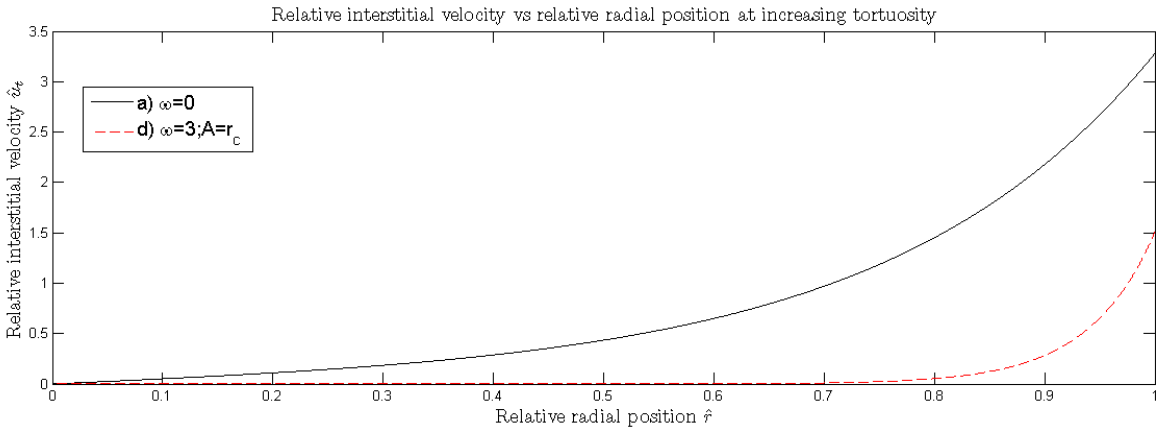

Figure 2.12: *The relative interstitial velocity, which is outward directed, for the reference and most tortuous configuration. The blood flow, which is driven by the pressure difference $\hat{\psi}$, is impaired by tortuosity and rapidly approaches zero.(In the displayed case, the interstitial flow reduces approximately to zero at $\hat{r} \simeq 0.7$).*

where p_I is the interstitial pressure. The fluid leakage from the blood vessels is an effective source for the interstitial flow:

$$\nabla \cdot \boldsymbol{u}_I = \frac{J_V}{\mathrm{V}}, \tag{2.64}$$

where V is the tumor volume and J_V is the vessels blood flux:

$$J_V = L_p \mathrm{S} \left(p_V - p_I\right), \tag{2.65}$$

p_V being the constant microvascular pressure and S the exchange surface. The relationship (2.65) rules out the contribution due to the osmotic pressure driven by the plasma proteins difference in concentration, which is negligible in tumors (Jain et al., 2007). Thus, substituting (2.63) and (2.65) into (2.64), they obtain, in dimensional form:

$$\nabla^2 p_I = -\frac{L_p \mathrm{S}}{\kappa \mathrm{V}} \left(p_V - p_I\right). \tag{2.66}$$

When assuming spherical symmetry with null interstitial pressure on the tumor boundary, the analytical solution of the model (2.66) for the relative interstitial pressure p_I/p_V in terms of the radial coordinate $\hat{r}$ is:

$$\frac{p_I}{p_V} = 1 - \frac{\sinh(\alpha_J \hat{r})}{\hat{r}\sinh(\alpha_J)}, \tag{2.67}$$

where

$$\alpha_J = \mathrm{R}\sqrt{\frac{L_p \mathrm{S}}{\kappa \mathrm{V}}}. \tag{2.68}$$

Jain and Baxter (1988) do not address the fluid dynamics in the vessels. Nevertheless, a comparison with the model proposed in this paper in terms of relative pressure difference is possible, in fact:

$$\frac{p_V - p_I}{p_V} = \frac{\sinh(\alpha_J \hat{r})}{\hat{r}\sinh(\alpha_J)}. \tag{2.69}$$

The pressure drop in (2.61) and (2.69) have the same functional form; however, the non dimensional coefficients α and α_J are different, as in this work we explicitly account for variations in the capillary pressure and for the role of the specific geometric and hydraulic vessels properties, such as their volume and hydraulic conductivity. In particular, the model by Jain and Baxter (1988) can be recovered when assuming that the capillary pressure is constant and

$$|\Omega_c|K_c \gg |\Omega_t|K_t, \quad |\Omega_t| \approx |\Omega| \to E_t \approx 1, \tag{2.70}$$

i.e. when accounting for a geometrically regular, low density, vascular network. For example, according to Tables 2.1, 2.2 and 2.3, we obtain $|\Omega_c|K_c \approx 5|\Omega_t|K_t$ and $|\Omega_t| \approx |\Omega|$ with $E_t \approx 1$ for our reference configuration. Whenever the conditions (2.70) apply, we obtain

$$\alpha \approx R\sqrt{\frac{\bar{L}_p S}{\bar{\kappa}|\Omega|}} = R\sqrt{\frac{L_p S L^2}{\kappa d|\Omega|}}, \tag{2.71}$$

where definitions (2.7) are exploited. The dimensional exchange surface to volume ratio and tumor radius read:

$$\frac{\mathrm{S}}{\mathrm{V}} = \frac{S}{d|\Omega|}, \quad \mathrm{R} = RL, \tag{2.72}$$

respectively, where R is the non-dimensional macroscale tumor radius, while the non-dimensional surface-to-volume ratio $S/|\Omega|$ is calculated over the microscale periodic cell. Thus, substituting (2.72) into (2.71) yields

$$\alpha \approx \mathrm{R}\sqrt{\frac{L_p \mathrm{S}}{\kappa \mathrm{V}}} = \alpha_J, \tag{2.73}$$

in agreement with relationship (2.68). The mathematical model by Jain and Baxter (1988) thus coincides with the homogenized model by Shipley and Chapman (2010) under the specific assumptions (2.70).

The main difference between the two models is represented by the additional information we are able to capture about the geometric and hydraulic properties of the microvascular network, as well as the spatial dependence of the capillary flow in the vessels. As the same functional form for the problem solution is obtained (see equations (2.61) and (2.69)) in both approaches, then an experimental datum fit by a relationship of the type (2.69) necessarily involves a dependence on the vascular microstructure, although not explicitly encoded in their non-dimensional number α_J.

We conclude the section discussing the role of the tumor blood convection determinants captured by the two models.

- The *Tumor growth stage*, identified by the tumor radius R, can significantly affect fluid convection in tumors. Normalization therapies able to reduce the tumor radius can therefore strongly improve transport of blood, and, as a consequence, anti-cancer drugs within the tumor mass, thus possibly increasing medical therapies effectiveness. The tumor radius has exactly the same impact on the tumor fluid dynamics in both models.

- The *Tumor hydraulic conductivity* κ regulates the amount of fluid that can actually permeate the tissue, hence, as expected, an increase in the tumor conductivity yields a decrease in α, which in turn drives a convection improvement. It plays a similar quantitative role in both models, as we did not observe a significant dependence on tortuosity (see Table 2.3). Nevertheless, we remark that the hydraulic conductivity values are obtained by experimental measurements (see e.g. Boucher et al. (1998)) and they intrinsically refer to the whole tumor tissue. Our K_t (see definitions (2.50)) corresponds, instead, to the interstitial conductivity only and it is in general a fraction of the average tumor conductivity value that can be experimentally measured. According to Jain et al. (2007), it is an open issue whether normalization therapies can play a role in increasing the tumor hydraulic conductivity; recently developed techniques do not highlight a significant increase of the tumor hydraulic conductivity, which is instead proved to strongly depend on the interstitial matrix constituents and hydration (Swabb et al., 1974; Jain, 1987b).

- The *vascular hydraulic permeability* L_p is the key determinant of the blood leakage from the capillary vessels to the tissue. It provides an averaged information on the fenestrations of the membrane, which, especially in tumors, exhibits openings and defects among the endothelial cells (Hashizume, 2000). Our model leads to the same, apparently counterintuitive, conclusion that is found in Jain et al. (2007), i.e. an increase in the vascular permeability does not improve blood convection within the tumor, because a more permeable membrane rapidly damps the pressure gradient across the vessels walls, which is the driving force of the blood convection process. The vascular hydraulic permeability is found to be up to two orders of magnitude greater in tumors than in healthy vascularized tissue and, according to Jain et al. (2007), vascular normalization therapies should significantly lower it.

- *The exchange surface-to-volume ratios*, here denoted by $S/|\Omega_t|$ and $S/|\Omega_c|$, play an impor-

ω	A	α
0	0	4.86
1	$0.25r_c$	4.87
1	$0.5r_c$	4.9
1	$0.75r_c$	4.96
1	r_c	5.02
2	$0.25r_c$	4.90
2	$0.5r_c$	5.05
2	$0.75r_c$	5.45
2	r_c	6.25
3	$0.25r_c$	4.97
3	$0.5r_c$	5.89
3	$0.75r_c$	9.05
3	r_c	17.72

Table 2.4: *Computed values of α for thirteen sample microvasculature geometries. At increasing tortuosity, a typical tumor pressure difference profile is obtained, even accounting for a normalized value of the vascular hydraulic permability L_p.*

tant role in driving the fluid transport process. In the double compartment model we started from, we are able to track both the interstitial and the capillary surface-to-volume ratios. As expected, for fixed interstitial and capillary volume, a greater vessels exchange surface leads to an increase in leakage, thus producing the same net effect of an increase in the vascular hydraulic permeability L_p. In Jain and Baxter (1988), the global surface-to-volume ratio plays a similar role, even though it refers to the volume of the whole tumor, instead of the interstitial portion only. According to Jain et al. (2007), vascular normalization therapies should decrease the global surface-to-volume ratio.

- *The capillary hydraulic conductivity*, here denoted by K_c, accounts for the hydraulic properties of the capillary network. It is a main feature captured by the homogenized model by Shipley and Chapman (2010) and neglected in the previous literature. The capillary hydraulic conductivity is strongly affected by the geometrical complexity of the network (see Figure 2.5). A decrease in K_c corresponds to an increase in α (see Table 2.4), resulting in a compromised blood flow within the tissue. Thus, geometric regularization of the vascular network can improve both directly (through the exchange surface-to-volume ratios) and indirectly (through K_c, see Table 2.2) the fluid transport process in the malignant mass.

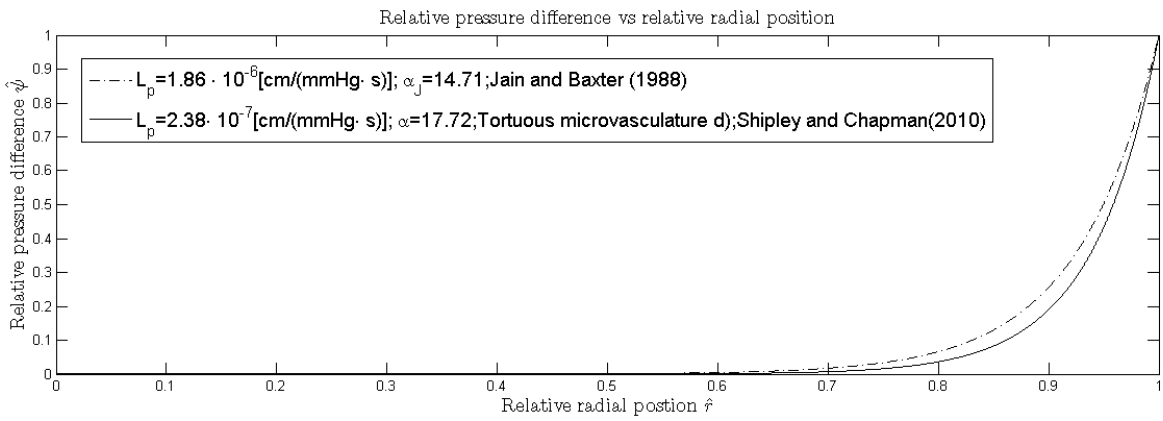

Figure 2.13: *A comparison between the models by Jain and Baxter (1988) (displayed for a tipical tumor value for L_p) and Shipley and Chapman (2010) (displayed for a typical normalized value for L_p, at increasing tortuosity). The characteristic tumor pressure difference, which is fit approximately in the range $7 < \alpha < 17$ (Jain et al., 2007), can be the result of both increased vascular hydraulic permeability L_p and of increased microvascular tortuosity*

2.6 Concluding remarks

In this work we perform a qualitative and quantitative analysis of the microvascular tortuosity impact on blood convection in solid isolated tumors. We start from the double Darcy homogenized model by Shipley and Chapman (2010), to describe the tissue scale fluid dynamics of both the interstitial and capillary compartments. Although this model neglects important features of the blood flow in the capillaries, such as non-Newtonian effects (see e.g. Fahareus and Lindqvist (1931), Pries et al. (1990)), structural adaptation, remodeling of the network (see for example Pries et al. (1998); Owen et al. (2008)) and macroscopic changes of the microstructure (Penta et al., 2013), it represents a robust starting point to account for the net effect of the tortuosity on blood transport phenomena, as it allows to track the interstitial and capillary compartment separately, as well as their hydraulic properties and their dependence on the microstructure. In this work, the geometric information encoded in the hydraulic conductivities of the model is obtained via 3D numerical simulations on a single representative microscale cell. Then, the computed values are injected in the tissue scale homogenized model, which we solve analytically in the case of macroscopic isotropy. As a result, we predict a dramatically impaired blood convection for increasing tortuosity, which can be properly quantified as a function of the specific microvasculature geometry (see Table 2.4).

According to Jain et al. (2007), vascular normalization therapies regularize the exchange surface of the vascular network. However, our analysis suggests that modifications in the microvascular geometry strongly affect the blood flow in the capillaries and hence the hydraulic properties of the vessels compartment. In Figure 2.13 we show a comparison between the Jain and Baxter (1988) and

Shipley and Chapman (2010) relative pressure difference profile, obtained using different values for the vascular hydraulic permeability. Curves are plotted using a L_p value associated to tumor vessels (Jain et al., 2007) for Jain and Baxter (1988), whereas we use a lower L_p value (corresponding to the range for normalized microvasculature, see Table 2.1) for Shipley and Chapman (2010), using the more tortuous configuration displayed in Figure 2.4d). As L_p is experimentally evaluated as the ratio between the average blood flux and pressure difference (both assumed constant, see e.g. Sevick and Jain (1991)), we argue that its decrease observed after normalization therapies by means of the single compartment model of Jain and Baxter (1988) actually encloses an increase in the capillary hydraulic conductivity. In other words, the same profile for the convection of blood in the tumor is obtained either accounting for a higher value of L_p, neglecting an explicit contribution of the microvascular properties, or accounting for a normalized L_p, accounting for a highly tortuous microvasculature.

Our analysis suggests that recent normalization techniques (Jain et al., 2007) affect both these crucial blood flow determinants. The observed decrease of the surface-to-volume ratio does affect the fluid-dynamics in the blood capillaries, whereas a reduction of the vessel wall openings and defects lowers L_p. We suggest that novel normalization therapies that rely on blood convection improvement via vascular network regularization, should focus both on structural (i.e affecting L_p) and geometrical (i.e affecting K_c, $S/|\Omega_c|$, $S/|\Omega_t|$) vessel properties.

Finally, although the aim of this work is to elucidate the connection between blood convection and vascular struscture, the next crucial step is to identify a realistic representative microscale network starting from medical images. Then, model predictions would enable clinical validation and highlight additional structure-specific blood flow features, related to possible microvascular anisotropy and heterogeneities.

CHAPTER 3

Effective governing equations for poroelastic growing media

3.1 Introduction

The theory of poroelasticity concerns the mechanics of porous elastic solids with fluid-filled pores. The applications and motivations for this theory are far-reaching, and include the seepage of liquid waste disposed of underground, oil and gas recovery, soil consolidation and glaciers dynamics, as well as transport, mass exchange and solid stress in biological tissues. Whereas poroelasticity concerns fluid-solid interactions in two-phase materials, it lies within the broader field of mixture theory, which includes fluid and chemical transport in multiphase systems.

The literature in poroelasticity develops according to two main approaches; volume-averaging and homogenisation (the two are discussed in detail and compared in the review paper Davit et al. (2013)). Most authors state *ab initio* the mass, momentum and energy balance equations for the individual phases on the basis of their “in bulk" mechanical behavior and utilize dissipation inequalities to restrict the possible constitutive equations for the components *in the mixture* (see Bowen (1980) and Bowen (1982)). While this approach allows for generality in the number of components

and their mechanical nature, including finite elastic strains, any information on the microstructure of the material is suppressed by an implicit averaging procedure; as a consequence, effective coefficients that appear in the equations (for example, the fluid permeability) are at most characterized by their sign and are to be fitted by macroscopic experiments only.

The alternative homogenisation method exploits information on the geometry at the microscale by a multiscale expansion of the fields. This approach yields macroscopic equations with parameters that depend explicitly on the microscale geometry and physics; these parameters are obtained by averaging suitable microscale cell problems (as for example in Sanchez-Palencia (1980), Sanchez-Palencia (1983), Holmes (1995) and Mei and Vernescu (2010)). The homogenisation technique is therefore powerful in retaining microscopic information; the drawback is that periodicity of the microstructure and linearity in the constitutive equations must be assumed. Moreover, the algebraic complexity of the method has reduced *de facto* its application to physical systems.

From the point of view of continuum mechanics, a challenging peculiarity of soft biological tissues is their ability to grow and remodel, a special characteristic of living matter that poses a number of intriguing mathematical questions: how to account for the resulting residual stress, which are the driving forces of growth, which are the corresponding regulatory mechanisms and the inner energy balance, see, e.g. Rodriguez et al. (1994),Taber (1995) and Ambrosi and Guana (2007). This kind of questions has inspired a substantial body of literature in mathematical methods that, starting from one–component continuum mechanics, move towards the inclusion of multicomponent and microscale information in the model Ambrosi et al. (2010).

On the basis of the considerations above, it is not surprising that the specific issue of poroelastic materials that exchange mass has been mainly addressed in terms of mixtures, both for inert (see for example Whitaker (1973), Gray (1975) and Hutter (1983)) and living matter (as in Cowin (2004) and Ateshian (2007)). In the current study we seek to extend the existing poroelastic literature by considering mass exchange between elastic and fluid phases using a multiscale approach[1]. Although poroelasticity exhibits a wide range of applicability and growth is a crucial issue to address in a number of fields, the chief motivation for this work is biological. The growth and remodelling of living tissues is driven by chemical stimuli as well as the mechanical environment (alongside genetic cues) and the development of mathematical models that couple fluid and chemical transport with mechanical properties is of fundamental interest (as for example in Cowin (2004) and Ateshian (2007)). A candidate system is a vascularised tissue, where the elastic phase (comprised

[1]In this work we refer to interfacial mass exchange between the solid and the fluid phase as “growth", notwithstanding the sign of the mass flow that can actually indicate “resorption".

of cells, fluid and protein matrix) undergoes small strains and the fluid phase (the blood supply) flows slowly. In this scenario, nutrients are delivered to the cell population by diffusion across the blood vessel walls, and may induce cellular proliferation and hence growth. In the context of drugs delivered through the blood supply, cellular death and tissue regression may result (for example, tumour treatment by chemotherapeutics); indeed, poroelastic frameworks have been used to model solid tumours (see Bottaro and Ansaldi (2012), Roose et al. (2007)) and the discussions within) and to extract tissue-specific poroelastic parameters from biological experiments Roose et al. (2003). In a recent study Moeendarbary et al. (2013), a combination of experiments and theory has also been used to develop a poroelastic model for the cytoplasm of living cells. Alternative scenarios of interest include tissue engineering applications, where tissue growth must be tightly controlled by providing a biomechanical and biochemical environment that mimics the physiological scenario. In many such situations surface growth of a cellular phase is a key feature, for example, in tissue expansion in hollow fibre bioreactors Bettahalli et al. (2011) (among many others). In Humphrey and Rajagopal (2003), Lemon et al. (2006) and O'Dea et al. (2008) mixture theory has been developed for such biological applications, and the interplay between fluid and chemical transport and tissue growth are explored; however, such models present challenges if the evolution of solid stresses are included (see Baek et al. (2006) and Ambrosi et al. (2010) for examples and discussions). Also, a remarkable example of surface growth modelling can be found in Ciarletta et al. (2013), where a rigorous thermomechanical theory to account for the coupling between growth and mass transport phenomena across material interfaces is developed and biological examples are provided.

Inevitably any modelling approach faces challenges for integration with specific biological scenarios. Poroelastic materials (and, in general, multiphase frameworks) require the prescription of constitutive relationships to describe the fluid and solid stresses within the material of interest. In the case of linear elasticity, combined mathematical and experimental approaches (for example Roose et al. (2003), Moeendarbary et al. (2013)) have been used to extract solid parameters and make predictions around solid stress generation within living tissues. However, many biological soft tissues and cell aggregates behave as complex nonlinear-elastic (and possibly visco-plastic) materials, as in Pioletti and Rakotomanana (2000) and Preziosi et al. (2010), so that the increased complexity of such models has limited the extraction of relevant parameters from biological experiments. Indeed, model parameterisation is a much broader issue given that mechanical, chemical and kinetic properties are both tissue and species-specific, and this motivates collaboration between biologists and mathematicians to close the data gap.

In the current study we derive a new poroelastic model that includes mass exchange between the solid and the fluid phase. The focus is on the accretion (or appositional growth) that occurs at the interface between solid and fluid in the pores. The mass exchange at the microscale interface modifies the mechanical properties of the elastic phase (which may be anisotropic) and the hydraulic characterization of the flow in the microstructure. While the small strains assumption applies to ensure linearity in the equations, finite growth (finite advancement of the fluid-solid interphase) is retained. This regime of infinitesimal displacement of the solid phase with respect to a finite evolution of the geometry rules out applicability of the model to questions of emergence of residual stress, an issue that should be addressed in the framework of nonlinear elasticity Rodriguez et al. (1994).

The model is derived using a two-scale asymptotic expansion, which exploits the separation between the length scale of the pores and the macroscale of the material. Such an approach has already been developed in the literature. In Burridge and Keller (1981) Burridge and Keller present a rigorous derivation of Biot's equations of poroelasticity (see Biot (1941) and Biot (1962)) via the multiple scales method, whereas in Mikelic and Wheeler (2012) the interface law between a deformable porous medium containing a viscous fluid and an elastic body is derived using rigorous homogenisation and the two-scale convergence approach. In Shipley and Chapman (2010), Shipley and Chapman derive a dual porous medium model for vascular and interstitial fluid transport, and chemical transport, in a vascularised tissue. Here the averaging procedure is applied to a pore-scale description of coupled fluid transport and linear elasticity, with solid accretion at the interface between the two phases.

The chapter is organized as follows. In section 3.2, we formulate the mechanical model description in both the fluid and solid phases of the material. The solid phase is described using a linear elastic model, and is coupled to Stokes' flow for the fluid phase via the normal component of stress on the interface between the two. Continuity of the mass flux is also imposed on the fluid-solid moving interface Ateshian (2007), alongside a growth law to describe its temporal evolution. In section 3.3 non-dimensionalisation of the equations is performed. Section 3.4 is devoted to the multiple scales analysis and, in particular, the assumptions of length scale separation and local periodicity are highlighted. Under these assumptions, a formal two-scale asymptotic expansion is used to decouple micro and macro spatial variations, and thus derive the effective equations for a poroelastic growing material in section 3.5. The results are discussed in section 3.6, while in section 3.7 key limiting cases are highlighted; in particular the poroelastic equations of Burridge and

Keller (1981) are recovered in the limit of no growth, as well as the specific form of the model in the isotropic case. Finally, conclusions are presented in section 3.8.

3.2 The governing equations for a poroelastic growing medium

We consider a set $\Omega \in \mathbb{R}^3$, such that $\Omega = \Omega_s \cup \Omega_f$, where Ω_s and Ω_f represent the porous solid and fluid compartment, respectively. At this stage, every field of interest is a function of space $\boldsymbol{x}$ and time t. We assume the typical length scale r of the pores to be small compared to the characteristic size d of the domain (see Figure 3.1), so that their ratio

$$\frac{r}{d} = \epsilon \ll 1. \tag{3.1}$$

We consider an incompressible Newtonian fluid, so that, assuming that body forces and inertial effects can be neglected, the Stokes' problem holds in the fluid domain Ω_f:

$$\begin{aligned} \nabla \cdot \sigma &= 0 \\ \nabla \cdot \boldsymbol{v} &= 0, \end{aligned} \tag{3.2}$$

where σ denotes the fluid stress tensor defined by

$$\sigma = -p\mathsf{I} + \mu \left(\nabla \boldsymbol{v} + (\nabla \boldsymbol{v})^{\mathsf{T}} \right) \tag{3.3}$$

and $\boldsymbol{v}$, p, μ are the fluid velocity, pressure and viscosity respectively.
The solid phase is modelled as a linear, elastic solid, with inertia and body forces neglected, through

$$\nabla \cdot \tau = 0 \tag{3.4}$$

in Ω_s, where the solid stress tensor τ is given by

$$\tau = \mathbb{C} \nabla \boldsymbol{u}. \tag{3.5}$$

Here, $\boldsymbol{u}$ is the displacement vector for the solid compartment and $\mathbb{C}$ is the fourth rank elasticity tensor (with components denoted C_{ijkl} for $i, j, k, l = 1, 2, 3$), completely defined by its action on the symmetric part of $\nabla \boldsymbol{u}$ (see, e.g. Gurtin et al. (2010)), through:

$$\begin{aligned} \mathbb{C} \nabla \boldsymbol{u} &= \mathbb{C}\mathsf{e}, \\ \mathsf{e} := \frac{\nabla \boldsymbol{u} + (\nabla \boldsymbol{u})^{\mathsf{T}}}{2}. \end{aligned} \tag{3.6}$$

In other words, the skew component of $\nabla \boldsymbol{u}$ is in the kernel of $\mathbb{C}$. Note that if $\mathbb{C} \nabla \boldsymbol{u} = \mathbb{C}\mathsf{e} = 0$ then $\boldsymbol{u}$ is a rigid body motion.

Interface conditions for the fluid-structure interaction apply between the fluid and the solid phase. Following Ateshian (2007), the boundary $\Gamma := \partial\Omega_s \cap \partial\Omega_f$ is represented as a moving interface with velocity $\boldsymbol{v}_\Gamma$. Enforcing global mass conservation in Ω we define:

$$\rho_f(\boldsymbol{v} - \boldsymbol{v}_\Gamma) \cdot \boldsymbol{n} = \rho_s(\dot{\boldsymbol{u}} - \boldsymbol{v}_\Gamma) \cdot \boldsymbol{n} = \tilde{g} \quad \text{on } \Gamma, \tag{3.7}$$

where $\dot{\boldsymbol{u}}$, ρ_f and ρ_s are the solid phase velocity and the fluid and solid densities, respectively. Here $\boldsymbol{n}$ is the unit vector normal to the interface pointing into the solid region, and $\tilde{g}$ is the mass transfer rate per unit of surface area, which is assumed to be prescribed and strictly positive in the case of solid phase growth. Equation (3.7) accounts for mass exchange between the solid and fluid phase, and is equivalent to the following two scalar conditions:

$$\rho_s(\dot{\boldsymbol{u}} - \boldsymbol{v}_\Gamma) \cdot \boldsymbol{n} = \tilde{g} \quad \text{on } \Gamma, \tag{3.8}$$

$$\rho_f(\boldsymbol{v} - \boldsymbol{v}_\Gamma) \cdot \boldsymbol{n} = \tilde{g} \quad \text{on } \Gamma. \tag{3.9}$$

Equations (3.8, 3.9) relate the interface velocity to the mass transfer rate $\tilde{g}$ and to the solid and fluid velocities and densities, respectively. From (3.8) we obtain:

$$\boldsymbol{v}_\Gamma \cdot \boldsymbol{n} = \dot{\boldsymbol{u}} \cdot \boldsymbol{n} - \frac{\tilde{g}}{\rho_s} \quad \text{on } \Gamma. \tag{3.10}$$

Substituting (3.10) into equation (3.9) gives:

$$\rho_f \boldsymbol{v} \cdot \boldsymbol{n} - \rho_f \dot{\boldsymbol{u}} \cdot \boldsymbol{n} + \rho_f \frac{\tilde{g}}{\rho_s} = \tilde{g} \quad \text{on } \Gamma. \tag{3.11}$$

Finally, dividing by ρ_f and rearranging terms, equation (3.11) yields the following jump condition for the fluid and solid velocities at the interface:

$$(\boldsymbol{v} - \dot{\boldsymbol{u}}) \cdot \boldsymbol{n} = \tilde{g}\left(\frac{1}{\rho_f} - \frac{1}{\rho_s}\right) \quad \text{on } \Gamma. \tag{3.12}$$

In order to simplify notation, we denote by g the right hand side of (3.12), so that

$$g := \tilde{g}\left(\frac{1}{\rho_f} - \frac{1}{\rho_s}\right). \tag{3.13}$$

The tangential components of the velocity and all components of the stress on Γ are continuous across the interface, such that

$$\tau \boldsymbol{n} = \sigma \boldsymbol{n} \qquad \text{on } \Gamma \tag{3.14}$$

$$\dot{\boldsymbol{u}} \cdot \boldsymbol{t} = \boldsymbol{v} \cdot \boldsymbol{t} \qquad \text{on } \Gamma, \tag{3.15}$$

where $\boldsymbol{t}$ is any unit vector tangent to the interface.

3.2.1 Kinematics of the moving interface

The interface velocity (which is directed along $\boldsymbol{n}$), satisfies

$$\boldsymbol{v}_\Gamma \cdot \boldsymbol{n} = \boldsymbol{v} \cdot \boldsymbol{n} - \frac{\tilde{g}}{\rho_f} = \dot{\boldsymbol{u}} \cdot \boldsymbol{n} - \frac{\tilde{g}}{\rho_s}, \tag{3.16}$$

where equations (3.8, 3.9) have been used for the simplification. The function $\tilde{g}$ accounts for surface growth and should be constitutively specified according to the physical system at hand. We further note that, as the interface is moving, the fluid and solid subdomains $\Omega_s(t)$ and $\Omega_f(t)$ change in time [2]. The assumptions underlying the material descriptions of the solid and fluid phases (small deformation of the solid elastic phase, negligible inertia) do not affect surface growth. The present framework allows for finite growth at a pore scale; the position of the fluid-solid interface evolves in time according to the interface velocity condition (3.16), and global mass conservation in Ω is ensured by the jump condition (3.12). Assuming that the moving interface is described by $F(\boldsymbol{x}, t) = 0$, its kinematics are described by:

$$\frac{\partial F}{\partial t} + \nabla F \cdot \boldsymbol{v}_\Gamma = 0. \tag{3.17}$$

Equations (3.2-3.5) describing the mechanics of the fluid and solid phases, together with the interface conditions (3.12, 3.14, 3.15) and the kinematic relationships for the evolution of the interface (3.16–3.17), represent the system of partial differential equations to be solved for every $\boldsymbol{x} \in \Omega$ and for every $t \in (0, T)$, $T \in \mathbb{R}^+$, (subject to appropriate initial and boundary conditions). When $\tilde{g} = 0$, there is no growth and the normal components of the fluid and solid velocities are equal and are the velocity of the interface itself. In this particular case the problem reduces to a standard linearized fluid-structure interaction problem as in Burridge and Keller (1981).

3.3 Non-dimensionalisation

Next we formulate the model in non-dimensional form in order to clarify the mutual weight of the relevant physical mechanisms. The model derived in this chapter does not aim to be application-specific; as such, we do not motivate the non-dimensionalisation via specific parameter values (see, e.g. Shipley and Chapman (2010) and Roose and Swartz (2012) for biological tissues), but instead we perform a formal non-dimensionalisation to highlight the proper asymptotic behaviour of the relevant fields. We rescale

$$\boldsymbol{x} = d\boldsymbol{x}', \quad \boldsymbol{v} = \frac{Cr^2}{\mu_c}\boldsymbol{v}', \quad \boldsymbol{v}_\Gamma = \frac{Cr^2}{\mu_c}\boldsymbol{v}'_\Gamma \quad p = Cdp', \quad \boldsymbol{u} = d\boldsymbol{u}', \quad t = \frac{d\mu_c}{Cr^2}t',$$

[2] We avoid denoting this time dependence explicitly in the following sections for simplicity of notation

$$\tilde{g} = \rho_c \frac{Cr^2}{\mu_c} \tilde{g}', \quad \mu = \mu_c \mu', \quad \rho_s = \rho_c \rho_s', \quad \rho_f = \rho_c \rho_f', \quad \mathbb{C} = Cd\mathbb{C}',$$

$$g = \frac{Cr^2}{\mu_c} g', \quad g' = \tilde{g}' \left(\frac{1}{\rho_f'} - \frac{1}{\rho_s'} \right), \quad \tau = Cd\tau', \quad \sigma = Cd\sigma', \tag{3.18}$$

where C, ρ_c, μ_c denote the characteristic pressure gradient, density and viscosity, respectively. Here, we scale the spatial coordinate and the elastic displacement by the characteristic length scale of the domain d, whereas the non–dimensional form of the velocity is suggested by the parabolic profile of a viscous fluid flowing in a straight channel of radius r

$$V = \frac{Cr^2}{\mu_c}. \tag{3.19}$$

Further, we scale pressure and stresses by adopting the same reference pressure gradient exploited in (3.19), (multiplied by the reference length scale d) and time assuming d/V as a reference time scale for slow flow of the fluid phase (which is analogous to that for deformation of the elastic material).

Thus, exploiting (3.18) and dropping the prime notation for the sake of simplicity, equations (3.2-3.5), (3.12, 3.14, 3.15) become:

$$\nabla \cdot \sigma = 0 \qquad \text{in } \Omega_f \tag{3.20}$$

$$-p\mathsf{I} + \epsilon^2 \mu \left(\nabla \boldsymbol{v} + (\nabla \boldsymbol{v})^{\mathsf{T}} \right) = \sigma \qquad \text{in } \Omega_f \tag{3.21}$$

$$\nabla \cdot \boldsymbol{v} = 0 \qquad \text{in } \Omega_f \tag{3.22}$$

$$\tau \boldsymbol{n} = \sigma \boldsymbol{n} \qquad \text{on } \Gamma \tag{3.23}$$

$$(\boldsymbol{v} - \dot{\boldsymbol{u}}) \cdot \boldsymbol{n} = g \qquad \text{on } \Gamma \tag{3.24}$$

$$\dot{\boldsymbol{u}} \cdot \boldsymbol{t} = \boldsymbol{v} \cdot \boldsymbol{t} \quad \text{on } \Gamma \tag{3.25}$$

$$\nabla \cdot \tau = 0 \qquad \text{in } \Omega_s \tag{3.26}$$

$$\mathbb{C} \nabla \boldsymbol{u} = \tau \qquad \text{in } \Omega_s. \tag{3.27}$$

The ϵ^2 coefficient that appears in (3.21) follows when assuming a reference velocity of the type (3.19) and is the standard scaling for Stokes' flow in porous media (see for example Sanchez-Palencia (1980), Holmes (1995), Burridge and Keller (1981), and Arbogast and Lehr (2006)), which reflects the asymptotic behaviour of the characteristic fluid velocity in the pores, that scales with ϵ^2 as $\epsilon \to 0$, as noted in Sanchez-Palencia (1983).

The kinematic condition is rewritten in non–dimensional form using the pore spatial scale r, so that

the relevant time scale is

$$T_g = \frac{r}{V} = \epsilon \frac{d\mu_c}{Cr^2}. \tag{3.28}$$

The interface kinematic equations (3.16, 3.17) with the time scale (3.28) yields, in non–dimensional form

$$\frac{1}{\epsilon}\frac{\partial F}{\partial t} + \nabla F \cdot \boldsymbol{v}_\Gamma = 0, \tag{3.29}$$

$$\boldsymbol{v}_\Gamma \cdot \boldsymbol{n} = \boldsymbol{v} \cdot \boldsymbol{n} - \frac{\tilde{g}}{\rho_f} = \dot{\boldsymbol{u}} \cdot \boldsymbol{n} - \frac{\tilde{g}}{\rho_s}, \tag{3.30}$$

where the prime notation has again been neglected, and the ϵ^{-1} term appearing at the left hand side of (3.29) accounts for the time scale separation between finite growth and linearized motion of the material.

3.4 Multiple scales formulation

In this section we employ a formal two-scales asymptotic expansion widely exploited in the literature (for example Sanchez-Palencia (1980), Sanchez-Palencia (1983), Holmes (1995), Mei and Vernescu (2010) and Hornung (1997)) to derive a continuum macroscale model for the system of equations (3.20-3.27, 3.29-3.30). Since $\epsilon \ll 1$, we enforce a sharp length scale separation between r (the *microscale*) and d (the *macroscale*), defining:

$$\boldsymbol{y} := \frac{\boldsymbol{x}}{\epsilon}. \tag{3.31}$$

Following the usual approach in multiscale analysis, from now on $\boldsymbol{x}$ and $\boldsymbol{y}$ denote independent variables, representing the macro and micro spatial scale, respectively. In the analysis that follows, all the fields (denoted collectively by ψ) and the elasticity tensor $\mathbb{C}$ are functions of these independent spatial variables:

$$\psi = \psi(\boldsymbol{x}, \boldsymbol{y}, t), \quad \mathbb{C} = \mathbb{C}(\boldsymbol{x}, \boldsymbol{y}),$$

and the differential operators transform accordingly,

$$\nabla \to \nabla_{\boldsymbol{x}} + \frac{1}{\epsilon}\nabla_{\boldsymbol{y}}. \tag{3.32}$$

Now we formally perform the following multiple scales expansion in power series of ϵ for every field ψ:

$$\psi_\epsilon(\boldsymbol{x}, \boldsymbol{y}, t) = \sum_{l=0}^{\infty} \psi^{(l)}(\boldsymbol{x}, \boldsymbol{y}, t)\epsilon^l. \tag{3.33}$$

The components $\psi^{(l)}$ are defined for every $\boldsymbol{x}$ belonging to the macroscale domain, whereas $\boldsymbol{y}$ spans only the specific portion of the microscale where ψ is defined. We further assume regularity of the

microstructure, so that every $\psi^{(l)}$ and $\mathbb{C}$ are $\boldsymbol{y}$-periodic. This means that *local* periodicity only is assumed, such that any (regular enough) macroscale variation in any field ψ is in principle allowed. Furthermore, since the surface description F can macroscopically vary, macroscale variations in the interface Γ are also permitted. A schematic of the setup is shown in Figure 3.1.

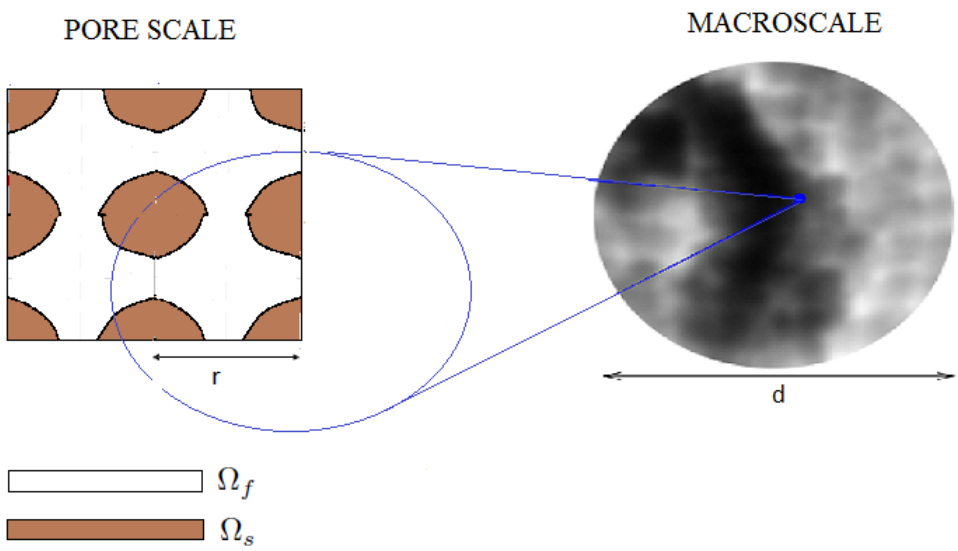

Figure 3.1: *A 2D cartoon of the pore scale (left), depicting the porous structure of the medium on the microscale and the corresponding* homogenised *one on the macroscale (right), where the geometry of the microstructure is smoothed out.*

Under the transformation (3.32), equations (3.20-3.27, 3.29-3.30) become:

$$\nabla_{\boldsymbol{y}} \cdot \sigma_\epsilon + \epsilon \nabla_{\boldsymbol{x}} \cdot \sigma_\epsilon = 0 \qquad \text{in } \Omega_f \tag{3.34}$$

$$p_\epsilon \mathsf{I} - \epsilon\mu \left(\nabla_{\boldsymbol{y}} \boldsymbol{v}_\epsilon + (\nabla_{\boldsymbol{y}} \boldsymbol{v}_\epsilon)^\mathsf{T} \right) - \epsilon^2 \mu \left(\nabla_{\boldsymbol{x}} \boldsymbol{v}_\epsilon + (\nabla_{\boldsymbol{x}} \boldsymbol{v}_\epsilon)^\mathsf{T} \right) = \sigma_\epsilon \qquad \text{in } \Omega_f \tag{3.35}$$

$$\nabla_{\boldsymbol{y}} \cdot \boldsymbol{v}_\epsilon + \epsilon \nabla_{\boldsymbol{x}} \cdot \boldsymbol{v}_\epsilon = 0 \qquad \text{in } \Omega_f \tag{3.36}$$

$$\tau_\epsilon \boldsymbol{n} = \sigma_\epsilon \boldsymbol{n} \qquad \text{on } \Gamma \tag{3.37}$$

$$\dot{\boldsymbol{u}}_\epsilon \cdot \boldsymbol{t} = \boldsymbol{v}_\epsilon \cdot \boldsymbol{t} \qquad \text{on } \Gamma \tag{3.38}$$

$$\boldsymbol{v}_\epsilon \cdot \boldsymbol{n} - \dot{\boldsymbol{u}}_\epsilon \cdot \boldsymbol{n} = g_\epsilon \qquad \text{on } \Gamma \tag{3.39}$$

$$\nabla_{\boldsymbol{y}} \cdot \tau_\epsilon + \epsilon \nabla_{\boldsymbol{x}} \cdot \tau_\epsilon = 0 \qquad \text{in } \Omega_s \tag{3.40}$$

$$\frac{1}{\epsilon} \mathbb{C} \nabla_{\boldsymbol{y}} \boldsymbol{u}_\epsilon + \mathbb{C} \nabla_{\boldsymbol{x}} \boldsymbol{u}_\epsilon = \tau_\epsilon \qquad \text{in } \Omega_s \tag{3.41}$$

$$\frac{\partial F_\epsilon}{\partial t} + \nabla_{\boldsymbol{y}} F_\epsilon \cdot \boldsymbol{v}_{\Gamma\epsilon} + \epsilon \nabla_{\boldsymbol{x}} F_\epsilon \cdot \boldsymbol{v}_{\Gamma\epsilon} = 0 \tag{3.42}$$

$$\boldsymbol{v}_{\Gamma\epsilon} \cdot \boldsymbol{n} = \boldsymbol{v}_\epsilon \cdot \boldsymbol{n} - \frac{\tilde{g}_\epsilon}{\rho_f} = \dot{\boldsymbol{u}}_\epsilon \cdot \boldsymbol{n} - \frac{\tilde{g}_\epsilon}{\rho_s} \quad \text{on } \Gamma, \tag{3.43}$$

where p_ϵ, $\boldsymbol{v}_\epsilon$, $\boldsymbol{u}_\epsilon$, σ_ϵ, τ_ϵ, $\boldsymbol{v}_{\Gamma\epsilon}$, $\tilde{g}_\epsilon$, g_ϵ, F_ϵ are the representation in the power series form (3.33) of the corresponding fields. Next we substitute power series expansions of the form (3.33) into the relevant fields in (3.34-3.43); by equating coefficients of ϵ^l for $l = 0, 1, ...$, we derive the macroscale model for the poroelastic growing medium in terms of the leading (zero-th) order relevant fields.

3.5 The macroscopic model

In this section we derive a closed system of partial differential equations for the macroscopic behaviour of the leading order fields $p^{(0)}$, $\boldsymbol{v}^{(0)}$, $\boldsymbol{u}^{(0)}$, by averaging over the zero-th and first order systems corresponding to (3.34–3.43) .

Whenever a component of the asymptotic expansion retains a dependence on the microscale $\boldsymbol{y}$, we can take its integral average, defined as follows:

$$\langle \psi \rangle_k = \frac{1}{|\Omega|} \int_{\Omega_k} \psi(\boldsymbol{x}, \boldsymbol{y}, t)\, \mathrm{d}\boldsymbol{y} \quad k = f, s, \tag{3.44}$$

where $|\Omega|$ represents the volume of the domain and integration is performed over the microscale $\boldsymbol{y}$. Because of $\boldsymbol{y}$-periodicity, the integral average can be performed over one representative cell only (see Figure 1): from now on, (3.44) should be understood as a cell average, where $|\Omega|$ is replaced by the cell volume and Ω_k by the corresponding k-phase subvolume.

Equating coefficients of ϵ^0 in the system (3.34-3.43) yields:

$$\nabla_{\boldsymbol{y}} \cdot \sigma^{(0)} = 0 \qquad \text{in } \Omega_f \tag{3.45}$$

$$\sigma^{(0)} = -p^{(0)} \mathsf{I} \qquad \text{in } \Omega_f \tag{3.46}$$

$$\nabla_{\boldsymbol{y}} \cdot \boldsymbol{v}^{(0)} = 0 \qquad \text{in } \Omega_f \tag{3.47}$$

$$\tau^{(0)} \boldsymbol{n} = \sigma^{(0)} \boldsymbol{n} \qquad \text{on } \Gamma \tag{3.48}$$

$$\dot{\boldsymbol{u}}^{(0)} \cdot \boldsymbol{t} = \boldsymbol{v}^{(0)} \cdot \boldsymbol{t} \qquad \text{on } \Gamma \tag{3.49}$$

$$\boldsymbol{v}^{(0)} \cdot \boldsymbol{n} - \dot{\boldsymbol{u}}^{(0)} \cdot \boldsymbol{n} = g^{(0)} \qquad \text{on } \Gamma \tag{3.50}$$

$$\nabla_{\boldsymbol{y}} \cdot \tau^{(0)} = 0 \qquad \text{in } \Omega_s \tag{3.51}$$

$$\mathbb{C} \nabla_{\boldsymbol{y}} \boldsymbol{u}^{(0)} = 0 \qquad \text{in } \Omega_s \tag{3.52}$$

$$\frac{\partial F^{(0)}}{\partial t} + \nabla_{\boldsymbol{y}} F^{(0)} \cdot \boldsymbol{v}_\Gamma^{(0)} = 0 \tag{3.53}$$

$$\boldsymbol{v}_\Gamma^{(0)} \cdot \boldsymbol{n} = \boldsymbol{v}^{(0)} \cdot \boldsymbol{n} - \frac{\tilde{g}^{(0)}}{\rho_f} = \dot{\boldsymbol{u}}^{(0)} \cdot \boldsymbol{n} - \frac{\tilde{g}^{(0)}}{\rho_s} \qquad \text{on } \Gamma, \tag{3.54}$$

whereas equating coefficients of ϵ^1 in equations (3.34-3.41) yields

$$\nabla_{\boldsymbol{y}} \cdot \sigma^{(1)} + \nabla_{\boldsymbol{x}} \cdot \sigma^{(0)} = 0 \qquad \text{in } \Omega_f \tag{3.55}$$

$$-p^{(1)}\mathsf{I} + \mu \left(\nabla_{\boldsymbol{y}} \boldsymbol{v}^{(0)} + (\nabla_{\boldsymbol{y}} \boldsymbol{v}^{(0)})^{\mathsf{T}} \right) = \sigma^{(1)} \qquad \text{in } \Omega_f \tag{3.56}$$

$$\nabla_{\boldsymbol{y}} \cdot \boldsymbol{v}^{(1)} + \nabla_{\boldsymbol{x}} \cdot \boldsymbol{v}^{(0)} = 0 \qquad \text{in } \Omega_f \tag{3.57}$$

$$\tau^{(1)}\boldsymbol{n} = \sigma^{(1)}\boldsymbol{n} \qquad \text{on } \Gamma \tag{3.58}$$

$$\dot{\boldsymbol{u}}^{(1)} \cdot \boldsymbol{t} = \boldsymbol{v}^{(1)} \cdot \boldsymbol{t} \qquad \text{on } \Gamma \tag{3.59}$$

$$\boldsymbol{v}^{(1)} \cdot \boldsymbol{n} - \dot{\boldsymbol{u}}^{(1)} \cdot \boldsymbol{n} = g^{(1)} \qquad \text{on } \Gamma \tag{3.60}$$

$$\nabla_{\boldsymbol{y}} \cdot \tau^{(1)} + \nabla_{\boldsymbol{x}} \cdot \tau^{(0)} = 0 \qquad \text{in } \Omega_s \tag{3.61}$$

$$\mathbb{C} \left(\nabla_{\boldsymbol{y}} \boldsymbol{u}^{(1)} + \nabla_{\boldsymbol{x}} \boldsymbol{u}^{(0)} \right) = \tau^{(0)} \qquad \text{in } \Omega_s. \tag{3.62}$$

Equations (3.45-3.46) infer that $p^{(0)}$ does not depend on the microscale $\boldsymbol{y}$, hence

$$p^{(0)} = p^{(0)}(\boldsymbol{x}, t). \tag{3.63}$$

Equation (3.52) implies, together with the elasticity tensor property (3.6), that $\boldsymbol{u}^{(0)}$ must correspond to a rigid body motion. Since the only $\boldsymbol{y}$-periodic solution of this type is $\boldsymbol{y}$-constant, we see that:

$$\boldsymbol{u}^{(0)} = \boldsymbol{u}^{(0)}(\boldsymbol{x}, t). \tag{3.64}$$

Hence the leading order solid displacement field is also locally constant.

3.5.1 Macroscale fluid flow

In order to obtain information on the leading order velocity of the fluid $\boldsymbol{v}^{(0)}$, we note that, enforcing (3.46), equations (3.49-3.50,3.55-3.56) form a Stokes-type boundary value problem for $(\boldsymbol{v}^{(0)},\, p^{(1)})$ which can be rewritten in terms of the relative fluid-solid displacement $\boldsymbol{w}$ defined by:

$$\dot{\boldsymbol{w}}(\boldsymbol{x}, \boldsymbol{y}, t) := \boldsymbol{v}^{(0)}(\boldsymbol{x}, \boldsymbol{y}, t) - \dot{\boldsymbol{u}}^{(0)}(\boldsymbol{x}, t), \tag{3.65}$$

as follows:

$$\mu \nabla_{\boldsymbol{y}}^2 \dot{\boldsymbol{w}} - \nabla_{\boldsymbol{y}} p^{(1)} - \nabla_{\boldsymbol{x}} p^{(0)} = 0 \qquad \text{in } \Omega_f \tag{3.66}$$

$$\nabla_{\boldsymbol{y}} \cdot \dot{\boldsymbol{w}} = 0 \qquad \text{in } \Omega_f \tag{3.67}$$

$$\dot{\boldsymbol{w}} \cdot \boldsymbol{t} = 0 \qquad \text{on } \Gamma \tag{3.68}$$

$$\dot{\boldsymbol{w}} \cdot \boldsymbol{n} = g^{(0)} \qquad \text{on } \Gamma, \tag{3.69}$$

where the knowledge that $\boldsymbol{u}^{(0)}$ is locally constant has been explicitly used. Now we exploit linearity together with (3.63) and propose the following ansatz for the solution $(\dot{\boldsymbol{w}},\, p^{(1)})$:

$$\dot{\boldsymbol{w}} = -\tilde{\mathsf{W}}\nabla_{\boldsymbol{x}} p^{(0)} + \boldsymbol{h}, \tag{3.70}$$

$$p^{(1)} = -\boldsymbol{P} \cdot \nabla_{\boldsymbol{x}} p^{(0)} + p_h, \tag{3.71}$$

where $p^{(1)}$ is defined up to an arbitrary $\boldsymbol{y}$-constant function and the quantities $(\tilde{\mathsf{W}}, \boldsymbol{P})$, $(\boldsymbol{h}, p_h)$ satisfy the following differential *cell problems*, to be solved on the single representative cell

$$\mu \nabla_{\boldsymbol{y}}^2 \tilde{\mathsf{W}}^{\mathsf{T}} - \nabla_{\boldsymbol{y}} \boldsymbol{P} + \mathsf{I} = 0 \quad \text{in } \Omega_f \tag{3.72}$$

$$\nabla_{\boldsymbol{y}} \cdot \tilde{\mathsf{W}}^{\mathsf{T}} = 0 \quad \text{in } \Omega_f \tag{3.73}$$

$$\tilde{\mathsf{W}} = 0 \quad \text{on } \Gamma, \tag{3.74}$$

$$\mu \nabla_{\boldsymbol{y}}^2 \boldsymbol{h} - \nabla_{\boldsymbol{y}} p_h = 0 \qquad \text{in } \Omega_f \tag{3.75}$$

$$\nabla_{\boldsymbol{y}} \cdot \boldsymbol{h} = 0 \qquad \text{in } \Omega_f \tag{3.76}$$

$$\boldsymbol{h} \cdot \boldsymbol{t} = 0 \qquad \text{on } \Gamma \tag{3.77}$$

$$\boldsymbol{h} \cdot \boldsymbol{n} = g^{(0)} \qquad \text{on } \Gamma. \tag{3.78}$$

The above system of equations (3.72–3.74) and (3.75–3.78) are supplemented by periodicity conditions on the unit cell in $\boldsymbol{y}$, together with suitable uniqueness conditions for $\boldsymbol{P}$, p_h. Example conditions are

$$\langle \boldsymbol{P} \rangle_f = \boldsymbol{0}, \quad \langle p_h \rangle_f = 0. \tag{3.79}$$

Exploiting definition (3.65) and equation (3.70), we notice that $\boldsymbol{v}^{(0)}$, and hence its cell average, can be recovered in terms of $p^{(0)}$ and $\boldsymbol{u}^{(0)}$ as follows:

$$\langle \dot{\boldsymbol{w}} \rangle_f = \left\langle \boldsymbol{v}^{(0)} \right\rangle_f - \phi \dot{\boldsymbol{u}}^{(0)} = -\left\langle \tilde{\mathsf{W}} \right\rangle_f \nabla_{\boldsymbol{x}} p^{(0)} + \langle \boldsymbol{h} \rangle_f \,, \tag{3.80}$$

where

$$\phi(\boldsymbol{x}, t) := \frac{|\Omega_f|}{|\Omega|} \tag{3.81}$$

is the porosity of the material.

Remark 3.1. Exploiting the local incompressibility constraint (3.76) together with interface condition (3.78) and $\boldsymbol{y}$-periodicity, we note that:

$$0 = \int_{\Omega_f} \nabla_{\boldsymbol{y}} \cdot \boldsymbol{h} \, \mathrm{d}\boldsymbol{y} = \int_{\partial\Omega_f} \boldsymbol{h} \cdot \boldsymbol{n} \, \mathrm{dS}_y = \int_{\Gamma} \boldsymbol{h} \cdot \boldsymbol{n} \, \mathrm{dS}_y = \int_{\Gamma} g^{(0)} \, \mathrm{dS}_y. \tag{3.82}$$

Hence, the cell problem (3.75-3.78) has a solution if and only if the compatibility condition

$$\int_{\Gamma} g^{(0)} \, \mathrm{dS}_y = 0 \tag{3.83}$$

is satisfied. Given that

$$g^{(0)} = \tilde{g}^{(0)} \left(\frac{1}{\rho_f} - \frac{1}{\rho_s} \right), \tag{3.84}$$

and $\tilde{g}^{(0)} \neq 0$ when surface growth is occurring, condition (3.83) is automatically satisfied whenever the density difference between the fluid and solid compartment is negligible,

$$\rho_f = \rho_s. \tag{3.85}$$

In this case, every $g^{(l)}$ for $l = 0, 1, ...$ and in particular $g^{(0)}$ reduces to zero and the unique solution of the cell problem (3.75-3.78) is $\boldsymbol{h} = \boldsymbol{0}$. This is not surprising, as the interface condition (3.78) is directly related to the jump condition (3.69), that arises from mass conservation for a moving interface. Indeed, if $\rho_f = \rho_s$, then mass conservation is automatic, the fluid and solid velocities on the interface are equal, and as a consequence $\boldsymbol{h} \cdot \boldsymbol{n} = 0$ on Γ. It is worth remarking that, $g^{(0)} = 0$ does not imply $\tilde{g}^{(0)} = 0$: the interface moves in absence of a density difference, with leading-order velocity driven by $\tilde{g}^{(0)}$ and provided by equation (3.54). The assumption (3.85) applies in most applications of interest, for example interstitial fluid versus cells in biological tissues, or water versus ice in glaciers.

Whenever (3.85) does not apply and there is a density jump between the solid and fluid phases, possible choices for the growth law $\tilde{g}^{(0)}$ are restricted by the compatibility condition (3.83). For example, any functional form of $\tilde{g}^{(0)}$ that takes the form

$$\tilde{g}^{(0)} = \boldsymbol{v}^* \cdot \boldsymbol{n} \tag{3.86}$$

satisfies the compatibility condition (3.83) provided that $\boldsymbol{v}^*$ is a locally divergence-free vector field,

$$\nabla_{\boldsymbol{y}} \cdot \boldsymbol{v}^* = 0 \text{ in } \Omega_f. \tag{3.87}$$

Clearly, a prescription of the type (3.86) is in general time-dependent because $\boldsymbol{n}$ evolves in time while the interface is moving. In practice in this scenario, given a suitable initial condition on the interface position, it suffices to prescribe the velocity field $\boldsymbol{v}^*$ (satisfying (3.87)); from here the updated interface normal vector $\boldsymbol{n}$ may be calculated using the leading-order kinematics of the interface (3.53) for every $t \in (0, T)$.

3.5.2 Effective poroelasticity

Finally, we require a set of macroscale equations to close the system for the solid displacement $\boldsymbol{u}^{(0)}$ and the fluid pressure $p^{(0)}$. Taking the integral average of the sum of (3.55) and (3.61) and using the divergence theorem yields

$$\frac{1}{|\Omega|}\int_{\Gamma}\left(\sigma^{(1)}\boldsymbol{n}-\tau^{(1)}\boldsymbol{n}\right)\,\mathrm{dS}_y=\left\langle\nabla_{\boldsymbol{x}}\cdot\tau^{(0)}\right\rangle_s-\phi\nabla_{\boldsymbol{x}}p^{(0)}, \tag{3.88}$$

where the contributions from the periodic boundaries cancel and the knowledge that $p^{(0)}$ is locally constant has been exploited. Given the normal stress condition on internal boundaries (3.58), (3.88) reduces to:

$$\left\langle\nabla_{\boldsymbol{x}}\cdot\tau^{(0)}\right\rangle_s-\phi\nabla_{\boldsymbol{x}}p^{(0)}=0. \tag{3.89}$$

Equation (3.89) can be rewritten in terms of $\left\langle\tau^{(0)}\right\rangle_s$ by means of the Reynolds transport theorem (see for example Holmes (1995)) and using $\boldsymbol{y}$-periodicity, namely:

$$\int_{\Omega_s}\nabla_{\boldsymbol{x}}\cdot\tau^{(0)}\,\mathrm{d}\boldsymbol{y}=\nabla_{\boldsymbol{x}}\cdot\int_{\Omega_s}\tau^{(0)}\,\mathrm{d}\boldsymbol{y}+\int_{\Gamma}\tau^{(0)}\boldsymbol{q}\,\mathrm{dS}_y, \tag{3.90}$$

where the vector $\boldsymbol{q}$, which accounts for macroscale variations in the interface Γ, is defined by

$$\boldsymbol{q}:=\left(\nabla_{\boldsymbol{x}}\boldsymbol{r}(\boldsymbol{x},\boldsymbol{y},t)\right)^{\mathsf{T}}\boldsymbol{n}. \tag{3.91}$$

Here the fact that the unit outward normal vector to $\partial\Omega_s$ is $-\boldsymbol{n}$ has been used in the simplification. The vector $\boldsymbol{r}$ (see Figure 3.2), which spans the interface Γ, should be recovered by integration of the interface descriptor (3.53). When each Ω_k is independent of the macroscale, $\boldsymbol{q}=0$ and we say that the medium is *macroscopically uniform*. Using (3.89) together with (3.90) we obtain:

$$\nabla_{\boldsymbol{x}}\cdot\left\langle\tau^{(0)}\right\rangle_s-\phi\nabla_{\boldsymbol{x}}p^{(0)}+\boldsymbol{s}_\tau=0, \tag{3.92}$$

where

$$\boldsymbol{s}_\tau:=\frac{1}{|\Omega|}\int_{\Gamma}\tau^{(0)}\boldsymbol{q}\,\mathrm{dS}_y \tag{3.93}$$

is the momentum production due to macroscopic changes in the solid-fluid interface.

Now we notice that (3.48, 3.51, 3.62) form a linear Neumann-type differential problem for $\boldsymbol{u}^{(1)}$ which can be written, enforcing (3.63, 3.64), as follows:

$$\nabla_{\boldsymbol{y}}\cdot\left(\mathbb{C}\nabla_{\boldsymbol{y}}\boldsymbol{u}^{(1)}\right)=0 \qquad \text{in } \Omega_s \tag{3.94}$$

$$\left(\mathbb{C}\nabla_{\boldsymbol{y}}\boldsymbol{u}^{(1)}+\mathbb{C}\nabla_{\boldsymbol{x}}\boldsymbol{u}^{(0)}\right)\boldsymbol{n}=-p^{(0)}\boldsymbol{n} \quad \text{on } \Gamma, \tag{3.95}$$

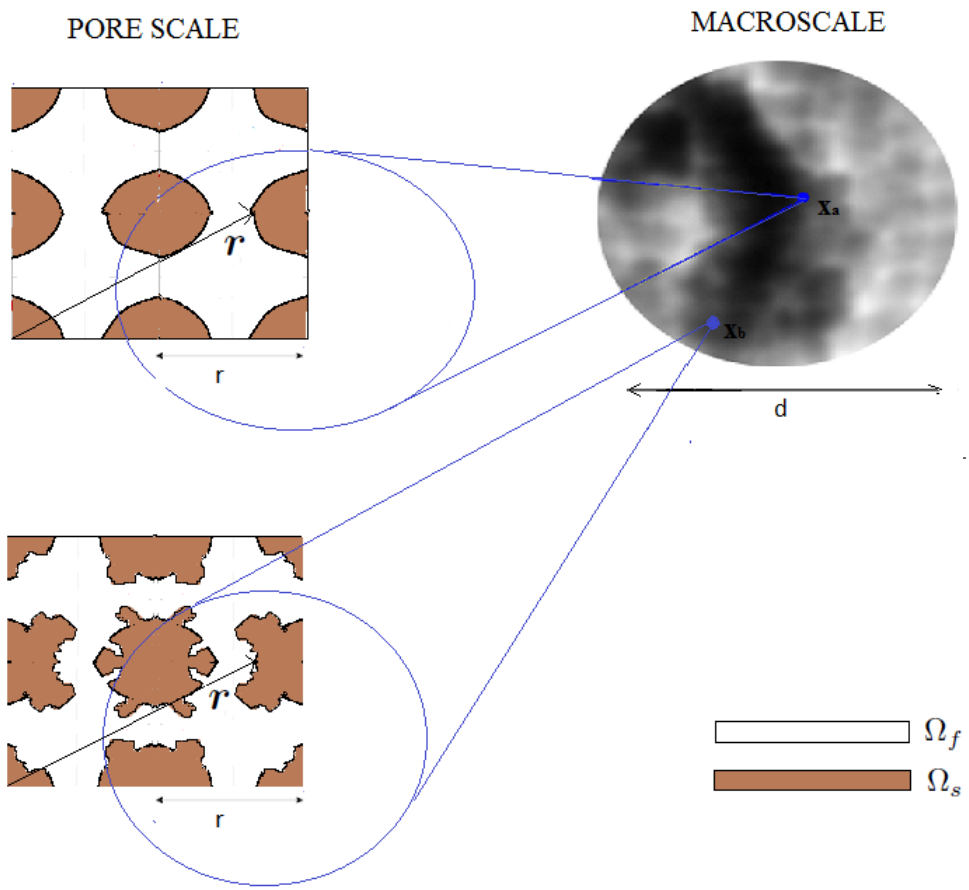

Figure 3.2: *2D schematic of a non-macroscopically uniform medium. In this case, the model supports macroscale variations of the microstructure so that, for every fixed $t \in (0, T)$, the interface position vector $\boldsymbol{r}$ related to the same (homologous by $\boldsymbol{y}$-periodicity) local point is varying with respect to $\boldsymbol{x}$, that is $\boldsymbol{r}(\boldsymbol{x_a}, \boldsymbol{y}, t) \neq \boldsymbol{r}(\boldsymbol{x_b}, \boldsymbol{y}, t)$. Whenever the medium exhibits such variations, one cell problem for every $\boldsymbol{x}$ of the homogenised domain needs to be solved.*

equipped with $\boldsymbol{y}$-periodicity in Ω_s. Since $\boldsymbol{u}^{(1)}$ is guaranteed to be a bounded vector function of $\boldsymbol{y}$ by local periodicity, then the solution is found to be unique up to an arbitrary $\boldsymbol{y}$-constant vector field and can be expressed, exploiting linearity of the problem, as:

$$\boldsymbol{u}^{(1)} = \mathcal{A}\nabla_{\boldsymbol{x}}\boldsymbol{u}^{(0)} + \boldsymbol{a}p^{(0)}, \tag{3.96}$$

where $\mathcal{A}$ is a rank three tensor, with components denoted A_{ijk} for $i, j, k = 1, 2, 3$.

The cell problem for the vector $\boldsymbol{a}$ is given by:

$$\nabla_{\boldsymbol{y}} \cdot (\mathbb{C}\nabla_{\boldsymbol{y}}\boldsymbol{a}) = 0 \qquad \text{in } \Omega_s \tag{3.97}$$

$$(\mathbb{C}\nabla_{\boldsymbol{y}}\boldsymbol{a})\,\boldsymbol{n} = -\boldsymbol{n} \qquad \text{on } \Gamma, \tag{3.98}$$

whereas $\mathcal{A}$ satisfies, in component notation:

$$\frac{\partial}{\partial y_j}\left(C_{ijkl}\frac{\partial A_{k\nu\gamma}}{\partial y_l}\right) = 0 \quad \text{in } \Omega_s \tag{3.99}$$

$$C_{ijkl}\frac{\partial A_{k\nu\gamma}}{\partial y_l}n_j + C_{ij\nu\gamma}n_j = 0 \quad \text{on } \Gamma, \tag{3.100}$$

where $i, j, k, l, \nu, \gamma = 1...3$ and summation over repeated notation indices is used.

As previously, a further condition for $\boldsymbol{a}$ and each A_{ijk} is required to ensure uniqueness; example conditions are:

$$\langle \boldsymbol{a} \rangle_s = 0, \quad \langle A_{ijk} \rangle_s = 0 \;\; \forall\, i, j, k = 1...3. \tag{3.101}$$

Note that, since $\boldsymbol{u}^{(1)}$ is directly related to the leading order solid stress tensor via (3.62), the form of $\boldsymbol{u}^{(1)}$ given by (3.96) indicates that $\tau^{(0)}$ (and also its cell average) is a function of both the gradient of the leading order solid displacement and the macroscopic fluid pressure $p^{(0)}$, as expected for a poroelastic material. In fact, enforcing equation (3.96), we can exploit equation (3.62), which relates the leading order solid stress tensor to $\nabla_{\boldsymbol{x}}\boldsymbol{u}^{(0)}$ and $\nabla_{\boldsymbol{y}}\boldsymbol{u}^{(1)}$, to provide an explicit relationship for $\tau^{(0)}$ as a function of $\nabla_{\boldsymbol{x}}\boldsymbol{u}^{(0)}$ and $p^{(0)}$, namely:

$$\tau^{(0)} = (\mathbb{C}\mathbb{M} + \mathbb{C})\,\nabla_{\boldsymbol{x}}\boldsymbol{u}^{(0)} + \mathbb{C}\mathsf{Q}p^{(0)}, \tag{3.102}$$

where the fourth rank tensor $\mathbb{M}$ and the second rank tensor Q are defined as follows:

$$\mathbb{M} := \nabla_{\boldsymbol{y}}\mathcal{A}, \quad \mathsf{Q} := \nabla_{\boldsymbol{y}}\boldsymbol{a}. \tag{3.103}$$

Now, (3.92-3.93) can be regarded as the effective macroscale stress equilibrium equations for the poroelastic medium.

A final scalar equation is required to close the macroscale model for the zeroth order variables $\boldsymbol{u}^{(0)}$, $\left\langle \boldsymbol{v}^{(0)} \right\rangle_f$, $p^{(0)}$ and this is provided by averaging the incompressibility condition (3.57) to give:

$$\left\langle \nabla_{\boldsymbol{y}} \cdot \boldsymbol{v}^{(1)} \right\rangle_f + \left\langle \nabla_{\boldsymbol{x}} \cdot \boldsymbol{v}^{(0)} \right\rangle_f = 0. \tag{3.104}$$

Applying the divergence theorem in the $\boldsymbol{y}$ variable, $\boldsymbol{y}$-periodicity together with equation (3.60), and the Reynolds theorem in $\boldsymbol{x}$ gives:

$$\frac{1}{|\Omega|}\int_\Gamma \dot{\boldsymbol{u}}^{(1)} \cdot \boldsymbol{n}\; \mathrm{dS}_y + \nabla_{\boldsymbol{x}} \cdot \left\langle \boldsymbol{v}^{(0)} \right\rangle_f - s_{\mathrm{v}} = 0 \tag{3.105}$$

where

$$s_{\mathrm{v}} := \frac{1}{|\Omega|}\int_\Gamma (\boldsymbol{v}^{(0)} \cdot \boldsymbol{q} - g^{(1)})\; \mathrm{dS}_y \tag{3.106}$$

is an effective mass source which is related to both the lack of macroscopic uniformity and to surface accretion (through $g^{(1)}$). Since

$$\int_{\Gamma} \dot{\boldsymbol{u}}^{(1)} \cdot \boldsymbol{n} \, \mathrm{dS}_y = -\int_{\Omega_s} \nabla_{\boldsymbol{y}} \cdot \dot{\boldsymbol{u}}^{(1)} \, \mathrm{d}\boldsymbol{y} = -\int_{\Omega_s} \mathrm{Tr}\left(\nabla_{\boldsymbol{y}} \dot{\boldsymbol{u}}^{(1)}\right) \, \mathrm{d}\boldsymbol{y}, \tag{3.107}$$

equation (3.105) can be rewritten by means of (3.96) and (3.103), accounting for (3.63, 3.64), as follows:

$$\nabla_{\boldsymbol{x}} \cdot \left\langle \boldsymbol{v}^{(0)} \right\rangle = \left\langle \mathrm{Tr}\, \dot{\mathbb{M}} \right\rangle_s : \nabla_{\boldsymbol{x}} \boldsymbol{u}^{(0)} + \left\langle \mathrm{Tr}\, \mathbb{M} \right\rangle_s : \nabla_{\boldsymbol{x}} \dot{\boldsymbol{u}}^{(0)} + \left\langle \mathrm{Tr}\, \dot{\mathsf{Q}} \right\rangle_s p^{(0)} + \left\langle \mathrm{Tr}\, \mathsf{Q} \right\rangle_s \dot{p}^{(0)} + s_{\mathrm{v}} \tag{3.108}$$

Having derived the new effective model on the macroscale, in the next sections we discuss the physical relevance of the various terms before comparing it against traditional poroelastic frameworks in the literature.

3.6 Discussion of the results

We have derived the homogenised macroscale model for the mechanical behaviour of a poroelastic medium, incorporating surface growth of the solid phase (provided that a suitable growth law is imposed constitutively). Equations (3.80, 3.92, 3.108) form the effective macroscale differential system to be solved for a growing poroelastic medium, provided that the time evolution of the microstructure is updated by (3.53-3.54). It is a closed system for the leading order fields $\left\langle \boldsymbol{v}^{(0)} \right\rangle_f$, $\boldsymbol{u}^{(0)}$, $p^{(0)}$, which are functions of $\boldsymbol{x}$ and t only; substituting (3.70) and (3.102) into (3.92), (3.108) yields a self-consistent system of partial differential equations for the leading order displacement and pressure fields $\boldsymbol{u}^{(0)}$ and $p^{(0)}$, so that the average fluid velocity $\left\langle \boldsymbol{v}^{(0)} \right\rangle_f$ can be finally recovered by means of (3.80).

The macroscale behavior of the fluid flow is given by an effective Darcy-type law for the relative average velocity $\left\langle \dot{\boldsymbol{w}} \right\rangle_f = \left\langle \boldsymbol{v}^{(0)} \right\rangle_f - \phi \dot{\boldsymbol{u}}^{(0)}$ given by (3.80). The effective permeability tensor $\left\langle \tilde{\mathsf{W}} \right\rangle_f (\boldsymbol{x}, t)$ provides the link between macroscale fluid transport and the pore-scale geometry and dynamics. The correction velocity $\left\langle \boldsymbol{h} \right\rangle_f$ on the left hand side of (3.80) comes from global mass conservation (the solid and fluid phases exchange mass without any surface source), and vanishes whenever there is no density difference between the two compartments.

The effective stress equilibrium equations (3.92) can be written in the form:

$$\nabla_{\boldsymbol{x}} \cdot \tau_E = -\boldsymbol{s}_\tau, \tag{3.109}$$

where

$$\tau_E := \left\langle \tau^{(0)} \right\rangle_s - \phi p^{(0)} \mathsf{I} = \langle \mathbb{C}\mathbb{M} + \mathbb{C} \rangle_s \nabla_{\boldsymbol{x}} \boldsymbol{u}^{(0)} + \left(\langle \mathbb{C}\mathsf{Q} \rangle_s - \phi \mathsf{I} \right) p^{(0)}. \tag{3.110}$$

Equations (3.109) and (3.110) can be formally viewed as the average force balance equations for the poroelastic medium.

The scalar equation (3.108), which in standard poroelasticity directly relates the pressure to the fluid and solid phases motion, here encodes instead both the surface growth and the movement of the material. The two terms on the right hand side, including time derivatives of the fields $p^{(0)}$ and $\boldsymbol{u}^{(0)}$, are related to the small displacement of the structure. The two terms including the time derivatives of the coefficients ($\mathrm{Tr}\,\dot{\mathbb{M}},\ \mathrm{Tr}\,\dot{\mathsf{Q}}$) account for the interplay between the elastic movement of the structure and surface growth. In fact, they reduce to zero both in the no growth limit (the coefficients are no longer varying in time) and in the rigid limit (every $\boldsymbol{u}^{(l)}$ for $l = 0, 1, \ldots$ reduces to zero, implying that, through (3.96) and (3.103), $\mathsf{Q} = 0$).

Remark 3.2. Since the interface Γ is moving, it should be understood that every cell problem must be solved in the evolving geometry, described by the leading-order equation for transport of the interface (3.53). As a result, the cell variables $\tilde{\mathsf{W}}$, $\boldsymbol{P}$, $\boldsymbol{h}$, p_h, $\mathcal{A}$, $\boldsymbol{a}$ are microscale variables, and depend on t as well as $\boldsymbol{x}$. Hence, although the effect of growth is purely geometrical at the microscale, it impacts on the macroscale model through the dependence of such variables on the microscale geometry. This represents a crucial difference compared to previous works, where the cell problems and the related macroscale coefficients do not involve any time dependence (see for example Shipley and Chapman (2010) and Arbogast and Lehr (2006)).

Remark 3.3. When the elasticity tensor $\mathbb{C}$ is $\boldsymbol{y}$-constant, the unique (up to a $\boldsymbol{y}$-constant vector field) solution of (3.94-3.95) can be written in the form:

$$\boldsymbol{u}^{(1)} = \mathcal{A} \nabla_{\boldsymbol{x}} \boldsymbol{u}^{(0)} + \boldsymbol{a} p^{(0)} = \tilde{\mathcal{A}} \mathbb{C} \nabla_{\boldsymbol{x}} \boldsymbol{u}^{(0)} + \boldsymbol{a} p^{(0)}, \tag{3.111}$$

where the three-rank tensor $\tilde{\mathcal{A}}$ solves, componentwise:

$$\frac{\partial}{\partial y_j} \left(C_{ijkl} \frac{\partial \tilde{A}_{k\nu\gamma}}{\partial y_l} \right) = 0 \quad \text{in } \Omega_s \tag{3.112}$$

$$C_{ijkl} \frac{\partial \tilde{A}_{k\nu\gamma}}{\partial y_l} n_j + \delta_{i\nu} \delta_{j\gamma} n_j = 0 \quad \text{on } \Gamma. \tag{3.113}$$

Hence, defining the tensor:

$$\mathbb{L} := \nabla_{\boldsymbol{y}} \tilde{\mathcal{A}} \tag{3.114}$$

yields

$$\nabla_{\boldsymbol{y}} \boldsymbol{u}^{(1)} = \mathbb{M} \nabla_{\boldsymbol{x}} \boldsymbol{u}^{(0)} + \mathsf{Q} p^{(0)} = \mathbb{L}\mathbb{C} \nabla_{\boldsymbol{x}} \boldsymbol{u}^{(0)} + \mathsf{Q} p^{(0)}, \tag{3.115}$$

so that $\mathbb{M} = \mathbb{L}\mathbb{C}$. Furthermore, comparing (3.112-3.113) with the cell problem for $\boldsymbol{a}$ given by (3.97-3.98), we deduce that

$$\mathrm{Tr}\, \tilde{\mathcal{A}} = \boldsymbol{a}, \tag{3.116}$$

or, in component notation,

$$\tilde{A}_{ikk} = a_i, \quad i = 1...3, \tag{3.117}$$

up to an $\boldsymbol{y}$-constant vector.

In summary, in the simplified scenario of a locally constant elasticity tensor, once $\tilde{\mathcal{A}}$ is calculated solving the cell problem (3.112-3.113), it suffices to exploit (3.117) to obtain the vector $\boldsymbol{a}$ and hence the tensors Q and $\mathbb{L}$ via (3.103) and (3.114).

3.6.1 Macroscopic uniformity

The momentum source $\boldsymbol{s}_\tau$ and the mass source s_{v} are both related to variations of the interface position vector $\boldsymbol{r}$ with respect to $\boldsymbol{x}$; these contributions arise when a poroelastic growing medium is not macroscopically uniform, so that $\Omega_k = \Omega_k(\boldsymbol{x}, \boldsymbol{y})$ and in particular $\boldsymbol{q} \neq 0$. The vector $\boldsymbol{q}$ reduces to zero whenever $\boldsymbol{r} = \boldsymbol{r}(\boldsymbol{y}, t)$ only and this implies, in turn, that both the initial value for the interface position and the interface velocity are $\boldsymbol{x}$-constant, so that:

$$F_0^{(0)} = F_0^{(0)}(\boldsymbol{y}), \tag{3.118}$$

$$\boldsymbol{v}_\Gamma^{(0)} = \boldsymbol{v}_\Gamma^{(0)}(\boldsymbol{y}, t), \quad \forall t \in (0, T), \tag{3.119}$$

where $F_0^{(0)} = F^{(0)}|_{t=0}$. However, the interface velocity is directly related to the growth law $\tilde{g}$ (see equation 3.16), so that, since we have assumed that movement of the interface is dominated by surface accretion, condition (3.119) is equivalent to:

$$\tilde{g}^{(0)} = \tilde{g}^{(0)}(\boldsymbol{y}, t) \quad \forall t \in (0, T). \tag{3.120}$$

Whenever the medium is macroscopically uniform $\boldsymbol{s}_\tau$ and s_{v} simplify to:

$$\boldsymbol{s}_\tau = 0, \tag{3.121}$$

$$s_{\mathrm{v}} = -\frac{1}{|\Omega|} \int_\Gamma g^{(1)}(\boldsymbol{y}, t)\ \mathrm{dS}_y, \tag{3.122}$$

and the macroscale model to be solved becomes

$$\begin{cases} \left\langle \boldsymbol{v}^{(0)} \right\rangle_f - \phi \dot{\boldsymbol{u}}^{(0)} = - \left\langle \tilde{\mathsf{W}} \right\rangle_f \nabla_{\boldsymbol{x}} p^{(0)} + \left\langle \boldsymbol{h} \right\rangle_f , \\ \nabla_{\boldsymbol{x}} \cdot \tau_E = 0, \\ \nabla_{\boldsymbol{x}} \cdot \left\langle \boldsymbol{v}^{(0)} \right\rangle_f = \left\langle \operatorname{Tr} \dot{\mathbb{M}} \right\rangle_s : \nabla_{\boldsymbol{x}} \boldsymbol{u}^{(0)} + \left\langle \operatorname{Tr} \mathbb{M} \right\rangle_s : \nabla_{\boldsymbol{x}} \dot{\boldsymbol{u}}^{(0)} + \left\langle \operatorname{Tr} \dot{\mathsf{Q}} \right\rangle_s p^{(0)} + \left\langle \operatorname{Tr} \mathsf{Q} \right\rangle_s \dot{p}^{(0)} + s_{\mathrm{v}}, \end{cases} \tag{3.123}$$

where (3.110) represents the effective constitutive relationship for the poroelastic growing medium. Whenever macroscopic uniformity applies, the following solution scheme for the macroscale model applies:

1. Fix material properties of the medium ρ_s, ρ_f, μ, and elastic moduli $\mathbb{C}$.

2. Fix a microscale structure, including a unit cell definition together with an initial value for the interface position $F_0^{(0)}(\boldsymbol{y})$.

3. Prescribe constitutively a growth law $\tilde{g}$, so that every $\tilde{g}^{(l)}$ for $l = 0, 1...$ is defined. In particular, $g^{(0)}$ must satisfy the compatibility condition (3.83). Whenever the densities of the solid and fluid phases are equal ($\rho_s = \rho_f$), every $g^{(l)} = 0$ for $l = 0, 1, \ldots$ so the compatibility condition (3.83) is automatic and $\boldsymbol{h} = \boldsymbol{0}$.

4. Fix a macroscale geometry and corresponding boundary conditions.

5. Solve the cell problems (3.72-3.73), (3.75-3.76), (3.97-3.98), (3.99-3.100) and calculate the corresponding macroscale model coefficients exploiting (3.44) and (3.103).

6. Solve the macroscale model (3.123), using (3.110) as the effective constitutive relationship for the material.

7. Update the interface position by means of equation (3.53), where the leading-order interface velocity is recovered by relationship (3.54).

8. Repeat the calculations explained in (5,6,7) for every $t \in (0, T)$.

It is worth remarking that, whenever the medium is not macroscopically uniform, additional momentum and mass sources of the form (3.93, 3.106) must be taken into account. Further, the interface position would depend on the macroscale variable $\boldsymbol{x}$, so that, in principle, every cell problem should be solved for each $\boldsymbol{x}$ belonging to the macroscale domain (see Figure 2). Hence, in this scenario, computational feasibility may be compromised.

3.7 Particular cases

In this section we focus on specific physical regimes, namely the no-growth limit and the macroscopic isotropy of the poroelastic material. These particular cases are chosen as they coincide with traditional literature results, namely the standard poroelasticity models of Burridge and Keller Burridge and Keller (1981), and also a physically-relevant special case.

In order to avoid unessential technicalities and to better highlight the results, in the following we assume that $\mathbb{C}$ is $\boldsymbol{y}$-constant, so that the considerations in Remark 3.3 apply.

3.7.1 No growth limit and comparison with standard poroelasticity

In the limiting case of no growth, we compare our model to the classical poroelasticity results. In particular, we refer to Burridge and Keller (1981), where the authors derive a set of equations for a poroelastic medium by means of a multiscale approach, that matches the classical Biot's system of equations, reported in Biot (1941) and Biot (1962), in the case of macroscopic uniformity.

Thus, setting $\tilde{g} = 0$ and $\boldsymbol{q} = 0$ our results, written for the average relative fluid-solid velocity $\langle \dot{\boldsymbol{w}} \rangle_f$, the leading order elastic displacement $\boldsymbol{u}^{(0)}$ and the leading order pressure $p^{(0)}$, reduce to:

$$\begin{cases} \langle \dot{\boldsymbol{w}} \rangle_f = -\left\langle \tilde{\mathsf{W}} \right\rangle_f \nabla_{\boldsymbol{x}} p^{(0)} & (3.124) \\ \nabla_{\boldsymbol{x}} \cdot \left\langle \tau^{(0)} \right\rangle_s - \phi \nabla_{\boldsymbol{x}} p^{(0)} = 0 & (3.125) \\ \dot{p}^{(0)} = \dfrac{1}{\langle \mathrm{Tr}\, \mathsf{Q} \rangle_s} \left[\mathrm{Tr} \left(\phi \nabla_{\boldsymbol{x}} \dot{\boldsymbol{u}}^{(0)} - \left\langle \mathbb{L}\mathbb{C} \nabla_{\boldsymbol{x}} \dot{\boldsymbol{u}}^{(0)} \right\rangle_s \right) + \nabla_{\boldsymbol{x}} \cdot \langle \dot{\boldsymbol{w}} \rangle_f \right] & (3.126) \\ \left\langle \tau^{(0)} \right\rangle_s = \langle \mathbb{C}\mathbb{L}\mathbb{C} + \mathbb{C} \rangle_s \nabla_{\boldsymbol{x}} \boldsymbol{u}^{(0)} + \langle \mathbb{C}\mathsf{Q} \rangle_s p^{(0)}, & (3.127) \end{cases}$$

where in (3.126) terms have been rearranged and the interface is assumed fixed, so that the coefficients are no longer varying in time. Since we are in a linearized motion context and the subdomains Ω_f and Ω_s are no longer time dependent, following Burridge and Keller (1981), we focus on linearized dynamics. We consider time harmonic motion with angular frequency ω, such that for every field ψ we have:

$$\dot{\psi} = i\omega\psi. \tag{3.128}$$

Then (3.124-3.126) become

$$\begin{cases} \langle \boldsymbol{w} \rangle_f = -\langle \mathsf{W} \rangle_f \nabla_{\boldsymbol{x}} p^{(0)} & (3.129) \\ \nabla_{\boldsymbol{x}} \cdot \left\langle \tau^{(0)} \right\rangle_s - \phi \nabla_{\boldsymbol{x}} p^{(0)} = 0 & (3.130) \\ p^{(0)} = \dfrac{1}{\langle \mathrm{Tr}\, \mathsf{Q} \rangle_s} \left[\phi \nabla_{\boldsymbol{x}} \cdot \boldsymbol{u}^{(0)} - \mathrm{Tr} \langle \mathbb{L}\mathbb{C} \rangle_s : \nabla_{\boldsymbol{x}} \boldsymbol{u}^{(0)} + \nabla_{\boldsymbol{x}} \cdot \langle \boldsymbol{w} \rangle_f \right], & (3.131) \end{cases}$$

where $\mathsf{W} = \dfrac{1}{i\omega}\tilde{\mathsf{W}}$ solves

$$i\omega\mu\nabla_{\boldsymbol{y}}^2\mathsf{W}^{\mathsf{T}} - \nabla_{\boldsymbol{y}}\boldsymbol{P} + \mathsf{I} = 0 \quad \text{in } \Omega_f \tag{3.132}$$

$$\nabla_{\boldsymbol{y}} \cdot \mathsf{W}^{\mathsf{T}} = 0 \quad \text{in } \Omega_f \tag{3.133}$$

$$\mathsf{W} = 0 \quad \text{on } \Gamma. \tag{3.134}$$

This system recovers the results of Burridge and Keller (1981) [3], when they are simplified to the quasistatic scenario. Furthermore, the scalar coefficient multiplying the square brackets in (3.131), which is, in the present framework, directly related to the geometric and mechanical properties of the elastic phase only, should be compared to the one in Burridge and Keller (1981)[4] given, in our notation, by

$$-\frac{\kappa}{\phi - \kappa\left\langle \mathrm{Tr}\,\mathsf{Q}\right\rangle_s}, \tag{3.135}$$

where κ denotes the bulk modulus. Since incompressibility of the fluid phase is assumed here,

$$\lim_{\kappa\to\infty}\left(-\frac{\kappa}{\phi - \kappa\left\langle \mathrm{Tr}\,\mathsf{Q}\right\rangle_s}\right) = \frac{1}{\left\langle \mathrm{Tr}\,\mathsf{Q}\right\rangle_s}, \tag{3.136}$$

and hence standard poroelasticity is recovered. Note that, as in Burridge and Keller (1981), if the solid matrix is rigid, $\boldsymbol{u}^{(l)} = 0$ for every l, $\dot{\boldsymbol{w}} = \boldsymbol{v}^{(0)}$ and $\mathsf{Q} = 0$. Thus rearranging terms, equations (3.129,3.131) are sufficient to close the system for $(\boldsymbol{v}^{(0)}, p^{(0)})$, which reduces to:

$$\begin{cases} \left\langle \boldsymbol{v}^{(0)}\right\rangle_f = -\left\langle \tilde{\mathsf{W}}\right\rangle_f \nabla_{\boldsymbol{x}} p^{(0)} & (3.137) \\ \nabla_{\boldsymbol{x}} \cdot \left\langle \boldsymbol{v}^{(0)}\right\rangle_f = 0, & (3.138) \end{cases}$$

so that we recover the simple incompressible Darcy's flow when a rigid, non-growing solid phase is assumed.

Remark 3.4. In this work we assume quasistatic dynamical conditions and incompressibility of the fluid phase, a restriction with respect to the regime addressed in Burridge and Keller (1981). These assumptions can be easily relaxed but add no increased physical insight. Moreover, we assume local periodicity, whereas in Burridge and Keller (1981) every field is simply a bounded function of $\boldsymbol{y}$. Our formulation can nevertheless be generalized to local boundness, when assuming that $\Gamma = \partial\Omega_s = \partial\Omega_f$. In this case, the results would be formally equivalent, but substantially different, because the resulting microscale differential problems would not be *cell*-decoupled problems and

[3] Equations (3.127,3.129-3.131) are equivalent to (36a, 39a, 39b, 36b), page 1443, Burridge and Keller (1981), where average quantities are represented by the superscript $^{-}$ instead of brackets $\langle\,\rangle$ and the porosity is denoted by V_f instead of ϕ.

[4] We refer to equations (36b,37), page 1443, Burridge and Keller (1981)

they would have to be solved on the whole microscale domain. It is worth remarking that the present formulation allows us to account for arbitrary macroscale boundary conditions, the latter prescribed, for example, by another mechanical system interacting with the poroelastic growing medium.

3.7.2 Macroscopically isotropic medium

When the poroelastic medium is macroscopically isotropic, we obtain

$$\left\langle \tilde{\mathsf{W}} \right\rangle_f = \frac{\mathrm{k}}{\mu}\mathsf{I} \tag{3.139}$$

$$\langle \mathrm{Tr}\,\mathbb{L}\mathbb{C} \rangle_s = \tilde{\alpha}\mathsf{I} \tag{3.140}$$

$$\langle \mathsf{Q} \rangle_s = \beta\mathsf{I} \rightarrow \langle \mathrm{Tr}\,\mathsf{Q} \rangle_s = 3\beta \tag{3.141}$$

$$\langle \mathbb{C}\mathbb{L}\mathbb{C} + \mathbb{C} \rangle_s \nabla_{\boldsymbol{x}} \boldsymbol{u}^{(0)} = \lambda \nabla_{\boldsymbol{x}} \cdot \boldsymbol{u}^{(0)}\mathsf{I} + 2\hat{\mu}\mathsf{e}^{(0)}, \tag{3.142}$$

where

$$\mathsf{e}^{(0)} := \frac{1}{2}\left[\nabla_{\boldsymbol{x}} \boldsymbol{u}^{(0)} + \left(\nabla_{\boldsymbol{x}} \boldsymbol{u}^{(0)}\right)^{\mathsf{T}}\right],$$

and k, λ, $\hat{\mu}$ formally play the role of an effective permeability and Lamé constants respectively, whereas $\tilde{\alpha}$ and β are poroelastic parameters. Note that $\tilde{\alpha}$, λ, β and $\hat{\mu}$ depend both on the evolving microstructure and on the microscale elastic properties of the medium, whereas k is purely geometric and, in general, all of them are functions of $\boldsymbol{x}$ and t. Following Remark 3.3, we adapt results (3.80,3.92,3.108) accordingly and exploit (3.139-3.142), so that, for a macroscopically isotropic poroelastic growing medium, the system of equations to be solved reads:

$$\begin{cases} \left\langle \boldsymbol{v}^{(0)} \right\rangle_f - \phi \dot{\boldsymbol{u}}^{(0)} = -\dfrac{\mathrm{k}}{\mu}\nabla_{\boldsymbol{x}} p^{(0)} + \langle \boldsymbol{h} \rangle_f & (3.143) \\ \nabla_{\boldsymbol{x}} \cdot \tau_E = -\boldsymbol{s}_\tau & (3.144) \\ \nabla_{\boldsymbol{x}} \cdot \left\langle \boldsymbol{v}^{(0)} \right\rangle_f = \dot{\tilde{\alpha}} \nabla_{\boldsymbol{x}} \cdot \boldsymbol{u}^{(0)} + \tilde{\alpha} \nabla_{\boldsymbol{x}} \cdot \dot{\boldsymbol{u}}^{(0)} + 3\dot{\beta} p^{(0)} + 3\beta \dot{p}^{(0)} + s_{\mathrm{v}}, & (3.145) \end{cases}$$

while the effective isotropic constitutive relationship is:

$$\tau_E := \left[\lambda \nabla_{\boldsymbol{x}} \cdot \boldsymbol{u}^{(0)} + (\tilde{\alpha} - \phi) p^{(0)}\right]\mathsf{I} + 2\hat{\mu}\mathsf{e}^{(0)}. \tag{3.146}$$

3.8 Conclusions

We have developed a theoretical model which describes the macroscopic behaviour of a poroelastic medium, when surface mass exchange occurs in the pores. The starting point is a coupled description of linear elasticity and Stokes' flow of the solid and fluid phases at the pore-scale. The solid and fluid mechanics are coupled through continuity of stress and mass flow on the displacing solid-fluid interface. Next, homogenisation via multiple scales yields the effective model on the macroscale. The result is a new system of equations for a poroelastic medium where time-dependent growth is encoded in the coefficients of the model; these coefficients can be computed by solving cell problems on the evolving microstructure.

The fluid flow is described through a Darcy-type law (3.80) for the relative average velocity of the fluid and solid phase, with an associated permeability tensor that captures the dependence on the pore-scale structure. A correction velocity $\langle \boldsymbol{h} \rangle_f$ appears as a consequence of the global transfer of mass between the solid and fluid phases. The mechanical properties of the poroelastic growing medium are directly encoded in a new effective constitutive relationship (3.102) which accounts for the fluid pressure in the pore, small elastic displacement of the structure and surface accretion of the solid phase. The interplay between the strain of the structure and appositional growth resides in the effective mass source contributions.

When macroscopic uniformity applies, the model simplifies and a solution strategy is provided. Limiting cases of the model are explored: in absence of growth, the model reduces to the classical result of Burridge and Keller Burridge and Keller (1981), while the assumption of isotropic growth leads to a much simpler set of equations. In the latter scenario, hydraulic and mechanical parameters are recovered, which formally play the role of effective permeability and Lamé moduli, respectively. A distinction can be made between parameters which depend purely on the evolving microstructure and pore scale elastic properties of the medium, and those which are purely geometric.

The homogenised set of equations has been obtained under assumption of periodic microstructure, infinitesimal strain and slow flow. While a slow modulation of the periodicity could be introduced without affecting the main results, the physical assumptions underlying the use of linear elasticity and Stokes' equations cannot be relaxed.

There are numerous opportunities for extension and application of the model presented here to specific mechanical systems. A natural development is to compare predictions of our new model to the classical description of Biot in the context of specific pore-scale structures. (In O'Dea et al.

(2013) the authors account for surface growth of a rigid solid porous medium, and numerical solutions of the resulting model are explored). In general, a critical next step in the application of the models derived here is to introduce constitutive equations for the mass exchange rate $\tilde{g}$, motivated by the specific application under consideration. This will enable simulations to be performed, model testing and prediction.

Final remarks

In this thesis we have investigated fluid and drug transport phenomena in tumor biology, as well as the poro-mechanics of growing materials, by multiscale homogenization (Sanchez-Palencia, 1980, 1983; Holmes, 1995; Mei and Vernescu, 2010). The original results we achieved can be summarized as follows:

- In chapter 1, we derived a new tissue scale mathematical framework for the fluid and drug dynamics in vascularized malignant tissues. The results is a double Darcy model for the blood flow and a double advection-reaction-diffusion differential system, coupled through effective mass sources and suitable reaction operators. The model generalizes that in Shipley and Chapman (2010) and account for several key physical phenomena in the tumor; blood transport in both the tumor interstitium and capillary network are taken into account, as well as advection and diffusion of drug and possibly non-linear uptake mechanisms. The provided framework is computationally feasible, as it holds on the tissue scale only and comprises the geometric information of the microvasculature in the model coefficients, which can be computed solving classical differential problem on the microscale representative unit cell. Macroscopic variations of the microstructure is encoded in the derived cell problems, as well as in effective correction factors, which appear in the effective mass sources, advective velocities and reaction operators. The fluid and drug transport models are coupled, as our formulation is robust with respect to choices for the fluid and drug fluxes, which are, in turn, the driving forces for the key mechanisms underneath the tumor system physics. The drug flux can exhibit large non-linearities in the fluid flux, while the fluid flux is influenced by the osmotic pressure con-

tribution due to the drug concentration difference across the vessels walls.

- In chapter 2 we focus on the fluid transport only, in order to point out the role of the microvascular tortuosity on blood convection in tumors. The model by Shipley and Chapman (2010) is solved for a prototypical geometry and the capillary and interstitial hydraulic conductivities are computed by 3D numerical simulations. The numerical results show that the hydraulic conductivity of the vessels damps as far as the tortuosity increases. As a result, the most striking prection of the model is that the blood convection in tumors is dramatically impaired for tortuous microvasculatures, so that normalization therapies should focus on regularization of the capillary network.

- In chapter 3 we derive a novel multiscale model for the behavior of poroelastic growing materials. The result is an effective tissue scale poroelastic-type model, with time dependent coefficients which account for the interplay between appositional growth and elastic strains. The role of the time-evolving pore-structure is encoded in the model coefficients, which can be computed solving time dependent cell problems on the pore scale. Our formulation is robust with respect to macroscopic variations of the pore geometry, which are taken into account in effective mass and momentum sources. Global mass conservation is guaranteed by a correction velocity, which modifies the usual Darcy profile. The model can be applied to surface tumor growth whenever the linear elastic regime holds, provided that a suitable growth law, which drives the pore geometry evolution, is prescribed. Standard poroelasticity Burridge and Keller (1981) is recovered in the no-growth limit.

APPENDIX $\mathcal{A}$

Analytical solution of the macroscale model

The problem to be solved is the following coupled system of second order differential equations of the form:

$$\begin{cases} \frac{1}{r}\frac{d^2}{dr^2}(rp_c) = M_c(p_c - p_t) \qquad 0 < r < R & \text{(A.1)} \\ \frac{1}{r}\frac{d^2}{dr^2}(rp_t) = -M_t(p_c - p_t) \qquad 0 < r < R & \text{(A.2)} \\ \frac{dp_c}{dr}|_{r=0} = \frac{dp_t}{dr}|_{r=0} = 0 & \text{(A.3)} \\ p_c|_{r=R} = \bar{p} > 0, \quad p_t|_{r=R} = 0, & \text{(A.4)} \end{cases}$$

where

$$M_c = \frac{\bar{L}_p S}{K_c|\Omega_c|}, \quad M_t = \frac{\bar{L}_p S}{K_t|\Omega_t|}. \tag{A.5}$$

We rewrite the problem (A.1-A.4) in terms of relative pressures and radial coordinate

$$\hat{p}_c = p_c/\bar{p}; \quad \hat{p}_t = p_t/\bar{p}; \quad \hat{r} = r/R, \tag{A.6}$$

thus we obtain:

$$\begin{cases} \frac{1}{\hat{r}}\frac{d^2}{d\hat{r}^2}(\hat{r}\hat{p}_c) = R^2 M_c(\hat{p}_c - \hat{p}_t) \qquad 0 < \hat{r} < 1 & \text{(A.7)} \\ \frac{1}{\hat{r}}\frac{d^2}{d\hat{r}^2}(\hat{r}\hat{p}_t) = -R^2 M_t(\hat{p}_c - \hat{p}_t) \qquad 0 < \hat{r} < 1 & \text{(A.8)} \\ \frac{d\hat{p}_c}{d\hat{r}}|_{\hat{r}=0} = \frac{d\hat{p}_t}{d\hat{r}}|_{\hat{r}=0} = 0 & \text{(A.9)} \\ \hat{p}_c|_{\hat{r}=1} = 1, \quad \hat{p}_t|_{\hat{r}=1} = 0. & \text{(A.10)} \end{cases}$$

We first derive the solution for the relative pressure difference

$$\hat{\psi} := \hat{p}_c - \hat{p}_t, \tag{A.11}$$

so that, subtracting equation (A.8) from equation (A.7) and rearranging boundary conditions, yields the following differential problem for $\hat{\psi}$:

$$\begin{cases} \frac{1}{\hat{r}}\frac{d^2}{d\hat{r}^2}(\hat{r}\hat{\psi}) = \alpha^2\hat{\psi} \qquad 0 < \hat{r} < 1 & \text{(A.12)} \\ \frac{d\hat{\psi}}{d\hat{r}}|_{\hat{r}=0} = 0 & \text{(A.13)} \\ \hat{\psi}|_{\hat{r}=1} = 1, & \text{(A.14)} \end{cases}$$

where we set

$$\alpha = R\sqrt{M_c + M_t}. \tag{A.15}$$

We set

$$\hat{\psi} = \frac{\tilde{\psi}}{\hat{r}}, \tag{A.16}$$

so that, substitution of (A.16) into (A.12) yields:

$$\frac{d^2\tilde{\psi}}{d\hat{r}^2} - \alpha^2\tilde{\psi} = 0. \tag{A.17}$$

The general solution of the linear second order homogeneous differential equation (A.17) reads:

$$\tilde{\psi} = \tilde{A}\exp(\alpha\hat{r}) + \tilde{B}\exp(-\alpha\hat{r}), \tag{A.18}$$

and, enforcing (A.16)

$$\hat{\psi} = \frac{\tilde{A}\exp(\alpha\hat{r}) + \tilde{B}\exp(-\alpha\hat{r})}{\hat{r}}, \tag{A.19}$$

where $\tilde{A}$ and $\tilde{B}$ are integration constants to be determined exploiting boundary conditions (A.13-A.14). In order to exploit (A.13) we first compute:

$$\frac{d\hat{\psi}}{d\hat{r}} = \frac{\alpha\hat{r}\tilde{A}\exp(\alpha\hat{r}) - \alpha\hat{r}\tilde{B}\exp(-\alpha\hat{r}) - \tilde{A}\exp(\alpha\hat{r}) - \tilde{B}\exp(-\alpha\hat{r})}{\hat{r}^2}, \tag{A.20}$$

then we observe that

$$\exp(\alpha\hat{r}) = 1 + \alpha\hat{r} + \frac{\alpha^2\hat{r}^2}{2} + O(\alpha^3\hat{r}^3), \tag{A.21}$$

$$\exp(-\alpha\hat{r}) = 1 - \alpha\hat{r} + \frac{\alpha^2\hat{r}^2}{2} + O(\alpha^3\hat{r}^3), \tag{A.22}$$

by means of Taylor expansions around $\alpha\hat{r} = 0$, where, for simplicity of notation, we use the same symbol $O(\alpha^3\hat{r}^3)$ to denote any sum of power series terms which approach 0 faster or equal to $\hat{r}^3$ as $\hat{r} \to 0$. Substituting expansions (A.21-A.22) into (A.20) and rearranging terms yields:

$$\frac{d\hat{\psi}}{d\hat{r}} = \frac{\left(\tilde{A} + \tilde{B}\right)\left(\frac{\alpha^2\hat{r}^2}{2} - 1\right) + O(\alpha^3\hat{r}^3)}{\hat{r}^2} \tag{A.23}$$

Imposing boundary condition (A.13) yields:

$$\frac{d\hat{\psi}}{d\hat{r}}|_{\hat{r}=0} = \lim_{\hat{r}\to 0}\frac{d\hat{\psi}}{d\hat{r}} = 0 \Rightarrow \lim_{\hat{r}\to 0}\frac{\left(\tilde{A} + \tilde{B}\right)\left(\frac{\alpha^2\hat{r}^2}{2} - 1\right) + O(\alpha^3\hat{r}^3)}{\hat{r}^2} = 0, \tag{A.24}$$

which holds if and only if

$$\tilde{B} = -\tilde{A}. \tag{A.25}$$

Starting from (A.19), we can find the solution for $\hat{\psi}$ via (A.25) and exploiting Dirichlet boundary condition (A.14), namely:

$$\hat{\psi}|_{\hat{r}=1} = 1 \Rightarrow \frac{2\tilde{A}\sinh(\alpha\hat{r})}{\hat{r}}|_{\hat{r}=1} = 1 \Rightarrow \tilde{A} = \frac{1}{2\sinh(\alpha)}, \tag{A.26}$$

hence the soultion for the relative pressure difference $\hat{\psi}$ reads:

$$\hat{\psi} = \frac{\sinh(\alpha\hat{r})}{\hat{r}\sinh(\alpha)}. \tag{A.27}$$

We point out that the function $\hat{\psi}$ must be finite in the limit $\hat{r} \to 0$, in fact:

$$\lim_{\hat{r}\to 0}\frac{\sinh(\alpha\hat{r})}{\hat{r}\sinh(\alpha)} = \frac{\alpha}{\sinh(\alpha)} < +\infty. \tag{A.28}$$

In order to compute the complete solution for $\hat{p}_c$ and $\hat{p}_t$, we can rewrite (A.7) and (A.8) as follows:

$$\begin{cases} \frac{1}{\hat{r}}\frac{d^2}{d\hat{r}^2}(\hat{r}\hat{p}_c) = R^2 M_c\hat{\psi} \qquad 0 < \hat{r} < 1 & \text{(A.29)} \\ \frac{d\hat{p}_c}{d\hat{r}}|_{\hat{r}=0} = 0 & \text{(A.30)} \\ \hat{p}_c|_{\hat{r}=1} = 1, & \text{(A.31)} \end{cases}$$

$$\begin{cases} \frac{1}{\hat{r}}\frac{d^2}{d\hat{r}^2}(\hat{r}\hat{p}_t) = -R^2 M_t\hat{\psi} \qquad 0 < \hat{r} < 1 & \text{(A.32)} \\ \frac{d\hat{p}_t}{d\hat{r}}|_{\hat{r}=0} = 0 & \text{(A.33)} \\ \hat{p}_t|_{\hat{r}=1} = 0, & \text{(A.34)} \end{cases}$$

where $\hat{\psi}$ is understood to be the known function given by (A.27), so that the problems (A.29-A.31), (A.32-A.34) are formally decoupled. Setting

$$\hat{p}_c = \frac{\tilde{p}_c}{\hat{r}}; \quad \hat{p}_t = \frac{\tilde{p}_t}{\hat{r}}, \tag{A.35}$$

equations (A.29) and (A.32) reduce to

$$\frac{d^2\tilde{p}_c}{d\hat{r}^2} = R^2 M_c \tilde{\psi}, \tag{A.36}$$

$$\frac{d^2\tilde{p}_t}{d\hat{r}^2} = -R^2 M_t \tilde{\psi}, \tag{A.37}$$

and the general solutions read

$$\tilde{p}_c = \frac{R^2 M_c}{\alpha^2}\tilde{\psi} + \tilde{C}\hat{r} + \tilde{D}, \tag{A.38}$$

$$\tilde{p}_t = -\frac{R^2 M_t}{\alpha^2}\tilde{\psi} + \tilde{E}\hat{r} + \tilde{F}, \tag{A.39}$$

and, exploiting (A.16), (A.35)

$$\hat{p}_c = \frac{R^2 M_c}{\alpha^2}\hat{\psi} + \tilde{C} + \frac{\tilde{D}}{\hat{r}}, \tag{A.40}$$

$$\hat{p}_t = -\frac{R^2 M_t}{\alpha^2}\hat{\psi} + \tilde{E} + \frac{\tilde{F}}{\hat{r}}, \tag{A.41}$$

where $\tilde{C}$, $\tilde{D}$, $\tilde{E}$, $\tilde{F}$ are integration constants to be determined exploiting the proper boundary conditions for $\hat{p}_c$ and $\hat{p}_t$. We impose that $\hat{p}_c$ and $\hat{p}_t$ are finite in the limit $\hat{r} \to 0$ i.e, since (A.28) holds for $\hat{\psi}$:

$$\tilde{D} = \tilde{F} = 0. \tag{A.42}$$

Furthermore, when accounting for (A.42) and (A.24) in (A.40-A.41), $\hat{p}_c$ and $\hat{p}_t$ automatically satisfy the Neumann boundary conditions (A.30) and (A.33), respcetively. Exploiting the Dirichlet boundary conditions (A.31-A.34) we can find $\tilde{C}$ and $\tilde{E}$, namely:

$$\hat{p}_c|_{\hat{r}=1} = 1 \Rightarrow \tilde{C} = 1 - \frac{R^2 M_c}{\alpha^2}; \quad \hat{p}_t|_{\hat{r}=1} = 0 \Rightarrow \tilde{E} = \frac{R^2 M_t}{\alpha^2}. \tag{A.43}$$

Enforcing definition (A.15) in (A.43) we deduce:

$$\tilde{C} = \tilde{E}, \tag{A.44}$$

so that the solutions for $\hat{p}_c$ and $\hat{p}_t$ rewrite:

$$\hat{p}_c = \frac{R^2 M_c}{\alpha^2}\hat{\psi} + \frac{R^2 M_t}{\alpha^2}, \tag{A.45}$$

$$\hat{p}_t = -\frac{R^2 M_t}{\alpha^2}\hat{\psi} + \frac{R^2 M_t}{\alpha^2}, \tag{A.46}$$

respectively. We check that the solutions given by (A.45-A.46) satisfy (A.11), namely

$$\hat{p}_c - \hat{p}_t = \frac{R^2 M_c}{\alpha^2}\hat{\psi} + \frac{R^2 M_t}{\alpha^2} + \frac{R^2 M_t}{\alpha^2}\hat{\psi} - \frac{R^2 M_t}{\alpha^2} = \hat{\psi}, \tag{A.47}$$

where we enforced definition (A.15).

We finally explicitly state the solution of the coupled problem (A.7-A.10) by means of (A.27) and rearranging terms:

$$\hat{p}_c = \frac{1}{M_c + M_t}\left(M_t + \frac{M_c \sinh(\alpha\hat{r})}{\hat{r}\sinh(\alpha)}\right), \tag{A.48}$$

$$\hat{p}_t = \frac{M_t}{M_c + M_t}\left(1 - \frac{\sinh(\alpha\hat{r})}{\hat{r}\sinh(\alpha)}\right). \tag{A.49}$$

List of Figures

List of Tables

Bibliography

Ambrosi, D., Guana, F., 2007. Stress–modulated growth. Math Mech. Solids 12, 319–342.

Ambrosi, D., Preziosi, L., 2002. On the closure of mass balance models for tumor growth. Math. Mod. Meth. Appl. Sci. 12, 737.

Ambrosi, D., Vitale, G., Preziosi, L., 2010. The insight of mixtures theory for growth and remodeling. ZAMP 61, 177–191.

Arbogast, T., Lehr, H.L., 2006. Homogenization of a darcy-stokes system modeling vuggy porous media. Computational Geosciences 10, 291–302.

Asaishi, K., Endrich, B., Götz, A., Messmer, K., 1981. Quantitative analysis of microvascular structure and function in the amelanotic melanoma a-mel-3. Cancer research 41, 1898–1904.

Ateshian, G.A., 2007. On the theory of reactive mixtures for modeling biological growth. Biomechanics and modeling in mechanobiology 6, 423–445.

Baek, S., Rajagopal, K., Humphrey, J., et al., 2006. A theoretical model of enlarging intracranial fusiform aneurysms. Journal of biomechanical engineering 128, 142.

Batchelor, G.K., 2000. An introduction to fluid dynamics. Cambridge university press.

Beavers, G.S., Joseph, D.D., 1967. Boundary conditions at a naturally permeable wall. Journal of Fluid Mechanics 30, 197–207.

Bettahalli, N., Vicente, J., Moroni, L., Higuera, G., Van Blitterswijk, C., Wessling, M., Stamatialis, D., 2011. Integration of hollow fiber membranes improves nutrient supply in three-dimensional tissue constructs. Acta biomaterialia 7, 3312–3324.

Bhalla, G., Deen, W.M., 2007. Effects of molecular shape on osmotic reflection coefficients. Journal of Membrane Science 306, 116–124.

Biot, M.A., 1941. General theory of three-dimensional consolidation. Journal of applied physics 12, 155–164.

Biot, M.A., 1962. Mechanics of deformation and acoustic propagation in porous media. Journal of applied physics 33, 1482–1498.

Bibliography

Bottaro, A., Ansaldi, T., 2012. On the infusion of a therapeutic agent into a solid tumor modeled as a poroelastic medium. Journal of Biomechanical engineering 134, 1–6.

Boucher, Y., Baxter, L.T., Jain, R.K., 1990. Interstitial pressure gradiennts in tissue-isolated and subcutaneous tumors: implications for therapy. Cancer Research 50, 4478–4484.

Boucher, Y., Brekken, C., Netti, P., Baxter, L., Jain, R., 1998. Intratumoral infusion of fluid: estimation of hydraulic conductivity and implications for the delivery of therapeutic agents. British journal of cancer 78, 1442.

Bowen, R., 1980. Incompressible porous media models by the use of the theory of mixtures. Int. J. Eng. Science 18, 1129–1148.

Bowen, R., 1982. Compressible porous media models by the use of the theory of mixtures. Int. J. Eng. Science 20, 697–735.

Burridge, R., Keller, J., 1981. Poroelasticity equations derived from microstructure. Journal of acoustical society of America 70, 1140–1146.

Carman, P., 1937. Fluid flow through granular beds. Transactions-Institution of Chemical Engineeres 15, 150–166.

Carmeliet, P., Jain, R.K., 2000. Angiogenesis in cancer and other diseases. Nature 407, 249–257.

Ciarletta, P., Preziosi, L., Maugin, G., 2013. Mechanobiology of interfacial growth. Journal of the Mechanics and Physics of Solids 61, 852 – 872.

Cooke, B.M., Stuart, J., 1988. Automated measurements of plasma viscosity by a capillary viscometer. Journal of clinical pathology 41, 1213–1216.

Cowin, S.C., 2004. Tissue growth and remodeling. Annu. Rev. Biomed. Eng. 6, 77–107.

Davit, Y., Bell, C., Byrne, H., Chapman, L., Kimpton, L., Lang, G., Leonard, K., Oliver, J., Pearson, N., Shipley, R., Waters, S., Whiteley, J., Wood, B., Quintard, M., 2013. Homogenization via formal multiscale asymptotics and volume averaging: how do the two techniques compare? Advances in Water Resources (in press) .

Di Federico, V., Cintoli, S., Bizzarri, G., 2002. Moto alla stokes in condotti a sezione variabile. 28Â° Convegno di Idraulica e Costruzioni idrauliche Potenza 16-19 settembre 2002 .

Dreher, M.R., Liu, W., Michelic, C., Dewhirst, M.W., Yuan, F., Chilkoti, A., 2006. Tumor vascular permability, accumulation and penetration of macromolecular drug carriers. JNCI 98, 335–344.

Fahareus, R., Lindqvist, T., 1931. The viscosity of the blood in narrow capillary tubes. American Journal of Physiology 96, 562–568.

Formaggia, L., Quarteroni, A., Veneziani, A., 2009. Cardiovascular Mathematics. Springer.

Gray, W.G., 1975. A derivation of the equations for multi-phase transport. Chemical Engineering Science 30, 229–233.

Gurtin, M., Fried, E., Anand, L., 2010. The mechanics and thermodynamics of continua. Cambridge University press.

Hahnfeldt, P., Panigrahy, D., Folkman, J., Hlatky, L., 1999. Tumor development under angiogenic signaling a dynamical theory of tumor growth, treatment response, and postvascular dormancy. Cancer research 59, 4770–4775.

Hashizume, H., 2000. Openings between defective endothelial cells explain tumor vessel leakiness. Am. J. Pathol. 156, 1363–1380.

Heijs, A.W.J., Lowe, C.P., 1995. Numerical evaluation of the permeability and the kozeny constant for two types of porous media. Phys. Rev. E 51, 4346–4352.

Heldin, C., Rubin, K., Pietras, K., Ostman, A., 2004. High interstitial fluid pressure- an obstacle in cancer therapy. Nature Reviews Cancer 4, 806–813.

Holmes, M., 1995. Introduction to perturbation method. Springer-Verlag.

Hornung, U., 1997. Homogenization and porous media. Springer.

Humphrey, J., Rajagopal, K., 2003. A constrained mixture model for arterial adaptations to a sustained step change in blood flow. Biomechanics and modeling in mechanobiology 2, 109–126.

Hutter, K., 1983. Theoretical glaciology: material science of ice and the mechanics of glaciers and ice sheets. Reidel.

Jain, R.K., 1987a. Transport of molecules across tumor vasculature. Cancer Metastasis Review 6, 559–594.

Jain, R.K., 1987b. Transport of molecules in the tumor interstitium: a review. Cancer Research 47, 3039–3051.

Jain, R.K., 1988. Determinants of tumor blood flow: A review. Cancer Research 48, 2641–2658.

Jain, R.K., Baxter, L.T., 1988. Mechanisms of heterogeneous distribution of monoclonal antibodies and other macromolecules in tumors: significance of elevated interstitial pressure. Cancer Research 48, 7022–7032.

Jain, R.K., Tong, R.T., Munn, L.L., 2007. Effect of vascular normalization by antiangiogenic therapy on interstitial hypertension, peritumor edema, and lymphatic metastasis: insights from a mathematical model. Cancer Res 67, 2729–2735.

Jayaweera, A.R., Edwards, N., Glasheen, W.P., Villanueva, F.S., Abbott, R.D., Kaul, S., 1994. In vivo myocardial kinetics of air-filled albumin microbubbles during myocardial contrast ecocardiography. comparison with radiolabeled red blood cells. Circulation Research 74, 1157–1165.

Jones, I.P., 1973. Low reynolds number flow past a porous spherical shell. Mathematical Proceedings of the Cambridge Phylosofical Society 73, 231–238.

Kedem, O., Katchalsky, A., 1958. Thermodynamic of the permeability of biological membranes to non-electrolytes. Biochimica and Biophysica Acta 27, 229–246.

Kitanidis, P.K., Dykaar, B.B., 1997. Stokes flow in a slowly varying two-dimensional periodic pore. Transport in porous media 26, 89–98.

Kozeny, J., 1927. Ueber kapillare leitung des wassers im boden. Sitzungsber. Akad. Wiss. Wien 136, 271–306.

Lemon, G., King, J.R., Byrne, H.M., Jensen, O.E., Shakesheff, K.M., 2006. Mathematical modelling of engineered tissue growth using a multiphase porous flow mixture theory. Journal of mathematical biology 52, 571–594.

Less, J.R., Skalak, T.C., Sevick, E.M., 1991. Microvascular architecture in a mammary carcinoma: Branching patterns and vessels dimensions. Cancer Research 51, 265–273.

Malevich, A., Mityushev, V., Adler, P., 2006. Stokes flow through a channel with wavy walls. Acta mechanica 182, 151–182.

Matyka, M., Khalili, A., Koza, Z., 2008. Tortuosity-porosity relation in porous media flow. Phys. Rev. E 78, 026306.

Mei, C.C., Vernescu, B., 2010. Homogenization Methods for multiscale mechanics. World Scientific.

Mikelic, A., Wheeler, M.F., 2012. On the interface law between a deformable porous medium containing a viscous fluid and an elastic body. Mathematical Models and Method in Applied Sciences 22, 1–32.

Modok, S., Hyde, P., Mellor, H., Roose, T., Callaghan, R., 2006. Diffusivity and distribution of vinblastine in three-dimensional tumour tissue: Experimental and mathematical modelling. European Journal of Cancer 42, 2404–2413.

Modok, S., Scott, R., Alderden, R., Hall, M., Mellor, H., Bohic, S., Roose, T., Hambley, T., Callaghan, R., 2007. Transport kinetics of four-and six-coordinate platinum compounds in the multicell layer tumour model. British Journal of Cancer 97, 194–200.

Moeendarbary, V., Fritzsche, H., Moulding, T., Stride, M., Charras, 2013. The cytoplasm of living cells behaves like a poroelastic material. Nature Materials 12, 253–261.

Netti, P.A., Berk, D.A., Swartz, M.A., Grodzinsky, A.J., Jain, R.K., 2000. Role of extracellular matrix assembly in interstitial transport in solid tumors. Cancer Research 60, 2497–2503.

O'Dea, R.D., Nelson, M.R., El Haj, A.J., Waters, S.L., M., B.H., 2013. A multiscale analysis of nutrient transport and biological tissue growth in vitro. Under submission .

O'Dea, R.D., Waters, S.L., Byrne, H.M., 2008. A two-fluid model for tissue growth within a dynamic flow environment. European Journal of Applied Mathematics 19, 607–634.

Owen, M.R., Alarcon, T., Maini, P.K., Byrne, H.M., 2008. Angiogenesis and vascular remodelling in normal and cancerous tissues. Journal of Mathematical Biology 58, 689–721.

Penta, R., Ambrosi, D., 2014. The role of the microvascular tortuosity in tumor transport phenomena. Journal of Theoretical Biology Submitted.

Penta, R., Ambrosi, D., Quarteroni, A., 2013. Multiscale homogenization for fluid and drug transport in vascularized malignant tissues. Mathematical Models and Methods in Applied Sciences (M3AS) Submitted.

Penta, R., Ambrosi, D., Shipley, R.J., 2014. Effective governing equations for poroelastic growing media. The Quarterly Journal of Mechanics and Applied Mathematics doi:doi: 10.1093/qjmam/hbt024.

Pioletti, D.P., Rakotomanana, L.R., 2000. Non-linear viscoelastic laws for soft biological tissues. European Journal of Mechanics-A/Solids 19, 749–759.

Pozrikidis, C., 2009. Numerical simulations of blood flow through microvascular capillary networks. Bullettin of Mathematical Biology 71, 1520–1541.

Preziosi, L., Ambrosi, D., Verdier, C., 2010. An elasto-visco-plastic model of cell aggregates. Journal of Theoretical Biology 262, 35 – 47.

Preziosi, L., Byrne, H., 2003. Modelling solid tumour growth using the theory of mixtures. Math. Med. Biol. 20, 341–366.

Pries, A., Neuhaus, D., Gaehtgens, P., 1992. Blood viscosity in tube flow: dependence on diameter and hematocrit. American Journal of Physiology-Heart and Circulatory Physiology 263, H1770–H1778.

Pries, A., Secomb, T., 2003. Rheology of the microcirculation. Clinical hemorheology and microcirculation 29, 143–148.

Pries, A.R., Secomb, T.W., Gaehtgens, P., Gross, J.F., 1990. Blood flow in microvascular networks. experiments and simulations. Circulation Research 67, 826–834.

Pries, A.R., Secomb, T.W., Gaethgens, P., 1998. Structural adaptation and stability of microvascular networks: theory and simulations. American Journal of physiology 275, 349–360.

Rand, P.W., Lacombe, E., Hunt, H.E., 1964. Viscosity of normal human blood under normothermic and hypothermic conditions. Journal of Applied Physiology 19, 117–122.

Rodriguez, E., Hoger, A., McCulloch, A., 1994. Stress -dependent finite growth in soft elastic tissues. J. Biomech. 27, 455–467.

Roose, T., Chapman, S.J., Maini, P.K., 2007. Mathematical models of avascular tumor growth. Siam Review 49, 179–208.

Roose, T., Netti, P.A., Munn, L.L., Boucher, Y., Jain, R.K., 2003. Solid stress generated by spheroid growth estimated using a linear poroelasticity model? Microvascular research 66, 204–212.

Roose, T., Swartz, M.A., 2012. Multiscale modeling of lymphatic drainage from tissues using homogenization theory. Journal of biomechanics 45, 107–115.

Sanchez-Palencia, E., 1980. Non-Homogeneous Media and Vibration Theory-Lecture Notes in Physics 127. Springer-Verlag.

Sanchez-Palencia, E., 1983. Homogenization method for the study of composite media. Asymptotic analysis II-Lecture notes in mathematics 985, 192–214.

Schuff, M., Gore, J., Nauman, E., 2013a. A mixture theory model of fluid and solute transport in the microvasculature of normal and malignant tissues. i. theory. Journal of Mathematical Biology 66, 1179–1207.

Schuff, M., Gore, J., Nauman, E., 2013b. A mixture theory model of fluid and solute transport in the microvasculature of normal and malignant tissues. ii. factor sensitivity analysis, calibration, and validation. Journal of Mathematical Biology in press, 1–31.

Scomparin, A., Salmaso, S., Bersani, S., Satchi-Fainaro, R., Caliceti, P., 2011. Novel folated and non-folated pullulan bioconjugates for anticancer drug delivery. European Journal of Pharmaceutical Sciences 42, 547–558.

Sevick, E.M., Jain, R.K., 1991. Measurement of capillary filtration coefficient in a solid tumor. Cancer research 51, 1352–1355.

Shipley, R., 2008. Multiscale Modelling of Fluid and Drug Transport in Vascular Tumors. Ph.D. thesis. St. Hugh's College University of Oxford.

Shipley, R.J., Chapman, J., 2010. Multiscale modelling of fluid and drug transport in vascular tumors. Bulletin of Mathematical Biology. 72, 1464–1491.

Simonescu, M., Simonescu, N., Palade, G.E., 1974. Morphometric data on the endothelium of blood capillaries. The Journal of cell biology 60, 128–152.

Stevens, C.W., Munden, R.F., Forster, K.M., Kelly, J.F., Liao, Z., Starkschall, G., Tucker, S., Komaki, R., 2001. Respiratory driven lung tumor motion is indipendent of tumor size, tumor location and pulmonary function. International Journal of Radiation Oncology*Biology*Physics 51, 62–68.

Swabb, E.A., Wei, J., Gullino, P.M., 1974. Diffusion and convection in normal and neoplastic tissues. Cancer Research 34, 2814–2822.

Taber, L., 1995. Biomechanics of growth, remodeling and morphogenesis. Appl Mech. Rev. 48, 487–545.

Tang, L., Su, J., Huang, D.S., Lee, D.Y., Li, K.C., Zhou, X., 2012. An integrated multiscale mechanistic model for cancer drug therapy. ISRN Biomathematics 2012, 12.

Waniewsky, J., 2006. Mathematical modeling of fluid and solute transport in hemodyalisis and peritoneal analysis. Journal of Membrane Science 274, 24–37.

Whitaker, S., 1973. The transport equations for multi-phase systems. Chemical Engineering Science 28, 139–147.

Yoshii, Y., Sugiyama, K., 1988. Intercapillary distance in the proliferating area of human glioma. Cancer research 48, 2938–2941.